Does the weak interaction constant depend on time?

A. S. Barabash[a)]
Institute of Theoretical and Experimental Physics, 117259 Moscow, Russia

A comparison is made of the probability of the process of two-neutrino double β decay for ^{82}Se and ^{96}Zr in direct (counter) and geochemical experiments. The experimental data for ^{130}Te are analyzed. It is shown that this probability is systematically lower in geochemical experiments, which characterize the probability of $2\beta(2\nu)$ decay 10^9 yr ago. It is proposed that this could be due to a change in the weak-interaction constant with time. It is proposed that a series of new, precise measurements be performed with the aid of counters and geochemical experiments. © *1998 American Institute of Physics.*
[S0021-3640(98)00113-3]

PACS numbers: 23.40.Bw, 27.50.+e, 27.60.+j

The question of the dependence of the fundamental constants on time was formulated by Dirac in 1937 — this is the so-called hypothesis of large numbers.[1] This question was later discussed in Refs. 2–7. Although Dirac's hypothesis was not confirmed in its initial form, interest in this problem gathered new strength in the 1980s, since a time dependence of the coupling constants appears in multidimensional Kaluza–Klein models[8,9] and in superstring theories[10] (see also Refs. 11 and 12). These theories are formulated for a multidimensional space, which must then be compactified to the four observable dimensions of space–time. In these theories the fundamental coupling constants are associated with the radii of additional dimensions and these additional dimensions can manifest themselves through a time dependence of the coupling constants. The radii can shrink, increase, or even oscillate. It has not been ruled out that the compactification process is continuing at present. A time dependence of the fundamental constants also arises in models with a massless dilaton, the scalar partner of the graviton.[13]

On the other hand, a clear regularity was recently discovered in the distribution of galaxies in the direction of the Galactic north and south poles, with a characteristic scale of $128h^{-1}$ Mpc (where $h \sim 0.5-1$; h is a constant characterizing the uncertainty in the value of the Hubble constant).[14] This periodicity can be explained by oscillations of the gravitational constant G_N in time.[15–18] For example, in Ref. 18 a model with an oscillating massive scalar field, which is cosmological ''dark matter'' and can be observed according to oscillations of the gravitational constant, is studied. This model explains well the periodicity in the distribution of galaxies which was observed in Ref. 14. Variations of the solar year, which were discovered in the deposits of corals and sea mollusks, can also serve as indirect evidence of a change in G_N with time.[19] The value of the period

1

of these variations (~ 400–600 million years) is close to the values required to explain the periodicity in the distribution of the galaxies.

Modern limits on the possible temporal variations of different fundamental constants can be found in Refs. 20–29. For example, the strictest limits for the weak-interaction constant were obtained from an analysis of the operation of the natural nuclear reactor in Oclo[b]: $|\Delta G_F|/G_F < 0.02$ (where $\Delta G_F = G_F^{\text{Oclo}} - G_F^{\text{now}}$) or $|\dot{G}_F/G_F| < 10^{-11}$ yr^{-1}. This value exceeds the limits obtained earlier from an analysis of nucleosynthesis processes ($|\Delta G_F|/G_F < 0.06$)[28] and analysis of the β decay of ^{40}K ($|\dot{G}_F/G_F| < 10^{-10}$ yr^{-1}).[29] However, it should be kept in mind that these limits were obtained under the assumption that all the other constants are constant, which makes estimates of this kind less reliable. It has not been ruled out that variations of the constants are interrelated and that the effect due to a change in one constant can be compensated by a change in another constant.

Double β decay is of interest in itself in the problem of the change in the fundamental constants with time. The probability of ordinary β decay is proportional to G_F^2, while the probability of 2β decay goes as $\sim G_F^4$ (since 2β decay is of second order in the weak interaction); G_F is the Fermi constant. For this reason, if, for example, in ordinary β decay the effect due to a change in G_F in time is compensated by the a change in other fundamental constants, then this effect could still come through in 2β decay. Therefore the study of the time dependence of the rate of 2β decay can give additional (and possibly also unique) information about the possible change in G_F with time. We recall in this connection that the age of minerals and meteorites is determined by radioisotopic methods (β and α decay). For this reason, when attempts are made to observe a time dependence of the rate of β decay of ^{40}K, for example, then the change in G_F can be masked by ''incorrect'' dating of the sample under study.

Let us compare the rate of 2β decay obtained in modern counter experiments to the rate of the same process obtained in geochemical experiments, which carry information about the rate of 2β decay in the past. Geochemical experiments are based on the separation of the products of 2β decay from ancient minerals followed by isotopic analysis of the products. The observation of an excess quantity of a daughter isotope attests to the presence of 2β decay of the initial isotope and makes it possible to determine its half-life. Minerals containing tellurium, selenium, and zirconium have been investigated and the half-lives of ^{130}Te, ^{128}Te, ^{82}Se, and ^{96}Zr have been measured. Since the age of the samples investigated ranged from ~ 28 million years up to 4.5 billion years, it is possible in principle to extract from geochemical experiments information about the values of G_F in the past — right back to the time when the solar system formed (4.5 billion years ago). If the value of G_F oscillates with time, then these oscillations can be observed.

Let us examine systematically all the existing experimental data.

1.^{82}**Se**. The most accurate ''present-day'' value of the half-life of ^{82}Se with respect to the $2\beta(2\nu)$ channel was obtained in the NEMO-2 track detector:[30] $T_{1/2} = [0.83 \pm 0.09(\text{stat}) \pm 0.07(\text{syst})] \times 10^{20}$ yr (the statistical error is given at the 68% reliability level). The following values were obtained in geochemical experiments: $T_{1/2} = (1.30 \pm 0.05) \times 10^{20}$ yr[31] (the average value for 17 independent measurements; the age of the samples ranged from 80 million years up to 4.5 billion years) and $T_{1/2} = (1.2 \pm 0.1) \times 10^{20}$ yr[32] (the age of the sample ~ 1 billion years). Comparing these results shows that

the present-day value of the half-life ^{82}Se is different from the half-life in the past (this effect is at the level $\geqslant 3\sigma$). If this is due to a change in the value of the weak-interaction constant, then $\Delta G_F/G_F \approx -0.1$, and with the errors taken into account the possible range of values is approximately $-(0.02-0.2)$.[c] It is interesting to note that the only experiment with a meteorite (age ~ 4.5 billion years) gave the following value of the half-life: $T_{1/2}=(1.03^{+0.33}_{-0.42})\times 10^{20}$ yr.[33] This value is identical, to within the error limits, to the present-day value of $T_{1/2}(^{82}$Se$)$, but it does not preclude a possible difference from the present-day value by $\sim 50\%$. If G_F does not change in time linearly but rather oscillates, then for a fortuitous value of the period of the oscillations, the values of G_F at present could coincide exactly with the value 4.5 billion years ago, for example.

The accuracy of the present-day values of the half-life of ^{82}Se can be increased to several percent, and such measurements will be performed on the NEMO-3 track detector.[34] The basic problem is to increase the accuracy of the results of geochemical measurements. Modern mass spectrometry makes it possible to perform such measurements with an accuracy of several percent (see, for example, Ref. 35). The age of the samples is also determined, as a rule, with an accuracy of several percent. The main uncertainty in geochemical experiments with ^{82}Se is due to the determination of the effective ''retention'' age of daughter ^{82}Kr in minerals. To solve this problem it is necessary to pick samples which have a well-known geological history and for which the retention age of ^{82}Kr can be accurately determined.

2. ^{96}**Zr.** The present-day value of the half-life of ^{96}Zr with respect to the $2\beta(2\nu)$ channel was recently measured with the NEMO-2 detector and equals $T_{1/2}=[2.1^{+0.8(\text{stat})}_{-0.4(\text{stat})}\pm 0.2(\text{syst})]\times 10^{19}$ yr.[36] A geochemical experiment (the age of the sample was 1.7 billion years) gave the value $T_{1/2}=(3.9\pm 0.9)\times 10^{19}$ yr.[39] One can see that the present-day value of the half-life is approximately half the value in the past. However, the errors in both experiments are quite large and it cannot be concluded unequivocally that the half-lives are different. New measurements with ^{96}Zr, in which the half-life will be determined with an accuracy of 10% using the NEMO-3 detector,[34] and new geochemical measurements with good accuracy (10–20%) could clarify this situation. We note that in the present case of 2β decay of ^{96}Zr it is a metal (^{96}Mo) that forms and not a gas, as in the 2β decay of ^{130}Te, ^{128}Te, and ^{82}Se (^{130}Xe, ^{128}Xe, and ^{82}Kr, respectively). This gives hope that the problems involved in determining the retention age of the decay products will be considerably smaller in this case.

3. ^{130}**Te,** ^{128}**Te.** Only data from geochemical measurements are available for these isotopes. Although the ratio of the half-lives of these isotopes has been determined to a high degree of accuracy ($\sim 3\%$),[35] the absolute values of $T_{1/2}$ differ substantially in different experiments. One group of authors[32,37,38,40] presents the values $T_{1/2}\approx 0.8\times 10^{21}$ yr for ^{130}Te and $T_{1/2}\approx 2\times 10^{24}$ yr for ^{128}Te, while another group[31,35] gives $\approx (2.5-2.7)\times 10^{21}$ and $\approx 2.7\times 10^{24}$ yr, respectively. In addition, as a rule, experiments with ''young'' samples (~ 100 million years) give $\sim (0.7-0.9)\times 10^{21}$ yr for ^{130}Te, whereas experiments on ''old'' (>1 billion years) samples give $\sim (2.5-2.7)\times 10^{21}$ yr.[d]

Evidetnly, this is mainly due to an incorrect estimate of the retention age of xenon in old samples (see the discussion in Ref. 38), but it cannot be ruled out that, to some

extent, this could be also due to a change in G_F. In this connection it is very important to perform precise measurements of the present-day value of the half-life ^{130}Te. Such measurements will be performed in the near future in an experiment with low-temperature TeO$_2$ detectors[41] and with the NEMO-3 track detector.[34] It is also obvious that new geochemical measurements with samples of different age and accuracy $\sim 10\%$ are required. This problem can be solved only by careful selection of the experimental samples (with well-known history and with a possibility of determining accurately the xenon retention age) and by using highly sensitive mass spectrometry. Unfortunately, a direct measurement of the half-life $T_{1/2}(^{128}$Te$)$ is virtually impossible because it is too long.

In summary, analysis has shown the following:

1. A discrepancy exists between the values of the half-life of ^{82}Se which were obtained in modern counter experiments and in geochemical measurements.

2. The ^{96}Zr data show the same tendency as the ^{82}Se data — the present-day value of $T_{1/2}$ is less than the values obtained in geochemical measurements. However, the measurement errors make it impossible to conclude unequivocally that the half-lives are unequal.

3. Geochemical measurements on young samples give lower values of $T_{1/2}(^{130}$Te$)$ as compared to measurements on old samples.

These discrepancies can all be explained (at least partially) by a change in G_F with time. If this is indeed the case, then this will have the most serious consequences for modern physics and astrophysics. But, this is why it is necessary to confirm (or refute) reliably the reality of these discrepancies. This can be done only by performing new and more accurate measurements. We propose the following:

● precise laboratory measurements of the present-day values of the $2\beta(2\nu)$-decay half-lives of ^{82}Se, ^{96}Zr, and ^{130}Te should be performed;

● new, precise measurements of the half-lives of ^{82}Se, ^{96}Zr, and ^{130}Te in geochemical experiments should be performed; for each isotope it is desirable to perform measurements with samples of different age in order to follow the character of the dependence of G_F on the time;

● the possibility of performing geochemical experiments with ^{100}Mo, ^{116}Cd, ^{124}Sn, ^{110}Pd, and ^{76}Ge should be investigated, and if possible such measurements should be performed; this will make it possible to enlarge the range of isotopes investigated, since the half-lives of ^{100}Mo, ^{116}Cd, and ^{76}Ge have already been measured in direct (counter) experiments,[42–44] while the half-lives of ^{124}Sn and ^{110}Pd can be measured in the near future.

For all isotopes listed above, the products of 2β decay are not gases, so that the problems related to their being retained in the minerals studied can be expected to be much smaller.

[a])e-mail: barabash@vxitep.itep.ru

[b])The first analysis[26] of the Oclo data for a possible change in the fundamental constants with time was made in Ref. 27.

[c])These values were obtained using the dependence $T_{1/2} \sim G_F^{-4}$. However, if the dependence $\sim G_F^{-2}$ is used, which takes into account the possible ''incorrect'' dating of the sample, then the corresponding values will be approximately $-(0.04 - 0.4)$. We note, however, that in the case of oscillations the interpretation of the experimental data becomes much more complicated and depends on the value of the period of the oscillations.

[d])It is interesting to note that even in the very carefully performed study in Ref. 35 a half-life $\sim 0.9 \times 10^{21}$ yr was obtained for samples with an age of 28 million years (see Table VI in Ref. 35), though the final result (2.7×10^{21} yr) was obtained by studying samples whose age was >1 billion years.

[1] P. A. M. Dirac, Nature **139**, 323 (1937).

[2] E. Teller, Phys. Rev. **73**, 801 (1948).

[3] L. D. Landau, ''On the quantum theory of fields,'' in *Niels Bohr and the Development of Physics,* edited by W. Pauli, Pergamon Press, London, 1955.

[4] C. Brans and R. H. Dicke, Phys. Rev. **124**, 925 (1961).

[5] B. S. De Witt, Phys. Rev. Lett. **13**, 114 (1964).

[6] G. Gamow, Phys. Rev. Lett. **19**, 759 (1967).

[7] F. J. Dyson, ''The fundamental constants and their time variation,'' in *Aspects of Quantum Theory*, edited by A. Salam and E. P. Wigner, Cambrige University Press, Cambridge, 1972.

[8] A. Chodos and S. Detweiler, Phys. Rev. D **21**, 2167 (1980).

[9] W. J. Marciano, Phys. Rev. Lett. **52**, 489 (1984).

[10] Y.-S. Wu and Z. W. Wang, Phys. Rev. Lett. **52**, 489 (1984).

[11] E. W. Kolb, M. J. Perry, and T. P. Walker, Phys. Rev. D **33**, 869 (1986).

[12] J. Griego and H. Vucetich, Phys. Rev. D **40**, 1904 (1989).

[13] T. Damour and A. M. Polyakov, Nucl. Phys. B **423**, 532 (1994).

[14] T. J. Broadhurst, R. S. Ellis, D. C. Koo, and A. S. Szalay, Nature **343**, 726 (1990).

[15] T. C. Hill, P. J. Steinbardt, and M. S. Turner, Phys. Lett. B **252**, 343 (1990).

[16] M. Morikawa, Astrophys. J. **362**, L37 (1990).

[17] M. Salgado, D. Sudarsky, and H. Quevedo, Phys. Rev. D **53**, 6771 (1996).

[18] M. Salgado, D. Sudarsky, and H. Quevedo, Phys. Lett. B **408**, 69 (1997).

[19] P. D. Sisterna and H. Vucetich, Phys. Rev. Lett. **72**, 454 (1994).

[20] J. H. Irvine and L. Humphreys, Prog. Part. Nucl. Phys. **17**, 59 (1986).

[21] J. Rich, O. D. Lloyd, and M. Spiro, Phys. Rep. **151**, 239 (1987).

[22] H. V. Klapdor-Kleĭngrothaus and A. Staudt, *Non-Accelerator Particle Physics*, IOP Publishers, 1994 [Russian translation, Nauka, Moscow, 1997].

[23] P. Sisterna and H. Vucetich, Phys. Rev. D **41**, 1034 (1990).

[24] D. A. Varshalovich, S. A. Levshakov, and A. Yu. Potekhin, Usp. Fiz. Nauk **163**, 111 (1993).

[25] D. A. Varshalovich, V. E. Panchuk, and A. V. Ivanchick, Pis'ma Astron. Zh. **22**, 8 (1996) [Astron. Lett. **22**, 6 (1996)].

[26] T. Damour and F. Dyson, Nucl. Phys. B **480**, 37 (1996).

[27] A. I. Shlyakhter, Nature **264**, 340 (1976).

[28] H. Reeves, Rev. Mod. Phys. **66**, 193 (1994).

[29] F. J. Dyson, in *Aspects of Quantum Theory,* edited A. Salam and E. P. Wigner, Cambridge University Press, Cambridge, 1972, p. 213.

[30] R. Arnold, C. Augier, J. Baker *et al.*, submitted to Nucl. Phys. A, 1998.

[31] T. Kirsten, E. Heusser, O. Kaether *et al.*, in *Proceedings of the International Symposium on Nuclear Beta Decay and Neutrino, Osaka'86*, edited by T. Kotani *et al.*, World Scientific, Singapore, 1987, p. 81.

[32] W. J. Lin, O. K. Manuel, G. L. Cumming *et al.*, Nucl. Phys. A **481**, 477 (1988).

[33] S. V. S. Murty and K. Marti, Geochim. Cosmochim. Acta **51**, 163 (1987).

[34] A. S. Barabash, in *Proceedings of the International Conference ''Neutrino'96''*, edited by K. Enqvist *et al.*, World Scientific, Singapore, 1997, p. 374.

[35] T. Bernatowicz, J. Brannon, R. Brazzle *et al.*, Phys. Rev. C **47**, 806 (1993).

[36] R. Arnold, C. Augier, J. Baker *et al.*, submitted to Nucl. Phys. A (1998).

[37] N. Takaoka and K. Ogata, Z. Naturforsch. Teil A **21**, 84 (1966).

[38] O. K. Manuel, in *Proceedings of the International Symposium on Nuclear Beta Decay and Neutrino. Osaka'86,* edited by T. Kotani *et al.*, World Scientific, Singapore, 1987, p. 71.

[39] A. Kawashima, K. Takahashi, and A. Masuda, Phys. Rev. C **47**, R2452 (1993).

[40] N. Takaoka, Y. Motomura, and K. Nagano, Phys. Rev. C **53**, 1557 (1996).

[41] A. Alessandrello, C. Brofferio, C. Bucci *et al.*, Nucl. Instrum. Methods Phys. Res. A **370**, 241 (1996).

[42] D. Dassie, R. Eschbach, F. Hubert *et al.*, Phys. Rev. D **51**, 2090 (1995).

[43] R. Arnold, C. Augier, A. Barabash *et al.*, Z. Phys. C **72**, 239 (1996).

[44] M. Gunther, J. Hellmig, G. Heusser *et al.*, Phys. Rev. D **55**, 54 (1997).

Translated by M. E. Alferieff

Cross-singular dips in the NMR absorption line of polycrystals with isolated spin pairs

O. V. Falaleev and L. G. Falaleeva

L. V. Kirenskiĭ Institute of Physics, Siberian Branch of the Russian Academy of Sciences, 660036 Krasnoyarsk, Russia

Cross-singular dips at the center of the spectra of polycrystals of Pake systems, i.e., systems containing well-isolated pair groupings, are obtained by numerical calculations of the NMR absorption line for a 10-spin ($I = 1/2$) model. The physical reason for such dips is the behavior of the flip-flop component of the interpair dipole–dipole interactions (''6/5 factor''). Cases of experimental manifestation of cross-singular dips are noted. © *1998 American Institute of Physics.* [S0021-3640(98)01713-7]

PACS numbers: 76.60.Es

Cross-singular dips are the most intriguing of the so-called cross-singular effects observed under certain conditions in well-resolved NMR spectra of polycrystalline samples.[1,2] These dips are due to the presence of a singularity in the distribution of frequencies corresponding to crossing spectral lines of individual crystallites over the spectrum of a polycrystal.

Thus far only cross-singular dips in the ^{19}F NMR spectra of octahedral molecules and ions with quite high anisotropy of the chemical shift of the fluorine nuclei have been studied conclusively both theoretically and experimentally.[3–5] Recently, cross-singular dips have been observed experimentally in the spectra of fluorine systems of a more general type, specifically, systems that do not contain isolated groupings.[6] Unfortunately, there are still no experimental data on cross-singular dips predicted theoretically for isolated two-spin systems with an anisotropic chemical shift of the resonating nuclei.[7,8]

The existence of a similar cross-singular dip can be easily verified by an analytical calculation of the NMR line shape for a polycrystal containing isolated pairs of quadrupolar nuclei with $I = 1$. As in the case of nuclei with an anisotropic chemical shift, the flip-flop component of the dipole–dipole interaction between the spins is responsible for the dip. The difference lies only in the fact that instead of the ''9/4 factor,'' describing the increase in the second moment of the crossing spectral components, in the second case a ''6/5 factor'' appears.[9] For this reason, it is quite obvious that there is a possibility of observing cross-singular dips in polycrystalline spectra of quadrupolar nuclei, despite the absence of experimental data (with the apparent exception of the [2]D NMR spectrum of polytetramethylene oxide[10]).

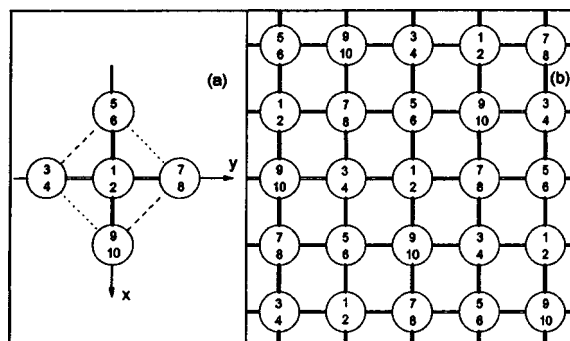It is much more difficult to substantiate the cross-singular nature of the dips that are

FIG. 1. Model of a 10-spin grouping (a) used for the calculations, including a variant with ''quasicyclic'' boundary conditions (b).

sometimes recorded in purely dipole–dipole systems. For example, for several years now it has been impossible to arrive at a consensus concerning the origin of the unusual dip positively recorded in the ^{1}H NMR spectrum of dellaite ($Ca_6(OH)_2(Si_2O_7)$), which contains well-isolated proton pairs.[1,2] The main reason is that in contrast to the cases considered above, where the fine structure of the spectrum of a polycrystal can be described by chemical shifts or quadrupole effects, while the dipole–dipole interaction between spins of an isolated pair participates in the formation of the cross-singular dip, in the purely dipole–dipole case[11] with a Pake structure of the spectrum[12] one must deal with interpair dipole–dipole interactions, encompassing all the surrounding spins and taken into account in the Gaussian broadening model, which, as is well known, cannot give any anomalies.[13] Another important circumstance is that the ''6/5 factor,'' long drawing attention in connection with Pake systems,[14–16] has still not been convincingly demonstrated experimentally even for H_2O molecules undergoing 180° flipping (proton exchange),[17] where the analogy with quadrupolar ($I=1$) nuclei is most obvious. Unfortunately, our attempt[18] to obtain a cross-singular dip on the basis of the four-spin ($I=1/2$) model, which is conventionally employed to analyze the interpair dipole–dipole interaction, was also unconvincing.

Nonetheless, active searches for alternative reasons explaining the anomaly under discussion have inevitably returned to the cross-singular mechanism as the only possible one. For this reason, we decided to perform numerical calculations of the NMR line shape using a sufficiently large number of spins so that it was possible to form quasicontinuous components of the Pake doublet. Using the standard procedure of Ref. 19 and the computer resources available to us, we decided on a 10-spin system. The present work is essentially a computater simulation with five identical, rigid (i.e., no 180° flipping) spin pairs. Despite the fact that such a system has no direct relation to any particular compound, it does make it possible to obtain a general idea about the character of the collective manifestation of interpair dipole–dipole interactions in Pake objects.

The first results justified our expectations. They were obtained for an equidistant arrangement of spin pairs of unit length, oriented along the z axis, in the xy plane. As is shown in Fig. 1a, where the numbers in the circles enumerate the spins, the central pair at the origin $(0, 0, \pm 0.5)$ is surrounded on four sides $(\pm r, \pm r, \pm 0.5)$ by equivalent pairs. The distance r makes it possible to vary the degree of isolation of the Pake pairs,
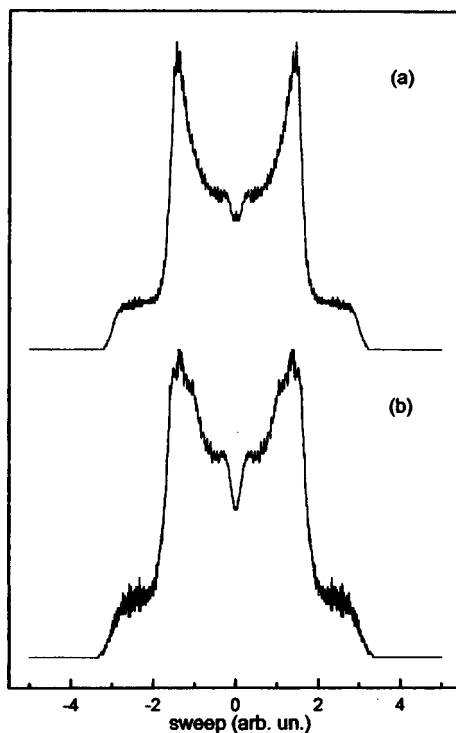
FIG. 2. Computed spectra of a polycrystal for variants (a) and (b), respectively.

i.e., the degree to which the Pake spectrum, determined by intrapair interactions, can be resolved. It is convenient to divide the set of 40 dipole–dipole constants between spins belonging to different pairs, of which in the general case only 18 are different, into groups in accordance with the interpair distances: r (shown by the double and heavy lines in Fig. 1a), $r\sqrt{2}$ (dashed and dotted lines), and $2r$ (not shown). As a rule, the interactions in the first group are strongest, though on account of anisotropy they often fade into the background.

Figure 2a shows the NMR spectrum obtained for a ''polycrystal'' with the optimum value $r = 2.5$. As one can see, a central dip, whose depth concedes essentially nothing to the depth observed experimentally in dellaite, comes through here distinctly. As r increases, the dip vanishes; as r decreases, the dip broadens and the structure of the entire spectrum becomes more complicated (pairs become nonisolated). Such behavior is characteristic for cross-singular dips.[1,4] Besides r, the depth of a dip depends on the orientation of the spin pairs and on the geometry of their relative arrangement, which often causes the dip to vanish.

As noted above, in real crystals (even, for example, in zeolites) it is difficult to find isolated clusters which in turn have several well-isolated pairs of nuclei. Ordinarily, the environments of all pairs are approximately the same, whereas in the model employed (Fig. 1a) for each central pair there are four peripheral pairs; this fundamentally differs from the typical experimental situation. The way out of the situation could be the use of
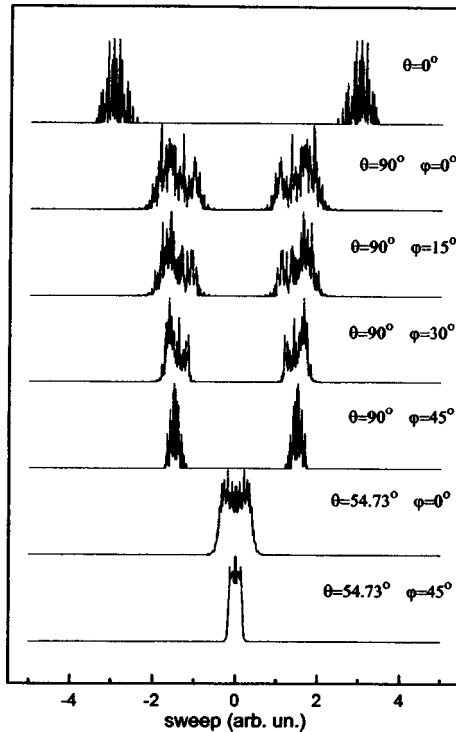
FIG. 3. Typical examples of spectra of a single crystal (variant (b)) for certain orientations of the magnetic field vector.

cyclic boundary conditions,[20] but the limited number of spins makes it possible to use them more or less rigorously only for a one-dimensional arrangement of pairs, which we propose to study in detail.

Nonetheless, sacrificing the possibility of taking into account all of the interactions, except those marked by the double and thick lines, we used unique ''quasicyclic'' boundary conditions that made it possible to place each of five spin pairs into an identical environment. Topologically, such a model can be represented by any five-vertex object (star, triangular bipyramid, and so on), but we prefer the two-dimensional representation shown in Fig. 1b. Of course, because of the small number of pairs, even such a model cannot claim to analyze real situations, but nonetheless it does expand the possibilities of studying the spectral manifestations of interpair dipole–dipole interactions. Compared with the previous model, here the contribution of interpair interactions is artificially increased. The number of different dipole–dipole constants decreases from 18 to 6, but for the components of Pake doublets quasicontinuity can be preserved in a ''single crystal,'' as one can see in Fig. 3. Only the first spectrum (for $H_0 \| z$) is an exception. Here, because of the high symmetry, only two interpair interaction constants are different. (When only one interpair constant remains, the components become line-like.)

The central dip for such a model with $r = 2.5$ came through much more distinctly in the spectrum presented in Fig. 2b for a ''polycrystal.'' It is interesting that despite the

inherent broadening of the Pake structure of the spectrum, the width of the dip remained constant (which is why its depth increased). On the whole, the ''quasicyclized'' model gives a cross-singular dip that is more stable against a change in orientation and relative arrangement of the spin pairs.

We note here that all of the spectra in Figs. 2 and 3 are represented by histograms with a step size of 0.01 arbitrary units on the horizontal sweep scale (sweep of the frequency, magnetic field, and so on). No measures were taken to smooth the computed curves. The spectra of the polycrystals were obtained by the usual summation of the single-crystal spectra with the spherical angles changing by steps $\Delta\theta = \Delta\varphi = 1°$ and with weighting factors $\sin\theta$. The obvious noisiness of the computed spectra is due not to computational errors (say, because of diagonalization of large matrices) but rather to the actual discrete nature of the spectra because of the small number of spins. The doublet structure sometimes seen on the components is also due to the small number of pairs.

The cross-singular nature of the dips, obtained computationally, in the Pake spectra follows from the fact that the values of the second moments of the individual components in the resolved doublets actually equal 5/6 of the Van Vleck values, and they strictly equal the Van Vleck values only for $\theta \approx 55°$. For this reason, at the central point of the spectrum, which is the only location where the spectral lines cross, the width of the lines suddenly increases by a small amount, which results in a ''shortfall'' of the integrated intensity when averaging over θ and φ.

The most surprising circumstance, making it difficult to perceive the cross-singular mechanism, is that the much stronger change in the width of the components as a result of the anisotropy of the interpair Van Vleck second moment (clearly illustrated in Fig. 3) is essentially not manifested in the spectrum of a polycrystal, since it is ''smeared'' over the entire spectrum.

It follows from the results presented above that the cross-singular dip is an integral property of the Pake NMR spectra. However, it is very sensitive to the relative arrangement of Pake pairs, which often causes the dip to vanish. The experimental observation of a cross-singular dip apparently requires spectra which are better resolved than the spectra ordinarily observed in rigid crystal hydrates. Thus, besides the aforementioned dellaite, we call attention to the distinct cross-singular dip in the ^{1}H NMR spectrum of trichloroacetic acid,[21] although the authors did not point it out. More demonstrative cases exist also. See, for example, Ref. 22, where a strongly expressed dip in the ^{1}H NMR spectrum of partially dehydrated magnesium perchlorate hexahydrate, which was recorded on the derivative as the ''line of reverse phase,'' was interpreted as an additional narrow peak with the corresponding physical conclusions.

To accumulate statistics on the dependence of the depth of a cross-singular dip on the characteristic features of the relative arrangement of pairs it will be necessary to improve the computational method employed, a task for which adequate resources are available. Specifically, the deep analogy with quadrupole systems makes it possible to increase substantially the number of Pake pairs in numerical models, where a nucleus with $I = 1/2$ will play the role of a pair and the Pake splitting will be replaced by quadrupole splitting.

[1] É. P. Zeer, V. E. Zobov, and O. V. Falaleev, *New Effects in the NMR of Polycrystals* [in Russian], Nauka, Novosibirsk, 1991.

[2] A-R. Grimmer and B. Blumich, *Introduction to Solid-State NMR,* Springer-Verlag, Berlin, 1994.

[3] M. L. Afanas'ev, É. P. Zeer, O. V. Falaleev *et al.*, Dokl. Akad. Nauk SSSR **303**, 1396 (1988).

[4] É. P. Zeer, O. V. Falaleev, Yu. N. Ivanov *et al.*, Khim. Fiz. **8**, 1067 (1989).

[5] O. V. Falaleev, M. L. Afanas'ev, and É. P. Zeer, Zh. Strukt. Khim. **35**, 68 (1994).

[6] O. V. Falaleev, O. P. Kukhlevsky, V. N. Voronov *et al.*, *Abstracts of the 13th European Experimental NMR Conference,* Paris, 1996.

[7] E. P. Zeer, O. V. Falaleev, and V. E. Zobov, Chem. Phys. Lett. **100**, 24 (1983).

[8] V. E. Zobov, in *NMR and the Structure of Crystals* [in Russian], Institute of Physics, Siberian Branch of the Russian Academy of Sciences, Krasnoyarsk, 1984.

[9] A. Abragam, *The Principles of Nuclear Magnetism*, Clarendon Press, Oxford, 1961 [Russian translation, Inostr. Lit., Moscow, 1963].

[10] J. P. Beyl, B. Meurer, and P. Spegt, Bruker Report **1**, 6 (1981).

[11] J. H. Van Vleck, Phys. Rev. **74**, 1168 (1948).

[12] G. E. Pake, J. Chem. Phys. **16**, 327 (1948).

[13] A. A. Lundin and B. N. Provotorov, Zh. Éksp. Teor. Fiz. **70**, 2201 (1976) [Sov. Phys. JETP **43**, 1149 (1976)].

[14] F. Reif and E. M. Purcell, Phys. Rev. **91**, 631 (1953).

[15] B. Pedersen, Chem. Phys. Lett. **1**, 373 (1967).

[16] N. Boden and Y. K. Levine, Mol. Phys. **29**, 1221 (1975).

[17] B. Pedersen, J. Chem. Phys. **39**, 720 (1963).

[18] O. V. Falaleev, O. P. Kukhlevskiĭ, and L. G. Falaleeva, Preprint 450F [in Russian], Institute of Physics, Siberian Branch of the Russian Academy of Sciences, Krasnoyarsk, 1987.

[19] S. K. Garg, J. A. Ripmeester, and D. V. Davidson, J. Magn. Reson. **35**, 145 (1979).

[20] M. Engelsberg, I. J. Lowe, and J. L. Carolan, Phys. Rev. B **7**, 924 (1973).

[21] M. E. Stoll, A. J. Vega, and R. W. Vaughan, J. Chem. Phys. **69**, 5458 (1978).

[22] R. A. Gazarov, V. F. Chuvaev, and V. I. Spitsyn, Dokl. Akad. Nauk SSSR **222**, 859 (1975).

Translated by M. E. Alferieff

On the screening of the leptonic charge of a body by a condensate of charged bosons

B. V. Martemyanov

Institute of Theoretical and Experimental Physics, 117218 Moscow, Russia

The hypothesis of leptonic charge raises the problem of its neutralization, which is crucial for the stability of material bodies. The screening of the leptonic charge by a charged bosonic condensate is considered. The screening length and the structure of the skin layer are investigated in both the nonrelativistic and relativistic regimes. © *1998 American Institute of Physics.* [S0021-3640(98)00313-2]

PACS numbers: 12.60.Cn, 03.75.Fi

1. Introduction

The possible existence of leptonic charge coupled to leptonic photons has been discussed for a long time.[1] The stability of bodies with respect to this additional interaction requires neutralization of the leptonic charge unless the leptonic interaction is extremely small.[1] The neutralization by antineutrinos does not ensure the stability of a body:[2] the pressure of degenerate gas of antineutrinos occurs to be disruptive for the bodies. Another possibility is neutralization by a condensate of leptonic bosons (scalar superpartners of antineutrinos, for example). In this case the neutralization is complete everywhere except for a skin layer,[2] and the stability of the skin layer requires the constant of leptonic interaction α_l to be smaller than approximately $10^{-12}(\alpha^6)$ (Ref. 3). In Ref. 3 the thickness of the skin layer was obtained from a dimensional analysis of the coupled Klein–Gordon and Poisson equations for scalar field ϕ and leptostatic potential A_0. The existence of the solutions for these equations was not considered. Here we present numerical solutions of the Klein–Gordon–Poisson equations in some specific cases. We will consider small pieces of matter, balls with radius equal to several screening lengths, uniformly charged by electronic charge. Two limiting cases will be analyzed: the nonrelativistic and relativistic regimes for the Klein–Gordon equation for the boson field ϕ. In the nonrelativistic case there exists a continuous set of solutions corresponding to different degrees of neutralization (from 0 to 100%). In the relativistic case (massless bosons) only the totally screened solution (100% neutralization) exists. The latter statement is in agreement with the analysis of Ref. 4, where the problem of screening (although in another context and for a different distribution of screened charge) was also considered.

In Sec. 2 we derive the system of equations to be solved. In Sec. 3 we present numerical solutions of this system in the nonrelativistic case. In Sec. 4 we consider the relativistic case. In the Conclusion we outline the prospects for future investigations.

2. The set of equations

Let A_μ be a leptonic gauge field coupled to a massive boson field Φ of mass m that has leptonic charge $e = -g$ and electrons that have leptonic charge g. The Lagrangian of the system is

$$L = -\frac{1}{4}F_{\mu\nu}^2 + (\partial_\mu - ieA_\mu)\Phi^*(\partial_\mu + ieA_\mu)\Phi - m^2\Phi^*\Phi - j_\mu^{\text{ext}}A_\mu, \tag{1}$$

where $F_{\mu\nu} = \partial_\mu A_\nu - \partial_\nu A_\mu$, $j_\mu^{\text{ext}} = g\delta_{\mu 0}n\,\theta(R-r)$ is the current of leptonic charge of the electrons, and n is the density of electrons inside a body of radius R. The equations of motion for fields A_μ and Φ are

$$-(\partial_\mu + ieA_\mu)^2\Phi - m^2\Phi = 0,$$

$$\partial_\nu^2 A_\mu = j_\mu^{\text{ext}} + e\Phi^*(i\overset{\leftrightarrow}{\partial}_\mu - 2eA_\mu)\Phi. \tag{2}$$

In the static limit for the leptonic gauge field,

$$A_i = 0, \quad \dot{A}_0 = 0,$$

and for the bosonic ground state $\Phi = e^{-iEt}\phi$. We derive from Eqs. (2) the coupled Klein–Gordon and Poisson equations for the scalar field ϕ and leptostatic potential A_0 (Δ is used for the Laplacian operator):

$$(E + gA_0)^2\phi + \Delta\phi = m^2\phi,$$

$$-\Delta A_0 = gn\,\theta(R-r) - g2(E + gA_0)\phi^2. \tag{3}$$

These equations describe the screening of leptonic charge of the body by a condensate (E is the ground-state energy of the bosons) of oppositely charged bosons. In what follows we will solve these equations numerically for nonrelativistic and ultrarelativistic bosons.

3. Nonrelativistic regime

Consider first the heavy boson, $gA_0 \ll m$, $E = m + \delta E$, $\delta E \ll m$ (nonrelativistic limit). Then from Eqs. (3) one gets

$$\delta E\,\phi \approx \left(-\frac{1}{2m}\Delta - gA_0\right)\phi, \quad -\Delta A_0 \approx gn\,\theta(R-r) - g2m\phi^2. \tag{4}$$

To cast these equations into scale-invariant form, we make the following substitutions:

$$r \to r(g^2nm)^{-1/4}, \quad \delta E = \epsilon \to \epsilon(g^2n/m)^{1/2},$$

$$-gA_0 = V \to V(g^2n/m)^{1/2}, \quad \phi \to \phi(n/2m)^{1/2}. \tag{5}$$

Then Eqs. (4) become

$$\epsilon\phi = \left(-\frac{1}{2}\Delta + V\right)\phi, \quad \Delta V = \theta(R-r) - \phi^2. \tag{6}$$

We solve Eqs. (6) with the following boundary conditions at the origin:

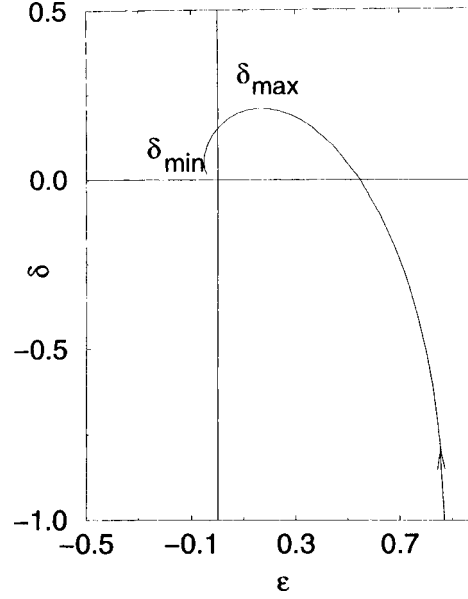$$V(0) = 0, \quad V'(0) = 0, \quad \phi(0) = 1 + \delta, \quad \phi'(0) = 0.$$

FIG. 1. The curve in the $\epsilon-\delta$ parameter plane for which there are solutions of Eqs. (6). The arrow on the curve corresponds to strengthening of the screening.

For a given δ we are looking for the lowest eigenvalue ϵ for which $\phi \to 0$ at infinity. The resulting curve in the $\epsilon-\delta$ plane is shown in Fig. 1 ($R=5$). This curve starts from the point $\epsilon=0.85$, $\delta=-1$, for which

$$\phi=0, \quad V(r)=\frac{1}{6}r^2 (r<R), \quad V(r)=\frac{1}{2}R^2-\frac{1}{3}R^3/r(r>R).$$

The eigenvalue $\epsilon=0.85$ is close to the lowest energy eigenvalue of the harmonic oscillator:

$$V(r)=\frac{1}{6}r^2, \quad \omega=1/\sqrt{3}, \quad \epsilon=\frac{3}{2}\omega=\sqrt{3}/2.$$

The solution corresponding to $\epsilon=0.85$, $\delta=-1$ is the totally unscreened solution ($\phi=0$), and its charge is equal to $Q_{\max}=4\pi/3R^3$ (in units of $n(g^2nm)^{-3/4}$). As one goes from the starting point along the curve of Fig. 1 the solution become more and more screened. There are two qualitatively different regimes in this process of strengthening of the screening effect. The first one corresponds to having δ grow from -1 to $\delta_{\max}=0.21$, for which ϕ is growing everywhere and $V(r)$ is declining everywhere (see Figs. 2 and 3). The second regime corresponds to having δ decrease from $\delta_{\max}$ to $\delta_{\min}=0.02$, for which ϕ decreases and flattens at the origin and has a slight bump near the surface of the body, while $V(r)$ grows and flattens at the origin and decreases slightly near the surface of the body (see Figs. 4 and 5). The end point on the curve ($\delta=\delta_{\min}$)
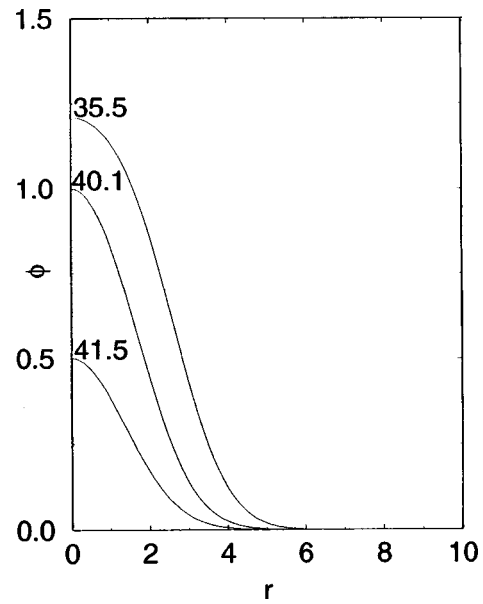
FIG. 2. The growing of the boson field ϕ for the first regime of strengthening of the screening. The numbers near the curves are the values of $Q/4\pi$.
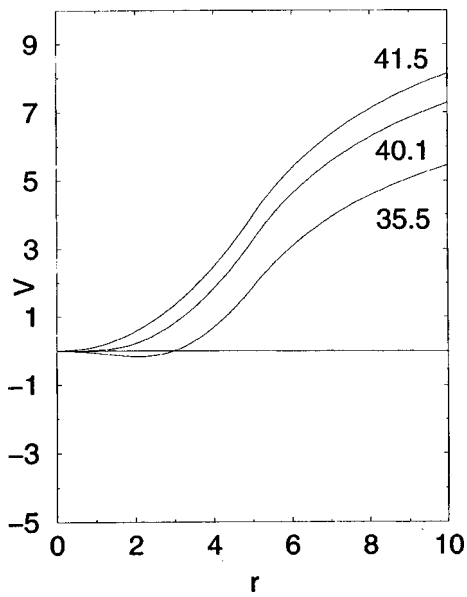

FIG. 3. The lowering of the potential energy of bosons $V(r)$ for the first regime of strengthening of the screening. The numbers near the curves are the values of $Q/4\pi$.
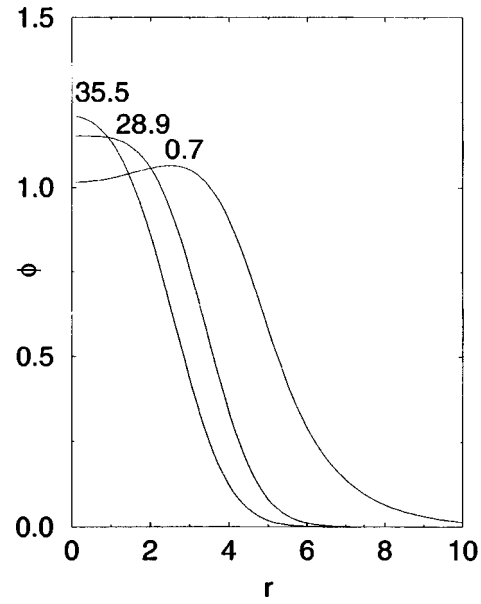
FIG. 4. The flattening of the boson field ϕ near the origin and bumping of ϕ near the surface from inside for the second regime of strengthening of the screening. The numbers near the curves are the values of $Q/4\pi$.
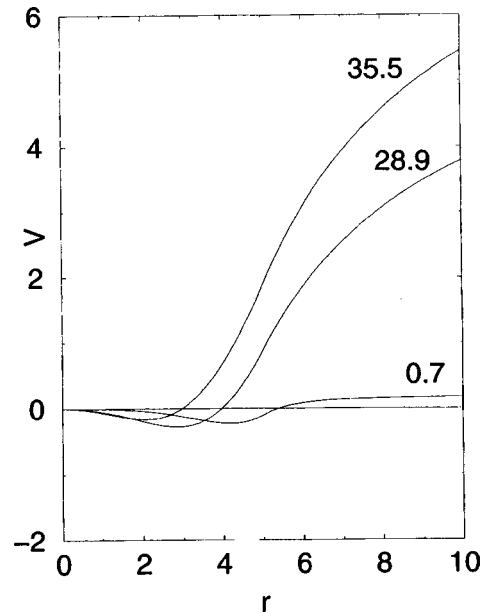

FIG. 5. The flattening of the potential energy of bosons $V(r)$ near the origin and the falling off of $V(r)$ near the surface from inside for the second regime of strengthening of the screening. The numbers near the curves are the values of $Q/4\pi$.
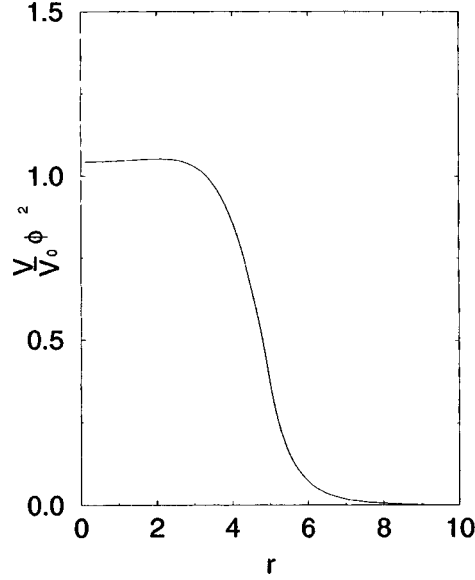
FIG. 6. The negative of the charge density of the boson field $(V/V_0)\phi^2$ for the case of complete screening of the leptonic charge of a body by a massless boson field.

corresponds to a total charge which is 60 times smaller than the initial unscreened charge of the body $(Q_{min} = \frac{1}{60}Q_{max})$. From physical arguments it is clear that a completely screened solution with zero charge $(Q_{min} \to 0)$ is possible.

4. Relativistic regime

To consider the relativistic limit we put $m = 0$ in Eqs. (3). We set also $E = 0$ by shifting the potential A_0, and for the boson potential energy $V = -gA_0$ and boson field ϕ we arrive at the equations

$$V^2\phi + \Delta\phi = 0, \quad \Delta V = g^2 n\,\theta(R - r) + g^2 2V\phi^2. \tag{7}$$

As in the nonrelativistic case, to cast these equations into scale-invariant form we make the following substitutions:

$$r \to r(g^2 n)^{-1/3}, \quad V \to V(g^2 n)^{1/3}, \quad \phi \to \phi(n/2|V(0)|)^{1/2}. \tag{8}$$

The substitutions (8) reduce Eqs. (7) to the scale-invariant form

$$V^2\phi + \Delta\phi = 0, \quad \Delta V = \theta(R - r) - \frac{V}{V(0)}\phi^2. \tag{9}$$

We solve Eqs. (9) with the following boundary conditions at the origin:

$$V(0) = -\epsilon, \quad V'(0) = 0, \quad \phi(0) = 1 + \delta, \quad \phi'(0) = 0.$$
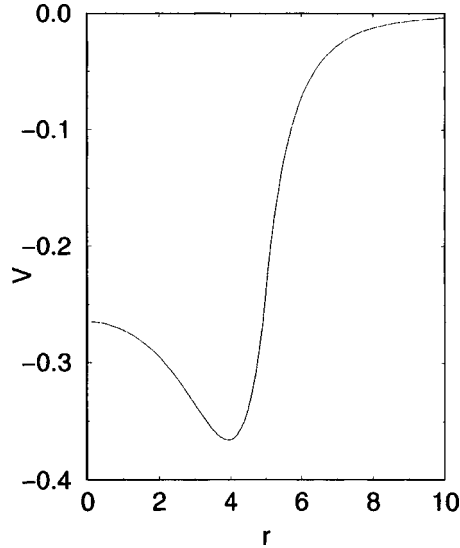
FIG. 7. The potential energy of massless bosons for the case of complete screening of the leptonic charge of a body by a massless boson field.

There is only one point for δ and ϵ at which V and ϕ go to zero at infinity. This is the point

$$\delta = 0.021, \quad \epsilon = 0.265.$$

Figures 6 and 7 present the corresponding solutions for ϕ and V ($R=5$). The charge of the body is completely screened. This follows from both the asymptotic form of V, which has no Coulomb tail, and from the uniqueness of the solution (there aren't different degrees of neutralization), and it is in agreement with the analysis of Ref. 4. Physically it is obvious that for massless bosons any electric field associated with the growth of the potential near the surface produces boson–antiboson pairs. The bosons neutralize the body and the antibosons go away to infinity.

5. Conclusion

We have presented numerical solutions of the Klein–Gordon–Poisson equations for the screening of hypothetical leptonic (electronic) charge of small balls of matter, with radius equal to several (five in our case) screening lengths, by a condensed boson field. We considered both the nonrelativistic and relativistic regimes for the Klein–Gordon equation for the boson field. In the nonrelativistic case we found a continuous set of solutions corresponding to different degrees of neutralization (from 0% to 100%). In the relativistic case (massless bosons) the Eqs. (7) have only a completely screened solution (corresponding to 100% neutralization).

There is an interesting problem of considering larger (in comparison to the screening length) balls of matter. From the numerical point of view, computations for $R=10$ (in units of the screening length) or larger are difficult. From the physical point of view it is

clear that the structure of the skin layer is the same for all bodies of sufficiently large size if all they are completely screened by bosons. This problem is now under investigation.

[1] L. B. Okun, ''A remark on leptonic photons,'' a manuscript in Russian presented at the ITEP theoretical seminar, June 1972.

[2] S. I. Blinnikov, A. D. Dolgov, L. B. Okun, and M. B. Voloshin, Nucl. Phys. B **458**, 52 (1996).

[3] B. V. Martemyanov, JETP Lett. **66**, 547 (1997).

[4] J. E. Mandula, Phys. Lett. B **69**, 495 (1977).

Diffusion of circularly polarized light in a disordered medium with large-scale inhomogeneities

E. E. Gorodnichev,[a] A. I. Kuzovlev, and D. B. Rogozkin

Moscow Engineering Physics Institute, 115409 Moscow, Russia

It is shown that in the presence of diffusion of electromagnetic waves in random media containing large discrete scatterers, circular polarization can persist even after the radiation flux is isotropized. For scattering exactly in the backward direction, this effect is manifested as an increase in the interference contribution to the cross-polarized component of the intensity as the size of the scatterers increases. © *1998 American Institute of Physics.* [S0021-3640(98)00413-7]

PACS numbers: 42.25.Fx, 42.25.Ja

1. Explaining the nature of polarization phenomena in the presence of multiple scattering of light in disordered media containing inhomogeneities of different size is still a topical problem. In recent years this problem has been attracting great interest in connection with various applications in the diffusion spectroscopy of biological tissues and of scattering media with a complicated structure.[1-3]

In the present letter the phenomenon of slow decay of circular polarization during the diffusion of light in random media with large (larger than the wavelength) scatterers is explained. It is shown that circular polarization can persist even after the radiation flux is isotropized. This effect was discovered comparatively recently in experiments and in Monte Carlo calculations.[2] How the persistence of circular polarization is manifested in the presence of coherent backscattering of polarized light is also discussed. It has been shown that this effect is directly related with the increase, observed back in the first experiments,[4,5] in the coherent contribution to the cross-polarized component of the intensity on reflection of light from disordered samples with large particles. This behavior was confirmed by direct numerical calculations,[6] but heretofore its physical reason remained unclear.

The calculations were performed for a disordered system of transparent latex particles in water. This is the system that is most often used in experiments.[1,2,4,5]

2. As analysis shows, in a scattering medium there is a fundamental difference between the behavior of the electric field vector in linearly and circularly polarized waves. In the case of the propagation of a linearly polarized wave, the direction of the electric field vector follows the light beam — the beam remains linearly polarized along the entire propagation trajectory.[7] The depolarization observed in the presence of multiple scattering in thick layers is a result of the chaotic variations that arise in the directions of polarization of waves moving along different random trajectories. It arises si-

multaneously with isotropization of the radiation with respect to directions.[2] In this sense a measurement of the degree of polarization of linearly polarized light in a random medium does not give anything new as compared with a measurement of the angular distribution of the scattered waves (here we are not concerned with the polarization characteristics of the interference of waves in the exactly backward direction).

The situation is different in the case of the propagation of circularly polarized light. Although circular polarization is not preserved along the propagation trajectory, in media with large-scale inhomogeneities it decays over distances much greater than the isotropization length (transport length l_{tr}). Depolarization starts as the variations arising in the phases of two linearly cross-polarized fields (into a superposition of which the incident circularly polarized wave can be decomposed) increase and is of a coherent nature. The depolarization rate depends only on how smooth the propagation trajectories of the waves are and, as will be shown below, in the case of scattering by large-scale inhomogeneities it is proportional to the average of the fourth power of the single-scattering angle (in contrast to the isotropization rate $1/l_{tr}$, which is proportional to the square of the angle). In this connection, a study of the circular polarization should yield new information about the medium, different from the information contained in the angular distribution of the scattered light.

3. Let a clockwise-polarized light beam be incident on a layer ($0 < z < L$) of a medium consisting of large spherical scatterers in a direction normal to the surface. We assume that the refractive index n of an individual center is real and differs little from 1 ($n - 1 \ll 1$). In this situation single scattering occurs predominantly in the forward direction[8] and the mean free path l is much shorter than the transport length l_{tr} ($l_{tr} = l/(1 - \langle \cos\gamma \rangle)$, $\langle \cos\gamma \rangle$ is the average cosine of the single-scattering angle).

We shall characterize the polarization state of the light by the Stokes parameters I, Q, U, and V, which satisfy a vector transfer equation.[9] In the present problem the vector equation decomposes into a system of equations for I and Q and a separate equation for V; the third Stokes parameter $U = 0$ because of the azimuthal symmetry of the problem,[9]

The system of equations for I and Q has the same form as in the case of an unpolarized beam.[9,10] According to Refs. 9 and 10, for multiply scattered radiation the ratio Q/I is small, and to a first approximation the influence of polarization effects on the value of the intensity I can be neglected. In this approximation the equation for I is identical to the scalar transfer equation:[9]

$$\left\{ \mu \frac{\partial}{\partial z} + n_0 \sigma \right\} I(z, \mu) = n_0 \int d\mathbf{n}' a_1(\mathbf{n} \cdot \mathbf{n}') I(z, \mu'), \tag{1}$$

where n_0 is the number of scattering particles per unit volume, σ is the total scattering cross section (we assume the medium to be nonabsorbing),

$$a_1(\cos\gamma) = \frac{1}{2} (|A_\parallel(\cos\gamma)|^2 + |A_\perp(\cos\gamma)|^2)$$

is the differential cross section, $A_\parallel$ and $A_\perp$ are the amplitudes for single scattering of waves polarized parallel and perpendicular to the scattering plane, and $\cos\gamma = \mathbf{n} \cdot \mathbf{n}'$. The

unit vectors $\mathbf{n} = \{\sin\theta\cos\varphi, \sin\theta\sin\varphi, \cos\theta\}$ and $\mathbf{n}' = \{\sin\theta'\cos\varphi', \sin\theta'\sin\varphi', \cos\theta'\}$ determine the direction of motion of a photon before and after a scattering event, $\mu = \cos\theta$, $\mu' = \cos\theta'$.

The equation for the fourth Stokes parameter V — the difference of the intensities of the waves polarized clockwise and counterclockwise — is[9]

$$\left\{ \mu\frac{\partial}{\partial z} + n_0\sigma \right\} V(z,\mu) = n_0 \int d\mathbf{n}' a_2(\mathbf{n}\cdot\mathbf{n}') V(z,\mu'), \qquad (2)$$

where

$$a_2(\cos\gamma) = \mathrm{Re}\, A_{\parallel}^*(\cos\gamma) A_{\perp}(\cos\gamma).$$

The boundary condition for Eqs. (1) and (2) is $I(z=0,\mu>0) = V(z=0,\mu>0) = 1$.

Since

$$\int d\mathbf{n}' a_2(\mathbf{n}\cdot\mathbf{n}') < \sigma,$$

the equation (2) for V can be regarded as a scalar equation describing transfer in a certain ''absorbing'' medium. The effective absorption is characterized by the cross section

$$\sigma_{\mathrm{dep}} = \int d\mathbf{n}'(a_1(\mathbf{n}\cdot\mathbf{n}') - a_2(\mathbf{n}\cdot\mathbf{n}')) \qquad (3)$$

and describes the damping of circular polarization as a result of scattering by inhomogeneities of the medium. The quantity $l_{\mathrm{dep}} = (n_0\sigma_{\mathrm{dep}})^{-1}$ plays the role of the mean free path with respect to depolarizing collisions.

In the case of Born scatterers ($k_0 a(n-1) \ll 1$, where a is the radius of a scatterer, $k_0 = 2\pi/\lambda$ is the wave number, and λ is the wavelength of the light) the amplitudes are related as $A_{\parallel}(\cos\gamma) = A_{\perp}(\cos\gamma)\cos\gamma$,[8] and the depolarization cross section equals

$$\sigma_{\mathrm{dep}} = \pi \int_0^{\pi} \sin\gamma\, d\gamma |A_{\perp}(\cos\gamma)|^2 (1-\cos\gamma)^2. \qquad (4)$$

According to Eq. (4), under conditions such that single scattering is predominantly by small angles, circular polarization should decay over distances greater than the isotropization length l_{tr} of the light flux: $l_{\mathrm{dep}} \sim l/\langle\gamma^4\rangle \ll l_{\mathrm{tr}} \sim l/\langle\gamma^2\rangle$.

For weakly refracting ($n-1 \ll 1$) spherical particles the form factor $|A_{\perp}|^2$ averaged over an angular range $\Delta\gamma > \lambda/a$ decreases at small angles as $1/\gamma^4$ (Refs. 8 and 9), and the ratio $l_{\mathrm{dep}}/l_{\mathrm{tr}}$ is proportional to the logarithm of the characteristic single-scattering angle:

$$l_{\mathrm{dep}}/l_{\mathrm{tr}} \simeq \begin{cases} 2\ln(2k_0 a), & k_0 a(n-1) \ll 1 \\ 3\ln 1/(n-1), & k_0 a(n-1) \gg 1 \end{cases}. \qquad (5)$$

The large value of the ratio $l_{\mathrm{dep}}/l_{\mathrm{tr}}$ is due to the sharply anisotropic character of single scattering. If the differential cross section decreases more slowly than $1/\gamma^4$ (for example, $1/\gamma^3$ according to the Guinier–Greenstein law (Ref. 9)), the ratio $l_{\mathrm{dep}}/l_{\mathrm{tr}}$ is of the order of 1, and depolarization sets in simultaneously with isotropization of the beam.

Equations (1) and (2) in the limit $l_{tr} \ll L \ll l_{dep}$ describe radiation diffusion in the medium and they can be solved in the transport approximation[9] or, when analyzing the passage of radiation through thick layers of matter, in the simplest approximation — the equation of spatial diffusion.[5,9]

4. We shall employ the spatial-diffusion approximation to calculate the polarization of photons which have passed through a thick $(L > l_{tr})$ layer of matter. In this approximation the angular distribution of the radiation is assumed to be close to isotropic, and the solution of Eqs. (1) and (2) can be represented in the form

$$I(z,\mu) = \frac{1}{4\pi}\left(I(z) + \mu l_{tr}\frac{\partial I(z)}{\partial z}\right), \quad V(z,\mu) = \frac{1}{4\pi}\left(V(z) + \mu l_{tr}\frac{\partial V(z)}{\partial z}\right). \tag{6}$$

The quantities $I(z)$ and $V(z)$ appearing in Eq. (6) satisfy the diffusion equations

$$\frac{\partial^2 I(z)}{\partial z^2} = 0, \quad \frac{\partial^2 V(z)}{\partial z^2} - \frac{3}{l_{tr}l_{dep}}V(z) = 0. \tag{7}$$

The boundary conditions for Eq. (7) are conditions at the effective boundaries of the medium,[5,9]

$$I(z = -z_0) = V(z = -z_0) = 1, \quad I(z = L + z_0) = V(z = L + z_0) = 0, \tag{8}$$

where z_0 is the extrapolated length. The exact value of z_0 depends on the characteristics of single scattering, but $z_0 \simeq 0.71 l_{tr}$ to within an error of 1%.[9]

The solution of the problem (6)–(8) is well known (see, for example, Refs. 5 and 9). For the ratio V/I — the helicity of the radiation which has passed through the layer — we find[b)]

$$\frac{V}{I} = \frac{(L + 2z_0)/l_c}{\sinh[(L+2z_0)/l_c]} \simeq \begin{cases} 1, & L < l_c \\ 2[(L+2z_0)/l_c]\exp(-(L+2z_0)/l_c), & L > l_c \end{cases}, \tag{9}$$

where $l_c = (l_{tr}l_{dep}/3)^{1/2}$ is the characteristic decay length of circular polarization in the case of passage through a thick layer of a nonabsorbing medium. Therefore for thicknesses in the range $l_{tr} < L < l_c$ the light flux remains circularly polarized despite the almost isotropic angular distribution.

It is of interest to compare the expression obtained for the decay length of circular polarization with the experimental data and the results of numerical simulations.[2] The decay lengths of linear and circular polarizations in a disordered medium consisting of a suspension of latex particles in water (the relative index of refraction of the particles $n \simeq 1.19$) were determined in Ref. 2. In a medium with large inhomogeneities the linear polarization decays over distances l_L which are essentially identical to l_{tr}.[2] The results of calculations of $l_{tr}/l_c = (3l_{tr}/l_{dep})^{1/2}$ on the basis of Eq. (3) according to the Mie formulas[8] are presented in Fig. 1 along with the values of l_L/l_c obtained from experiments and Monte Carlo calculations. An analysis shows that the small difference in the results could be due to the procedure used in Ref. 2 to determine the lengths l_L and l_c.

5. The slow decay of circular polarization, studied above, should always appear when the discussion concerns the correlation of cross-polarized fields. The point is that the correlation function of the cross-polarized fields can be represented as a sum of the Stokes parameters U and V: $\langle E_\parallel E_\perp^* \rangle = 4\pi(U - iV)/c$ (Ref. 8). The quantity U, as a
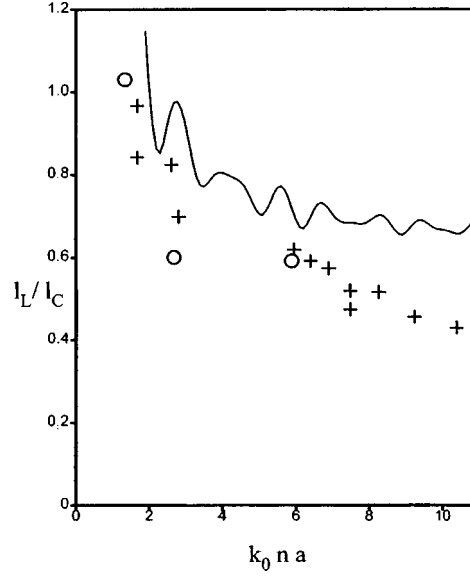
FIG. 1. Ratio of the linear and circular polarization decay lengths in a disordered medium. Solid curve — result of the present work; $\bigcirc$ — experiment of Ref. 2; $+$ — result of statistical simulation.[2]

component of the linear polarization, decays as the light flux is isotropized. For this reason, the large-scale behavior of the correlation function of cross-polarized fields in a medium with large scattering particles is determined by V.

We shall show that the persistence of circular polarization explains the increase, observed even in the first experiments on coherent backscattering,[4,5] in the backscattering factor for cross-polarized waves as the the inhomogeneities of the medium increase in size. This mechanism was confirmed in Ref. 6 by direct numerical integration of the transfer equation, but heretofore its physical reason has remained unclear.

From the relations derived in Ref. 11 (see also Ref. 6) between the interference corrections to the matrix elements of the Green's function of the vector transfer equation and the value of the matrix elements themselves it follows that the coherent contribution to the intensity of the reflected light polarized perpendicular to the incident light can be represented as

$$I_\perp^{(coh)} = \frac{1}{2}(I_\parallel - I_\perp + V),\tag{10}$$

where $I_\parallel$ and $I_\perp$ are the intensities of the incoherently scattered waves polarized parallel and perpendicular to the incident waves. This formula is valid for scattering precisely in the backward direction for close-to-normal angles of incidence of the radiation.

For a disordered medium with large particles $I_\parallel \simeq I_\perp$,[4,5] i.e., in the presence of incoherent backscattering of linearly polarized light the reflected flux is essentially completely depolarized. In this connection the backscattering gain for the cross-polarized component of the reflected light equals
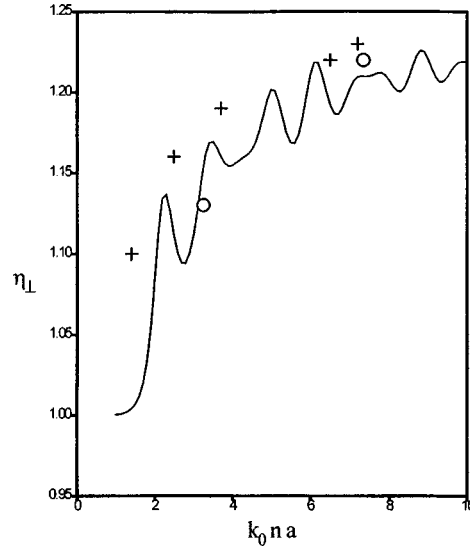
FIG. 2. Gain for backscattering of cross-polarized light. Solid curve — calculation using Eq. (11); $\bigcirc$ — experiment of Ref. 4; $+$ — result of numerical integration of the vector transfer equation.[6]

$$\eta_\perp = \frac{I_\perp^{(\text{coh})} + I_\perp}{I_\perp} \simeq 1 + \frac{V}{I} \tag{11}$$

and in accordance with the foregoing considerations it should increase as the scattering particles increase in size. The validity of this is illustrated in Fig. 2, which presents the experimental results of Ref. 4, the results of numerical integration of the transfer equation,[6] and the calculations performed on the basis of Eq. (11). All data are presented for latex particles in water. The values of V and I appearing in Eq. (11) were calculated in the transport approximation (the differential cross section was replaced by an isotropic cross section with the total cross section equal to the transport cross section).[9] The cross sections themselves were calculated according to the Mie theory.[8]

[a] e-mail: gorod@theor.mephi.msk.su

[b] For light scattered directly forward ($\mu = 1$) the second Stokes parameter $Q = 0$ from symmetry considerations, and the degree of polarization $P = \sqrt{V^2 + Q^2}/I$ always equals the helicity.

[1] F. C. MacKintosh, J. X. Zhu, D. J. Pine, and D. A. Weitz, Phys. Rev. B **40**, 9342 (1989).

[2] D. Bicout, C. Brosseau, A. S. Martinez, and J. M. Schmitt, Phys. Rev. E **49**, 1767 (1994).

[3] S. G. Demos and R. R. Alfano, Opt. Lett. Opt. Lett. **21** 161 (1996); Diffusing Photons in Turbid Media (special issue) Appl. Opt. **36,** 9 (1997).

[4] M. P. van Albada, M. B. van der Mark, and A. Lagendijk, Phys. Rev. Lett. **58**, 361 (1987).

[5] P. E. Wolf, G. Maret, E. Akkermans, and R. Maynard, J. Phys. (Paris) **49**, 63 (1988).

[6] M. I. Mishchenko, J. Opt. Soc. Am. A **9**, 978 (1992).

[7] S. M. Rytov, Dokl. Akad. Nauk SSSR **18**, 2 (1938).

[8] R. Newton, *Scattering of Waves and Particles*, 2nd ed., Springer-Verlag, New York, 1982 [Russian translation of 1st ed., Mir, Moscow, 1969].

[9] H. C. van de Hulst, *Multiple Light Scattering*, Academic Press, New York, 1980.

[10] E. E. Gorodnichev and D. B. Rogozkin, Zh. Éksp. Teor. Fiz. **107**, 209 (1995) [JETP **80**, 112 (1995)].

[11] A. A. Golubentsev, Izv. Vyssh. Uchebn. Zaved. Radiofiz. **27**, 734 (1984).

Translated by M. E. Alferieff

Diffusion-broadened line shape near a turning point

D. A. Shapiro and M. G. Stepanov

Institute of Automation and Electrometry, Siberian Branch of the Russian Academy of Sciences, 630090 Novosibirsk, Russia

The absorption spectrum of a gas with a large Doppler width and soft collisions between particles is studied. The particles are assumed to have a nonlinear dependence of the resonance frequency on velocity. The shape of the narrow peak in the spectrum resulting from an extremum of this dependence is calculated analytically for the first time. In the absence of collisions it has a characteristic asymmetric shape. Collisions are shown to broaden the line and change its shape. The profile of the probe-field spectrum is obtained for a three-level system with the strong field at an adjacent transition. The components of the Autler–Townes doublet are found to spread and repel each other because of collisions. © *1998 American Institute of Physics.*
[S0021-3640(98)00513-1]

PACS numbers: 33.70.Jg, 34.50.−s, 33.20.−t

An investigation of the resonant interaction of a gas of particles and an electromagnetic wave is a promising way of studying collision processes in gases.[1–3] Of particular interest is the case when collisions can be described as diffusion in velocity space; for example, when the particles are ions in a plasma or heavy atoms in a buffer gas of light atoms. The Landau collision term describes well the spectroscopic effects of ion–ion Coulomb scattering.[4] For some reason the frequency of exact resonance between a wave and a particle can depend on the velocity. If this dependence results from the Doppler shift then it is linear; the spectral line shape within the linear approximation in the field intensity has been calculated previously.[5,6] The first nonlinear corrections to the absorption spectrum due to saturation have been obtained,[7] too.

Besides the effects of saturation and nonlinear interference, the field of a monochromatic wave splits the energy levels of a particle.[8] Consider the interaction of a gas with strong and probe waves resonant to adjacent transitions between intrinsic states of the particle. Without the strong field the dependence of the resonance frequency for the probe wave on the velocity is linear due to the Doppler shift. If one turns on the field, then for each particle there are two resonances between it and the probe wave. Their positions coincide with the Rabi frequencies, which are nonlinear functions of the velocity. However, the computation of the splitting in a system with large Doppler width has been done for the collisionless case only.[9]

Nowadays a challenging task is to get tunable cw UV coherent radiation. Using

stimulated Raman scattering, tunable radiation has been obtained in Na_2, Ne. The ions have higher energy levels, so there is hope of reaching short-wavelength radiation by Raman up-conversion in Ar^+ (Refs. 10 and 11). Thus strong-field effects are of interest for experiment along with soft collisions.

In the present letter we study the absorption spectra of a gas of particles with both soft collisions and a nonlinear resonance frequency $\Omega_R(v)$, the frequency of the field at which the exact resonance between it and a particle with velocity v occurs. In Refs. 5–7 the linear dependence $\Omega_R = kv$ was considered. Here we examine a nonlinear function $\Omega_R(v)$ arising from the interaction with a strong monochromatic wave. The extremum of $\Omega_R(v)$ is of special interest in our consideration. The simplest nonlinearity is quadratic. If particles are concentrated near a velocity v_0, then one can interpret this dependence as a Taylor expansion of Ω_R about v_0 to order $(v - v_0)^2$. If for some v_0 the linear term in the expansion is equal to zero, then it would appear reasonable that the leading term in it is quadratic or that Ω_R is constant. In brief, the quadratic nonlinearity seems sufficient to describe all the new effects associated with nonlinearity.

Let us calculate the spectrum of light absorbed (or emitted) by a monokinetic beam of particles with a given initial velocity v_0 throughout its whole time evolution, the so-called beam spectrum with velocity v_0. After that it is possible to find the absorption spectra for an arbitrary velocity distribution. The spectrum is given by the expression

$$I(\Omega) = \frac{1}{\pi} \operatorname{Re} \int_0^\infty dt\, \Phi(t) e^{-i\Omega t}, \quad \Phi(t) = \left\langle \exp\left(i \int_0^t d\tau\, \Omega_R(v(\tau)) \right) \right\rangle, \tag{1}$$

where $\Phi(t)$ is the correlation function. The width of the beam spectrum is the inverse dephasing time t_D^{-1}. When the dependence of the resonance frequency Ω_R is linear, $\Omega_R(v) = kv$, the correlation function is given by[5,6]

$$\Phi(v_0, t) = e^{ikv_0 t - Dk^2 t^3/3}. \tag{2}$$

Roughly, the deviation of the velocity from its initial value is of the order of $\Delta v(t) \sim \sqrt{Dt}$. Then the phase deviation is

$$\Delta \varphi = \Delta \int_0^t d\tau\, \Omega_R(\tau) \sim t \cdot k\Delta v \sim \sqrt{Dk^2 t^3}.$$

The dephasing happens when the latter reaches π, and thus the spectrum width or the inverse dephasing time is of the order of $t_D^{-1} \sim (Dk^2)^{1/3}$. If the particles decay in time, then one should add $i\Gamma$ to Ω_R or multiply $\Phi(t)$ by $e^{-\Gamma t}$, where Γ is the inverse lifetime of the particles.

When only the integral of $\Phi(t) e^{-i\Omega t}$ over time is of interest, one can reduce the problem to simpler one: there is a source of particles with velocity v_0 and there is a steady-state distribution for the polarization of the particles, $\rho(v)$, which is governed by the equation

$$\left(i(\Omega - \Omega_R) - D \frac{d^2}{dv^2} \right) \rho = \delta(v - v_0), \tag{3}$$

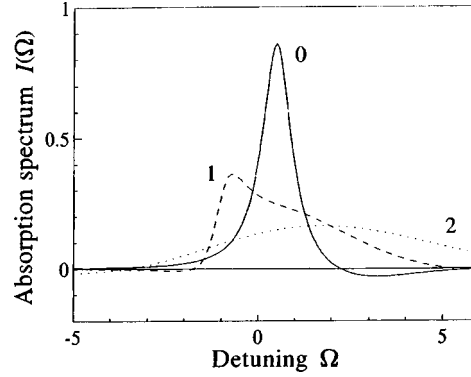and the beam spectrum given by the expression $I_B(\Omega, v_0) = (1/\pi)\operatorname{Re}\int dv\, \rho(v)$.

FIG. 1. Beam spectra with velocity $v_0=n$, $n=0,1,2$ (curve n) at $\Omega_R(v)=v^2/2$, $D=2$.

Let us now consider the case when the dependence of resonance frequency is quadratic, $\Omega_R(v)=\omega+kv+av^2/2$, at least near v_0. If $v_0 \simeq -k/a$, then the linear shift of the resonance frequency with change in velocity vanishes, and so the diffusion of phase arises from the quadratic shift

$$\Delta\varphi \sim t \cdot a(\Delta v)^2 \sim Dat^2,$$

and the spectrum width is of the order of $t_D^{-1} \sim (D|a|)^{1/2}$. These simple estimates are confirmed below by detailed calculations. The point $v=-k/a$, or generally the point where $d\Omega_R/dv=0$, can be called a turning point,[9,12] because if you pull the velocity through it the sign of $d\Omega_R/dv$ (or the direction of Ω_R variation) changes.

We introduce a new variable $z=\alpha(v+k/a)$, $\alpha=(a/2iD)^{1/4}$, $z_0=z|_{v=v_0}$ and decompose ρ, $\delta(v-v_0)$ in a series over functions $\psi_n(z)$

$$\psi_n(z)=\alpha\frac{e^{-z^2/2}H_n(z)}{\sqrt{\pi}2^n n!}, \quad \rho=\sum_{n=0}^{\infty}\rho_n\psi_n(z), \quad \delta(v-v_0)=\sum_{n=0}^{\infty}\psi_n(z)e^{-z_0^2/2}H_n(z_0),$$

where $H_n(z)$ is the nth Hermite polynomial. The quantities ρ_n are found immediately since all ψ_n are eigenvectors of the operator on the left-hand side of (3). After integration over v one gets

$$I_B(\Omega,v_0)=\frac{\sqrt{2}}{\pi}\text{Re}\sum_{n=0}^{\infty}\frac{e^{-z_0^2/2}H_{2n}(z_0)}{2^{2n}n!(2\beta n+x)}=\frac{1}{\pi}\text{Re}\int_0^{\infty}d\tau\frac{e^{(\beta/2-x)\tau}}{\sqrt{\cosh\beta\tau}}\exp\left(-\frac{1}{2}z_0^2\tanh\beta\tau\right). \tag{4}$$

$$\beta=(2Da/i)^{1/2}, \quad x=\beta/2+i(\Omega-\omega-k^2/2a).$$

Thus the spectrum is given by expression (1) with correlation function

$$\Phi(v_0,t)=\frac{e^{i\Omega_R(v_0)t}}{\sqrt{\cosh\tau}}\exp\left(\frac{h}{4}\frac{D(k+av_0)^2}{\Gamma_2^3}(\tau-\tanh\tau)\right), \tag{5}$$

where $h=1-i\,\text{sign}\,a$, $\tau=h\Gamma_2 t$, $\Gamma_2=\sqrt{D|a|}$. Examples of the beam spectrum are plotted in Fig. 1. When $\Gamma_2 \ll \Gamma_1$ one can expand $\tanh\tau$ to order τ^3 and replace $\cosh\tau$ by 1. The

resultant expression coincides with (2). If $\Omega_R(v)$ is a second-degree polynomial, then (5) is the exact solution for the correlation function (1), otherwise it is valid if the characteristic velocity scale of Ω_R is much greater than $(D/|a|)^{1/4}$.

Let us consider the spectrum of particles that are uniformly distributed over velocity. For $\Omega_R(v) = av^2/2$ we have $\Gamma_1 = (Da^2v^2)^{1/3}$, $\Gamma_2 = (D|a|)^{1/2}$, and the spectrum is given by

$$I(\Omega) = \frac{1}{\pi} \operatorname{Re} \int dv \int_0^\infty dt\, \Phi(v,t) e^{-i\Omega t} = \frac{1}{(2D|a|^3)^{1/4}} \operatorname{Re} e^{\pm 3\pi i/8} \frac{\Gamma\left(z + \frac{1}{4}\right)}{\Gamma\left(z + \frac{3}{4}\right)}, \qquad (6)$$

where $z = e^{\pm \pi i/4}(\Gamma + i\Omega)/\sqrt{8D|a|}$, $\Gamma(z)$ is the gamma function, and the upper/lower sign corresponds to positive/negative value of a. $I(\Omega)$ is an asymmetric peak, which has two characteristic widths: a width Γ due to decay, and a diffusion width $(D|a|)^{1/2}$. If Ω is far from $\Omega_R(v_*)$, where v_* is the turning point, then the number of particles N_R resonantly interacting with the field is proportional to $\gamma(v_R)/(d\Omega_R/dv)(v_R)$, where v_R is the resonance frequency, $\Omega \simeq \Omega_R(v_R)$; and $\gamma(v)$ is the width of the beam spectrum with velocity v. Near a turning point $v_R \simeq v_*$ we have $N_R \propto (\gamma(v_*)/(d^2\Omega_R/dv^2)(v_*))^{1/2}$, i.e., the field resonantly interacts with a maximal number of particles when $\Omega \simeq \Omega_R(v_*)$. The spectrum wings are asymmetric:

$$I(\Omega) \simeq \begin{cases} \sqrt{\dfrac{2}{a\Omega}}, & a\Omega > 0, \\[2mm] \dfrac{1}{\sqrt{2|a\Omega|}}\left(\dfrac{\Gamma}{|\Omega|} + \dfrac{D|a|}{4\Omega^2}\right), & a\Omega < 0. \end{cases}$$

When the diffusion is unimportant, $\Gamma \gg (D|a|)^{1/2}$, we have

$$I(\Omega) = \operatorname{Re}\left[\frac{2}{a(\Omega - i\Gamma)}\right]^{1/2} = \frac{\sqrt{|a|}\sqrt{\sqrt{\Omega^2 + \Gamma^2} + a\Omega}}{|a|\sqrt{\Omega^2 + \Gamma^2}}.$$

To calculate the spectrum $I(\Omega)$ one can replace the beam spectrum $I_B(\Omega, v_0)$ by $\delta(\Omega - \Omega_R(v_0))$ if the linear shift $\Omega'(v) = (d\Omega_R/dv)(v)$ does not change substantially within the domain $v - v_0 \sim \gamma(v_0)/\Omega'(v_0)$. In a more general problem one should also require that the integrated intensity of the beam spectrum change insignificantly with velocity v inside this domain. Here we have $\Omega'(v) = av$, $\gamma(v) \sim \Gamma_1$, so the condition of invariance of Ω' looks like $\Gamma_1/\Omega' \ll v$, i.e., $v \gg (D/|a|)^{1/4}$. The widths of this domain and function $\rho(v)$ at $v_0 = 0$ are of the same order. The shift of the resonance frequency in this domain is of the order of Γ_2.

Now we will calculate the probe-wave spectrum in the presence of strong field at the adjacent transition. The strong and probe fields are resonant to transitions between states $|2\rangle$ and $|1\rangle$, $|3\rangle$, respectively. We assume that the two waves are copropagating and denote the projection of the velocity by $v = \mathbf{k}\mathbf{v}/k$, where $\mathbf{k}$ is the wave vector of the strong field. Denoting the detunings from the resonance of the strong and the probe waves as Ω and Ω_μ, we write kinetic equations for off-diagonal elements of density matrix as

$$\rho_{13}(\mathbf{r},\mathbf{v},t) = \rho_{13}(\mathbf{v})\exp(i(\mathbf{k}_\mu-\mathbf{k})\cdot\mathbf{r}-i(\Omega_\mu-\Omega)t),$$

$$\rho_{23}(\mathbf{r},\mathbf{v},t) = \rho_{23}(\mathbf{v})\exp(i\mathbf{k}_\mu\cdot\mathbf{r}-i\Omega_\mu t),$$

$$\left(\Omega_\mu-\Omega_{1B}+iD\frac{d^2}{dv^2}\right)\rho_{31} = G\rho_{32}-G_\mu^*\rho_{21},$$

$$\left(\Omega_\mu-\Omega_{2B}+iD\frac{d^2}{dv^2}\right)\rho_{32} = G^*\rho_{31}-G_\mu^*(\rho_2-\rho_3),$$

$$\Omega_{1B}=\Omega+(k_\mu-k)v+i\Gamma_{13}, \quad \Omega_{2B}=k_\mu v+i\Gamma_{23}, \tag{7}$$

where Γ_{13}, Γ_{23} are the relaxation constants of coherence between $|2\rangle$ and $|1\rangle$, $|3\rangle$; $G=\mathbf{E}\cdot\mathbf{d}_{21}/2\hbar$, $G_\mu=\mathbf{E}_\mu\cdot\mathbf{d}_{23}/2\hbar$, $\mathbf{d}_{ij}$ is the matrix element of the dipole moment, and $\mathbf{E}$ and $\mathbf{E}_\mu$ are the amplitudes of the strong and the probe waves, respectively. To find ρ_{31} and ρ_{32} one must know ρ_2, ρ_3, and ρ_{21}.

The beam spectrum with velocity v has two resonances at the Rabi frequencies[8]

$$\Omega_R^{(1,2)}(v) = k_\mu v+\eta+i\Gamma_+\pm\sqrt{(\eta+i\Gamma_-)^2+|G|^2}, \tag{8}$$

where $2\eta=\Omega-kv$, $2\Gamma_\pm=\Gamma_{13}\pm\Gamma_{23}$. One may think of this as there being two types of particles with different dependence of their resonance frequency on velocity. Strictly speaking, the diffusion causes transitions between these types. But if $|G|\gg(Dk^29)^{1/3}$, then one can treat these two branches of hyperbola (8) independently and apply the theory developed above. Only two elements of the density matrix are mixed by the strong field. Then there are no cubic and higher shifts in the equation for ρ_{32}. One can get this equation by operating with $(\Omega_\mu-\Omega_{1B}+iDd^2/dv^2)$ on (7).

If $k_\mu<k$, then there is one turning point in each of these two frequency branches, located at

$$v_{1,2}=\frac{\Omega}{k}\mp\frac{(2k_\mu-k)|G|}{k\sqrt{k_\mu(k-k_\mu)}}, \quad \Omega_R^{(1,2)}(v_{1,2})=k_\mu\frac{\Omega}{k}\pm\frac{2|G|}{k}\sqrt{k_\mu(k-k_\mu)},$$

$$\frac{d\Omega_R^{(1,2)}}{dv}(v_{1,2})=0, \quad a=\frac{d^2\Omega_R^{(1,2)}}{dv^2}(v_{1,2})=\pm\frac{2(k_\mu(k-k_\mu))^{3/2}}{k|G|}. \tag{9}$$

Here for simplicity we have neglected the decay Γ_{13}, Γ_{23}. The expressions for the coordinates of the turning points (9) coincide with the result for the collisionless case.[9] The curvature of the frequency branch $a\propto1/|G|$, $N_R\propto|G|^{1/2}$, and so the absorption grows with $|G|$.

By analogy with (5) the spectrum is given by

$$I_\mu(\Omega_\mu)\propto\sum_{j=1}^2(-1)^j\mathrm{Re}\int dv\int_0^\infty dt\frac{\exp(i(\Omega_R^{(j)}-\Omega)t)}{\sqrt{\cosh\tau_j}}$$

$$\times\frac{(\Omega_R^{(j)}-\Omega_{1B})(\rho_2-\rho_3)+G^*\rho_{21}}{\Omega_R^{(1)}-\Omega_R^{(2)}}\exp(h_j(\Gamma_{j1}/\Gamma_2)^3(\tau_j-\tanh\tau_j)), \tag{10}$$
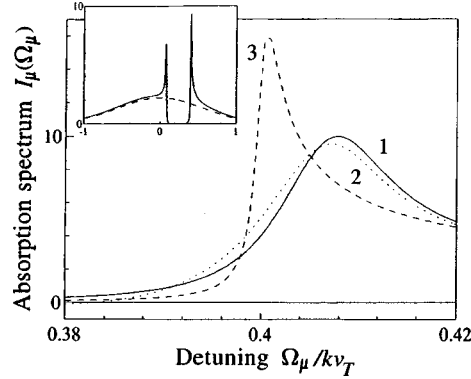
FIG. 2. Absorption spectra $I_\mu(\Omega_\mu)$ in arbitrary units. $(Dk^2)^{1/3} = 6.3 \times 10^{-2} k v_T$: numerical calculations (curve *1*) and approximation formula (10) (curve *2*); and $D = 0$ (curve *3*). $\Gamma_{ij} = 10^{-3} k v_T$, $\Omega = 0.3 k v_T$, $|G| = 0.2 k v_T$, $k_\mu = 0.8 k$. The population of levels *1* and *2* coincide. The dashed curve in the inset corresponds to $G = 0$.

$$\Gamma_{j1} = \left(D \frac{d\Omega_R^{(j)}}{dv} \right)^{1/3}, \quad h_{1,2} = 1 \mp i \, \mathrm{sign}(k - k_\mu), \quad \Gamma_2 = \left(\frac{2Dk_\mu |k - k_\mu|}{\Omega_R^{(1)} - \Omega_R^{(2)}} \right)^{1/2}, \quad \tau_j = h_j \Gamma_2 t.$$

The probe-wave spectrum is illustrated in Fig. 2. In the inset there are two narrow peaks that come from the turning points. Curve *1* is derived from numerical solution of coupled diffusion equations for the whole 3×3 density matrix with the friction force and collisional mixing of the frequency branches taken into account.

The diffusion width Γ_2 of each narrow peak in the spectrum is found to be much less than the width $\Gamma_1 = (Dk_\mu^2)^{1/3}$ resulting from the linear shift. Their ratio is $\Gamma_2/\Gamma_1 = (2\Gamma_1 \kappa/|G|)^{1/2}$, where $\kappa = (k/k_\mu - 1)^{3/2} k_\mu/k$. Such peaks in a plasma (Ar$^+$, 488 and 514.5 nm, V-scheme with common short-lived level 2, $\Gamma_{23} = 250$ MHz) was observed in Ref. 12. If we take the diffusion coefficient measured under similar conditions,[13] then $\Gamma_1 = 170$ MHz and $\Gamma_2 = 20$ MHz. However, the width of the peaks was about 200 MHz. The diffusion width of the peak arises from the nonlinear shift near a turning point; otherwise, the peak would be appreciably wider.

Thus, the absorption spectrum of the gas of particles whose velocity evolves in a diffusional way is obtained. The dependence of the resonance frequency on the velocity of the particle can deviate from linear. The universal shape of the narrow peak in the spectrum (6), which comes from the extremum of the velocity dependence of the resonance frequency, is found. The collisional width of the peak is proportional to the square root of the diffusion coefficient.

[1] S. Rautian and I. Sobelman, Usp. Fiz. Nauk **90**, 209 (1966) [Sov. Phys. Usp. **9**, 701 (1966)].
[2] P. Berman, Adv. At. Mol. Phys. **13**, 57 (1977).
[3] S. Rautian and A. Shalagin, *Kinetic Problems of Nonlinear Spectroscopy*, Elsevier, Amsterdam, 1991.

[4] G. Smirnov and D. Shapiro, Zh. Éksp. Teor. Fiz. **76**, 2084 (1979) [Sov. Phys. JETP **49**, 1054 (1979)].

[5] L. Galatry, Phys. Rev. **122**, 1218 (1961).

[6] M. Podgoretsky and A. Stepanov, Zh. Éksp. Teor. Fiz. **40**, 561 (1961) [Sov. Phys. JETP **13**, 393 (1961)].

[7] S. Rautian, Zh. Éksp. Teor. Fiz. **51**, 1176 (1966) [Sov. Phys. JETP **24**, 788 (1967)].

[8] S. Autler and C. Townes, Phys. Rev. **100**, 703 (1955).

[9] O. Bykova, V. Lebedeva, N. Bykova, and A. Petukhov, Opt. Spektrosk. **53**, 171 (1982) [Opt. Spectrosc. (USSR) **53**, 101 (1982)].

[10] A. Feitish, D. Schnier, T. Müller, and B. Wellegehausen, IEEE J. Quantum Electron. **24**, 507 (1988).

[11] A. Apolonsky *et al.*, Phys. Rev. A **55**, 661 (1997).

[12] N. Bykova *et al.*, Preprint ITAM N26-84, Novosibirsk, 1984.

[13] S. Babin and D. Shapiro, Phys. Rep. **241**, 119 (1994).

Low-frequency relativistic electromagnetic solitons in collisionless plasmas

T. Zh. Esirkepov and F. F. Kamenets

Moscow Institute of Physics and Technology, 141700 Dolgoprudnii, Russia

S. V. Bulanov and N. M. Naumova

General Physics Institute, Russian Academy of Sciences, 117333 Moscow, Russia

A relativistic electromagnetic soliton solution in the model of a one-dimensional, unbounded, cold, collisionless plasma is obtained without using the envelope approximation. The breaking of solitons with over-critical amplitudes is observed. The stability of undercritical solitons and the breaking of overcritical solitons are demonstrated by a particle-in-cell computer simulation. © *1998 American Institute of Physics.* [S0021-3640(98)00613-6]

PACS numbers: 52.40.Nk

1. The technique of ultrashort, ultraintense laser pulses has been developing rapidly in recent years.[1] It has called into being a vast area of nonlinear physics describing the dynamics of matter in ultraintense electromagnetic fields. Among the enormous variety of nonlinear effects induced by a relativistically strong laser pulse propagating through a plasma, we will select out as our topic the formation and evolution of relativistic solitary waves.

Electromagnetic solitons with relativistic amplitudes were first investigated by V. A. Kozlov, A. G. Litvak and E. V. Suvorov.[2] Their study was continued in Refs. 3–10. For the most part these studies used the envelope approximation, i.e., they assumed that the solitary solution to be found is a wave packet whose length and frequency are much greater than those of an electron plasma wave.

Electromagnetic relativistic solitons in collisionless plasmas were observed in a PIC-code simulation of the interaction of ultraintense laser radiation with underdense[11] and overdense[12] plasmas. It was shown that the soliton formation is a significant channel of laser-pulse energy transformation.[13]

The solitons obtained in computer simulations, in contrast to theoretical models using the envelope approximation, have lengths and frequencies of the order of the length and frequency of an electron plasma wave and move at nonrelativistic speed.[13]

As is shown in Ref. 11 and 14, the growth of instability induced by Raman scattering plays the key role in the mechanism of decay of a long, relativistically strong laser pulse. If the length of a high-frequency laser pulse is sufficiently greater than the electron plasma wavelength λ_{pe}, the propagation of the pulse through a plasma is inevitably

accompanied by envelope modulation on a scale of the order of the electron plasma wavelength. This modulation is induced by Raman scattering and leads to decay of the pulse.

On the other hand, an intense laser pulse with length sufficiently smaller than the electron plasma wavelength excites wake-field plasma waves and quickly loses energy.

On the basis of this discussion one can suggest that the expected size of a relativistic electromagnetic soliton must be comparable with the electron plasma wavelength λ_{pe}.

The main task of this paper is to investigate such a ''short'' relativistic soliton.

2. Let us consider a model of unbounded, cold, collisionless plasma, described by Maxwell's equations and the hydrodynamic equations of an electron fluid on a fixed ion background:

$$\Delta \mathbf{A} - \mathbf{A}_{tt} - \nabla \varphi_t - \frac{n}{\gamma}(\mathbf{P} + \mathbf{A}) = 0,$$

$$n = 1 + \Delta \varphi, \quad \text{div } \mathbf{A} = 0, \quad \mathbf{P}_t = \nabla(\varphi - \gamma) + \frac{1}{\gamma}(\mathbf{P} + \mathbf{A}) \times \text{curl } \mathbf{P}. \tag{1}$$

Here $n = n_e/n_i$ is the ratio of the electron and ion densities, $n_i = \text{const}$; $\mathbf{P}$ is the generalized momentum of an electron, $\mathbf{P} = \mathbf{p} - \mathbf{A}$; $\gamma^2 = 1 + (\mathbf{P} + \mathbf{A})^2$. The equations are written in dimensionless form with the help of the substitutions $(\omega_{pe}/c)\mathbf{x} \to \mathbf{x}$, $\omega_{pe}t \to t$, $(e/m_e c^2)\mathbf{A} \to \mathbf{A}$, $(e/m_e c^2)\varphi \to \varphi$, $(e/m_e\omega_{pe}c)\mathbf{E} \to \mathbf{E}$, $(e/m_e\omega_{pe}c)\mathbf{B} \to \mathbf{B}$, $(1/m_e c)\mathbf{p} \to \mathbf{p}$, where m_e and e are the electron mass and charge, and $\omega_{pe} = \sqrt{4\pi n_e e^2/m_e}$ is the electron plasma-wave frequency for the undisturbed density $n_e = n_i$ at infinity.

Let us consider the case when all the variables that characterize fields and plasma are independent of y and z, so that $\partial_y = \partial_z = 0$. Denoting $\mathbf{P} = (P^1, P^2, P^3)$ and $\mathbf{A} = (A^1, A^2, A^3)$, we can rewrite Eqs. (1) in terms of the vector components:

$$A_{xx}^1 - A_{tt}^1 - \varphi_{xt} - \frac{n}{\gamma}(P^1 + A^1) = 0,$$

$$A_{xx}^2 - A_{tt}^2 - \frac{n}{\gamma}(P^2 + A^2) = 0, \quad A_{xx}^3 - A_{tt}^3 - \frac{n}{\gamma}(P^3 + A^3) = 0,$$

$$n = 1 + \varphi_{xx}, \quad A_x^1 = 0,$$

$$P_t^1 = \varphi_x - \gamma_x + \frac{1}{\gamma}(A^2 P_x^2 + A^3 P_x^3 + P^2 P_x^2 + P^3 P_x^3),$$

$$P_t^2 + \frac{1}{\gamma}P^1 P_x^2 = 0, \quad P_t^3 + \frac{1}{\gamma}P^1 P_x^3 = 0. \tag{2}$$

We want to find a spatially localized solution corresponding to perturbations of the fields and of the electron density and momentum which move with a constant velocity V. Localization in the spatial coordinate entails the relation $A^1 = 0$.

Let us assume that the solution to be found is induced by an ultraintense, circularly polarized, finite laser pulse propagating through an underdense plasma. (In the one-dimensional model the direction of laser pulse propagation coincides with the x axis).

Let us imagine that before the interaction the laser pulse was outside the plasma, in vacuum. Then the momentum of the laser pulse had only one nonzero component (in the direction of propagation). According to generalized momentum conservation, it is natural to expect that the transverse generalized momentum $\mathbf{P}_\perp$ (averaged over a sufficiently long period) in the region of the solution that we seek should be zero after the interaction. Therefore, the condition $P^2 = P^3 = 0$, which simplifies Eqs. (2) significantly, can be regarded as a strengthened form of the momentum conservation law.

We can also suppose the solution to be circularly polarized as a result of polarization of the initial laser pulse. This condition can be regarded as a strengthened form of the angular momentum conservation law and is a result of the symmetry of Eqs. (2) with respect to rotation in the plane (y,z).

Thus we are looking for a solution of the form (in terms of the new coordinates ξ, τ):

$$\xi = x - Vt, \quad \tau = t,$$

$$A^1 = 0, \quad A^2 + iA^3 = a(\xi)e^{i\omega((1-V^2)\tau - V\xi)},$$

$$P^1 = Vb(\xi), \quad P^2 = P^3 = 0. \tag{3}$$

Note that the components P^2, P^3 can be proved to be zero by making use of the requirement that the solution is localized in space.

After substituting expression (3) into (2) we obtain

$$(\gamma - V^2 b)'' = \frac{b}{\gamma - b}, \quad \frac{a''}{a} = \frac{1}{1 - V^2} \frac{1}{\gamma - b} - \omega^2, \tag{4}$$

where $\gamma = (1 + a^2 + V^2 b^2)^{1/2}$. This system of equations with the boundary conditions

$$a(\infty) = b(\infty) = 0, \quad a(\xi) < \infty, b(\xi) < \infty \tag{5}$$

describes a one-dimensional relativistic electromagnetic soliton propagating through a cold collisionless plasma. The velocity of the soliton is less than speed of light, $V < 1$. The frequency of the soliton is less than the electron plasma frequency, $\omega < 1$.

In the case $V = 0$ the component P^1 vanishes, and the system of equations (4) can be reduced to

$$b = \frac{\gamma \gamma''}{1 + \gamma''}, \quad \frac{a''}{a} = \frac{1 + \gamma''}{\gamma} - \omega^2. \tag{6}$$

These equations are easily integrated with the help of the substitution $a = \sinh u$, $\gamma = \cosh u$, and we obtain:

$$\mathbf{A} = \frac{2\sqrt{1 - \omega^2} \cosh(\xi\sqrt{1 - \omega^2})}{\cosh^2(\xi\sqrt{1 - \omega^2}) + \omega^2 - 1} \exp(i\omega\tau). \tag{7}$$

One can see that the relationship between the maximum soliton amplitude A_0 and the angular velocity of rotation ω of the plane of polarization of the soliton is given by

$$A_0 = \frac{2\sqrt{1-\omega^2}}{\omega^2}.\tag{8}$$

The values of the fields, electron momentum, vector potential, electron density, and gamma factor in the soliton can be written as

$$\mathbf{E} = \left(\frac{2(1-\omega^2)}{\omega} \frac{\sinh(\zeta)}{\cosh^2(\zeta)-1+\omega^2}, \sin(t\omega), -\cos(t\omega) \right) \frac{2\omega\sqrt{1-\omega^2}\cosh(\zeta)}{\cosh^2(\zeta)-1+\omega^2},$$

$$\mathbf{B} = (0, \sin(t\omega), -\cos(t\omega)) \frac{2(1-\omega^2)\sinh(\zeta)}{\cosh^2(\zeta)-1+\omega^2} \left(1 + \frac{2(1-\omega^2)}{\cosh^2(\zeta)-1+\omega^2} \right),$$

$$\mathbf{p} = \mathbf{A} = (0, \cos(t\omega), \sin(t\omega)) \frac{2\sqrt{1-\omega^2}\cosh(\zeta)}{\cosh^2(\zeta)-1+\omega^2},$$

$$n = 1 + \frac{(1-\omega^2)^2(\cosh(4\zeta)-2(2\omega^2-1)\cosh(2\zeta)-3)}{(\cosh^2(\zeta)-1+\omega^2)^3},$$

$$\gamma = 1 + \frac{2(1-\omega^2)}{\cosh^2(\zeta)-1+\omega^2}.\tag{9}$$

Here $\zeta = \sqrt{1-\omega^2}(x-x_0)$. Fig. 1 shows a corresponding graph for the case $A_0 = \sqrt{3}$, $\omega = \sqrt{2/3}$.

Let us consider the series expansion of the solution a, P^1 in powers of the soliton velocity V about zero:

$$P^1(\xi) = Vb_0(\xi) + V^3 b_2(\xi) + O(V^5), \quad a(\xi) = a_0(\xi) + V^2 a_2(\xi) + O(V^4).\tag{10}$$

The function $b_0(\xi)$ defined in the first equation in (6) can be singular when $1 + \gamma'' = 0$. It is obvious that the electron density $n = 1 + \gamma''$ reaches its minimum value when the amplitude $a_0(\xi)$ is maximum. Thus the minimum envelope amplitude A_0 for which the function $b_0(\xi)$ is singular is determined by the condition
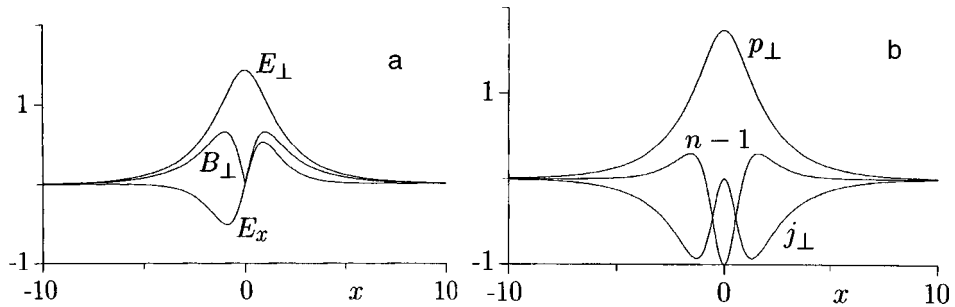

FIG. 1. Electromagnetic fields and the momentum and density of electron fluid in the soliton. a — Fields $E_\perp$, $B_\perp$, E_x. b — Transverse momentum $p_\perp$ and density n of the electron fluid and the transverse current $j_\perp$.
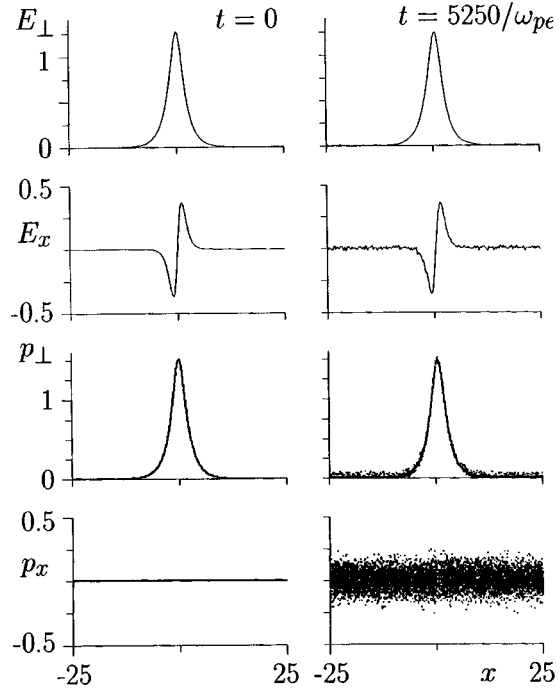
FIG. 2. Stability of a soliton of amplitude $A_0 = 1.5$, given by (7), (9). The transverse and longitudinal electric fields are shown as functions of time along with the transverse and longitudinal momentum of the electrons. The steady-state electron temperature is $T_e \sim (2-4) \times 10^{-3} mc^2$.

$$n|_{\xi=0} \equiv 1 - \frac{4(1-\omega^2)^2}{\omega^4} = 0 \qquad (11)$$
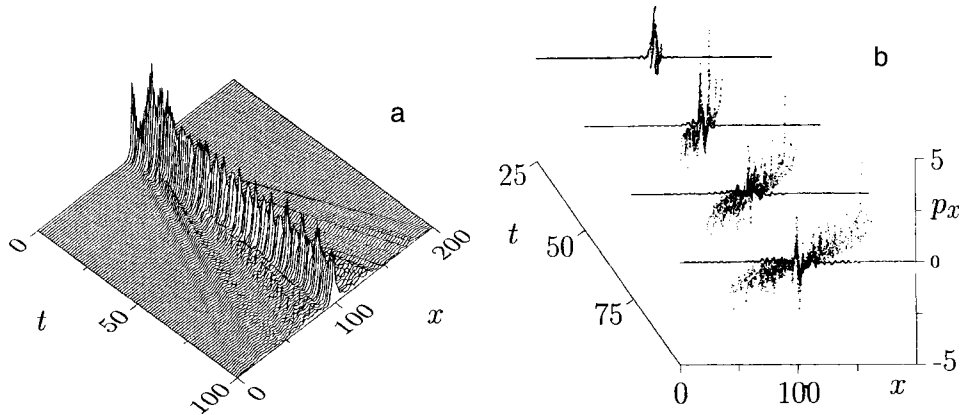

FIG. 3. Breaking of a soliton with overcritical amplitude $A_0 = 3$ and acceleration of the electrons. a — Evolution of the electron transverse momentum averaged over the cell, $p_\perp$. b — Phase plane (x, p_x) in time.

and is equal to $\sqrt{3}$.

We see that there is a critical value of the soliton vector potential at which the longitudinal momentum P^1 of the electron fluid becomes singular and the ''breaking'' of the soliton can take place. One can assume that this process is accompanied by heating and acceleration of some electrons falling at the field maximum.

The possibility of breaking points out an instability of solitons with overcritical amplitudes.

3. To test the solution and to observe possible breaking we carried out numerical simulations using a one-dimensional PIC code. In simulations whose results are presented below, the typical number of particles per cell was 50 and the cell size was $c/(32\pi\omega_{pe})$.

Figure 2 demonstrates the excellent stability of the soliton given by (7), (9). The insignificant damped oscillation in the vicinity of the soliton is a result of the error in the initial electron distribution. This error can be abated by increasing the number of particles per cell and increasing the grid resolution.

In the present calculation the maximum soliton amplitude is $A_0 = 1.5$ and its frequency $\omega = \sqrt{2\sqrt{1+A_0^2}-2}/A_0 \approx 0.8447$. The soliton preserves its shape and amplitude forever (for longer than the code precision permits following it). The error in the initial electron distribution results in plasma heating to temperatures of the order of $(2-4) \times 10^{-3} m_e c^2$.

In the simulation of a soliton with amplitude $A_0 = 3$, which is greater than the critical value, one can observe heating and acceleration of electrons falling at the maximum field region up to energies $(3-5)m_e c^2$. This is a demonstration of soliton breaking (Fig. 3).

[1] G. Mourou, C. P. J. Barty, and M. D. Perry, Phys. Today **51**(1), 22 (January 1998); A. Modena *et al.*, Nature **337**, 606 (1995); K. Nakajima *et al.*, Phys. Rev. Lett. **74**, 4428 (1995); R. Wagner, S. Chen, A. Maksimchuk, and D. Umstadter, Phys. Rev. Lett. **78**, 3125 (1997).

[2] V. A. Kozlov, A. G. Litvak, and E. V. Suvorov, Zh. Éksp. Teor. Fiz. **76**, 148 (1979) [Sov. Phys. JETP **49**, 75 (1979)].

[3] P. K. Shukla, M. Y. Yu, and N. L. Tsintsadze, Phys. Fluids **27**, 327 (1984).

[4] Yu. B. Movsesyants, Zh. Éksp. Teor. Fiz. **91**, 493 (1986) [Sov. Phys. JETP **64**, 289 (1986)].

[5] P. K. Kaw, A. Sen, and T. Katsouleas, Phys. Rev. Lett. **68**, 3172 (1992).

[6] H. H. Kuehl, C. Y. Zhang, and T. Katsouleas, Phys. Rev. E **47**, 1249 (1993).

[7] H. H. Kuehl and C. Y. Zhang, Phys. Rev. E **48**, 1316 (1993).

[8] V. I. Berezhiani and S. M. Mahajan, Phys. Rev. Lett. **73**, 1110 (1994).

[9] H. H. Kuehl and C. Y. Zhang, Phys. Plasmas **2**, 35 (1995).

[10] A. V. Borovskii, Ya. M. Zhileikin, and V. V. Korobkin, J. Quantum Electronics **22**, 1 (1995).

[11] S. V. Bulanov, I. N. Inovenkov, V. I. Kirsanov *et al.*, Phys. Fluids B **4**, 1935 (1992).

[12] S. V. Bulanov, N. M. Naumova, and F. Pegoraro, Phys. Plasmas **1**, 745 (1994).

[13] S. V. Bulanov, T. Zh. Esirkepov, F. F. Kamenets, and N. M. Naumova, Fiz. Plazmy **21**, 584 (1995) [Plasma Phys. Rep. **21**, 550 (1995)].

[14] A. S. Sakharov and V. I. Kirsanov, Phys. Rev. E **49**, 3274 (1994).

Effect of regimes of cooling in a magnetic field on the magnetization of a $La_{0.9}Sr_{0.1}MnO_3$ single crystal

V. E. Arkhipov and V. E. Startsev

Institute of Metal Physics, Urals Branch of the Russia Academy of Sciences, 620219 Ekaterinburg, Russia; International Laboratory for High Magnetic Fields and Low Temperatures, 53-529 Wroclaw, Poland

V. P. Dyakina[a]

Institute of Metal Physics, Urals Branch of the Russia Academy of Sciences, 620219 Ekaterinburg, Russia

J. Klamut

International Laboratory for High Magnetic Fields and Low Temperatures, 53-529 Wroclaw, Poland

Ya. M. Mukovskiĭ

Moscow Institute of Steels and Alloys, 117939 Moscow, Russia

A. Czopnik

Institute of Low Temperatures and Structural Research, 50-950 Wroclaw, Poland

Magnetization measurements were performed on a lanthanum manganite $La_{0.9}Sr_{0.1}MnO_3$ single crystal in the temperature interval 4.2–300 K and magnetic field interval 50 Oe–55 kOe in two sample cooling regimes: 1) cooling down to 4.2 K in a high (55 kOe) magnetic field, and 2) cooling in a ''zero'' field. It is shown that the temperature dependences of the magnetization $M(T)$ are substantially different in these regimes. Pronounced anomalies of $M(T)$ were observed at temperatures $T^* = 103$ K and $T_c = 145$ K. The first anomaly is attributed to a structural transition, while the second one corresponds to a ferromagnet–paramagnet phase transition. The magnetization of a $La_{0.9}Sr_{0.1}MnO_3$ single crystal in the cooling regimes studied shows typical ''spin-glass'' behavior. © *1998 American Institute of Physics.*
[S0021-3640(98)00713-0]

PACS numbers: 75.60.Ch, 75.50.Lk, 75.30.Kz

In a number of works published in recent years the magnetic state of lanthanum manganites $La_{1-x}Sr_xMnO_3$ with low strontium concentrations $x \sim 0.1$ at low temperatures is classified as antiferromagnetic with a canted magnetic structure.[1,2] Alongside this point of view is a different one, viz., that a spin-glass state is realized in calcium and strontium manganites doped with rare-earth metals (praseodymium, neodymium, or terbium).[3,4] Finally, it is asserted in Ref. 5, contrary to Refs. 1 and 2, that lanthanum
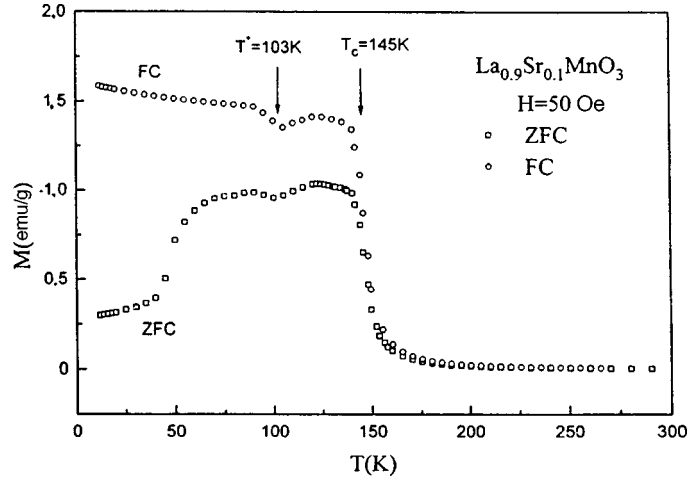
FIG. 1. Temperature dependences of the magnetization of a $La_{0.9}Sr_{0.1}MnO_3$ single crystal, measured in a field $H = 50$ Oe, in the FC and ZFC regimes.

manganite with a strontium content $x \sim 0.1$ is not an insulator with a canted antiferromagnetic structure but rather a polaron-ordered phase whose magnetic structure has not been established. In this connection it is of interest to investigate in greater detail the behavior of the magnetization of a single crystal of this compound, in contrast to most studies, which have been performed on ceramic (polycrystalline) samples.

To determine the possibility of a spin-glass state being realized in the $La_{1-x}Sr_xMnO_3$ system without doping with rare-earth metals, we investigated the temperature dependences of the magnetization $M(T)$ of a $La_{0.9}Sr_{0.1}MnO_3$ single crystal in two cooling regimes:

1) cooling in a zero magnetic field from temperatures above the magnetic ordering point down to 4.2 K (ZFC);

2) cooling in a high magnetic field $H = 55$ kOe (FC).

The single crystal was grown by the floating-zone method zone with radiation heating of the zone (xenon lamp). The Laue diffraction patterns and diffraction patterns obtained at $T = 293$ K showed the experimental sample to be an orthorhombic single crystal with crystallographic domain (parquet) structure. It had the form of a parallelepiped with transverse dimensions of the order of 1 mm and mass 38.0 mg. During the measurements, the magnetic field was directed to within $\pm 2°$ along a crystallographic axis of the $\langle 112 \rangle$ type.

The magnetization was measured on a Quantum Design SQUID magnetometer in the temperature interval 4.2–300 K and magnetic fields from 50 Oe up to 55 kOe. Before each measurement of the temperature dependences $M(T)$ and field dependences $M(H)$ of the magnetization, in both the ZFC and FC regimes, the sample was precooled to 4.2 K from a temperature not less than 300 K.

Figure 1 displays the temperature dependence of the magnetization of the experimental single crystal, measured in a weak magnetic field $H = 50$ Oe in the ZFC regime.[b]
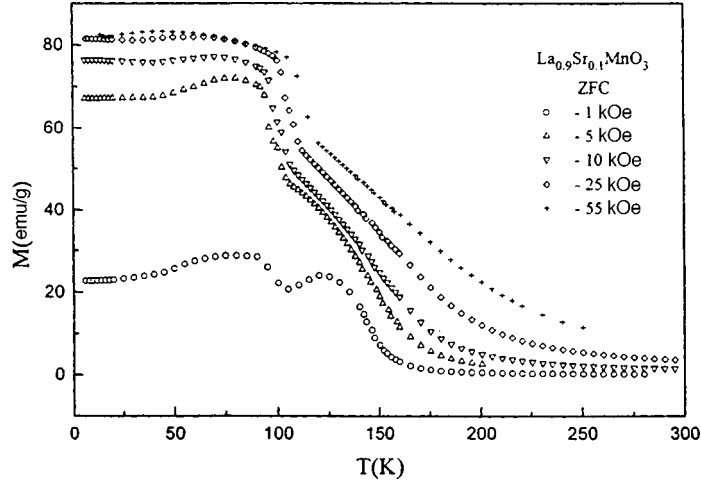
FIG. 2. Evolution of the curves $M(T)$ of a $La_{0.9}Sr_{0.1}MnO_3$ single crystal, measured in the ZFC regime, in magnetic fields from 1 to 55 kOe.

Two features stand out clearly: a minimum in $M(T)$ at $T^* = 103$ K and a sharp drop of the magnetization at $T_c = 145$ K. We note that such a ''double-hump'' temperature dependence of the ac magnetic susceptibility of a single crystal with the same composition, measured at 135 Hz with amplitude modulation of a 10 Oe magnetic field, was recently observed in Ref. 6. Measurements of $M(T)$ in the same ZFC regime but at higher fields 1–55 kOe (Fig. 2) show that a high magnetic field changes the temperature dependence $M(T)$ considerably, leaving only the anomaly near T^* sharply expressed.

The form of the curve $M(T)$ (Fig. 1, top curve) measured in a 50 Oe field in the FC regime (cooling at $H = 55$ kOe) also differs strongly from the temperature dependence $M(T)$ in the ZFC regime: Instead of the strong (factor of 4) increase in the magnetization as the temperature increases from 4.2 to 100 K, in the FC regime, at $H = 50$ Oe, the magnetization does not increase but decreases. The value of M at $T = 4.2$ K in the FC regime is six times greater than in the ZFC regime. In sufficiently high fields the form of the dependence $M(T)$ in both the ZFC and FC regimes (Fig. 3) is similar, i.e., only the anomaly near T^* remains pronounced. We note that at liquid-helium temperatures hysteresis is observed in $M(H)$ (Fig. 4).

Thus the experimental data presented attest to a complicated magnetic structure of the compound $La_{0.9}Sr_{0.1}MnO_3$ and a magnetic state that is very labile with respect to the magnetic field.

The sharp drop in magnetization at $T_c = 145$ K can be quite reliably attributed to a phase transition from the ferro- to the paramagnetic state and agrees with the results of Refs. 2, 6, and 7, whereas the anomaly observed clearly in $M(T)$ at $T^* = 103$ K in both the ZFC and FC regimes can hardly be unequivocally interpreted as a simple transition to an antiferromagnetic state with a canted magnetic structure at $T < T^*$, as is done in Refs. 1, 2, and 7. The results of our measurements show that the anomaly at $T^* = 103$ K can be interpreted differently: It can be supposed that for $T < T^*$ a cluster-glass state is realized in the compound $La_{0.9}Sr_{0.1}MnO_3$ in weak magnetic fields, since the magnetization of
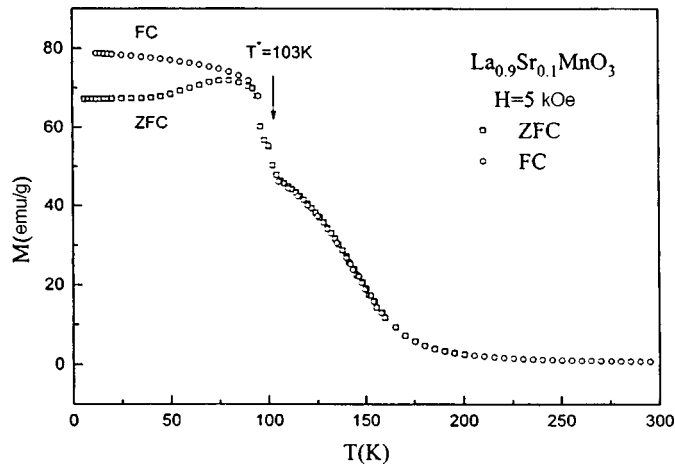
FIG. 3. Temperature dependences of the magnetization of the same single crystal, measured in a 5 kOe field, in the FC and ZFC regimes.

single-crystal $La_{0.9}Sr_{0.1}MnO_3$ in weak magnetic fields exhibits typical spin-glass behavior at temperatures $T < T^*$.

What is more, neutron diffraction studies[2] of the crystal structure show that at $T^* \cong 103$ K we are dealing not only with a magnetic transition but simultaneously with a structural transition also. As follows from this work, a transition occurs near T^* from an orthorhombic pseudocubic phase ($T < T^*$) to an orthorhombic phase with Jahn–Teller distortions ($T > T^*$).[2] Nonetheless, the experimental facts which we present do not rule out the possibility of coexistence of two magnetically ordered structures (for example, ferro- and antiferromagnetic) at $T < T^*$.

In conclusion, the main result of the present work is an experimental proof of the
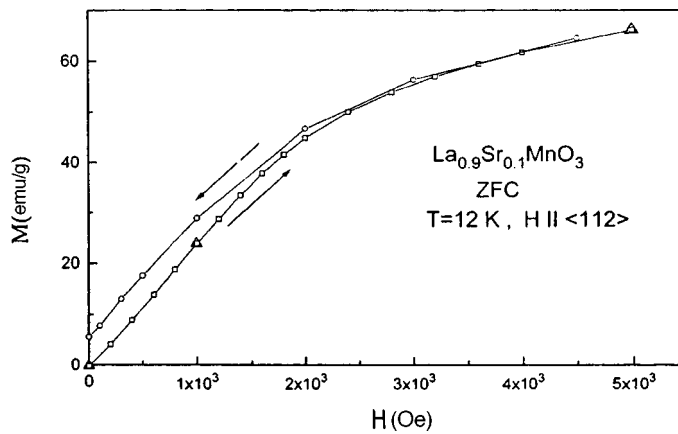

FIG. 4. Hysteresis of the magnetization of a $La_{0.9}Sr_{0.1}MnO_3$ single crystal cooled in the ZFC regime; $T = 12$ K. Δ — independent control measurements, showing the reproducibility of the results.

fact that the magnetic properties of the $La_{1-x}Sr_xMnO_3$ system with low strontium content depend not only the chemical composition of the compound but also, to a considerable degree, on the cooling regime of the sample, and that the magnetic state of a $La_{1-x}Sr_xMnO_3$ crystal is very sensitive to the magnetic field. It is very likely that the results of measurements of other properties of this system (specifically, the magnetostriction) will also differ, depending on whether the sample is cooled in the presence or absence of a magnetic field. To establish unequivocally the magnetic state of a $La_{1-x}Sr_xMnO_3$ single crystal below 100 K it is necessary to perform direct experiments with small-angle magnetic scattering of neutrons in the ZFC and FC cooling regimes.

After the measurements were performed and the manuscript of this letter was prepared for publication, Ref. 8 appeared in print, reporting the observation of spin-glass behavior of the magnetization in polycrystalline $Y_{0.7}Ca_{0.3}MnO_3$ without doping with rare-earth metals. It is entirely possible that a different behavior of magnetic properties in the ZFC and FC regimes is a characteristic feature of the magnetic state of lanthanum manganites[3,4] and manganates[9] in a definite range of strontium and calcium concentrations.

We are grateful to A. Korolev, N. Kourov, V. Nizhankovskiĭ, T. Palevskiĭ, V. Sazonova, V. Sussk, and Yu. Tsiovkin for helpful discussions and assistance.

[1] H. Kawano, R. Kajimoto, M. Kubota *et al.*, Phys. Rev. B **53**, 2202 (1996).
[2] H. Kawano, R. Kajimoto, M. Kubota *et al.*, Phys. Rev. B **53**, R14709 (1996).
[3] A. Maignan, U. V. Varadaraju, F. Millange *et al.*, J. Magn. Magn. Mater. **168**, L237 (1997).
[4] J. M. Teresa, M. R. Ibara, J. Garsia *et al.*, Phys. Rev. Lett. **76**, 3392 (1996).
[5] Y. Yamada, O. Hiro, S. Mohdo *et al.*, Phys. Rev. Lett. **77**, 904 (1996).
[6] S. E. Lofland, V. Ray, P. H. Kim *et al.*, J. Phys.: Condens. Matter **9**, L633 (1997).
[7] A. Urushibara, Y. Morimoto, T. Arima *et al.*, Phys. Rev. B **51**, 14103 (1995).
[8] X. L. Wang, J. Horvat, and H. K. Liu, J. Magn. Magn. Mater. **182**, L1 (1998).
[9] Y. Morimoto, Y. Tomioka, A. Asamitsu *et al.*, Phys. Rev. B **51**, 3297 (1995).

Translated by M. E. Alferieff

Nonequilibrium distribution of two-dimensional electrons in the presence of transverse high-frequency pumping

F. T. Vas'ko[a]

Institute of Semiconductor Physics, Ukrainian National Academy of Sciences, 252650 Kiev, Ukraine

A mechanism is described which leads to the formation of a nonequilibrium distribution of two-dimensional electrons on account of the effect of the electric field of radiation on the interaction of the electrons with a phonon thermostat in the absence of absorption. An analysis is made of the case of a nonresonant, transversely polarized pump, where the intersubband transitions and Drude absorption of the radiation are very weak but the probabilities of transitions involving the participation of phonons do not satisfy the principle of detailed balance. The character of the nonequilibrium distribution of highly degenerate electrons is discussed and their effective temperature is found. © *1998 American Institute of Physics.* [S0021-3640(98)00813-5]

An external electric field applied to an electron gas not only leads to absorption of energy on account of the current in phase with this field, but it also changes the transition probabilities describing the interaction of electrons with a thermostat. This fact was already noted in early works on the quantum theory of electron transport in strong high-frequency[1] or static[2] fields and was discussed in detail in subsequent works (see Ref. 3). A result of such a change in the transition probabilities is that the principle of detailed balance for transitions between the states with energies ε and ε_1 (T is the temperature of the phonon thermostat)

$$w(\varepsilon,\varepsilon_1)=w(\varepsilon_1,\varepsilon)\exp[(\varepsilon_1-\varepsilon)/T] \tag{1}$$

is violated. If Eq. (1) does not hold, then the equilibrium Fermi distribution will not be imposed on the electrons in their interaction with the phonon thermostat, even in the absence of radiation absorption due to the presence of a current. Such a mechanism of formation of a nonequilibrium distribution is inefficient compared with the ordinary heating in the case of a static field, since the characteristic collision time $\hbar/\bar{\varepsilon}$ ($\bar{\varepsilon}$ is the average energy of the electrons; the field changes the transition probability in such a time interval) is short compared with the transit time $\bar{\tau}$ under the standard condition $\bar{\varepsilon} \gg \hbar/\bar{\tau}$. For the quantum frequency range $\hbar\omega > \bar{\varepsilon}$ the nondissipative mechanism under study makes an appreciable contribution to the formation of a nonequilibrium electron

distribution,[4,5] but it has turned out to be quite difficult to distinguish such contributions experimentally for 3D electrons against the background of Drude absorption, and this has not yet been done with pumping by a CO_2 laser.

The situation changes qualitatively in the case of nonresonance terahertz pumping of 2D systems (such experiments were recently begun using free-electron-laser radiation[6]). The problem is that there will be no absorption of terahertz radiation under conditions of excitation by a nonresonance transverse electric field (since the current across the QW is due to intersubband transitions only), but this field will effectively influence the electron–phonon interaction on account of a change in the mechanism by which the transverse wave vector of 3D phonons is transferred in the scattering of 2D electrons on them. For this reason, the transition probabilities will be different from the standard expressions in the absence of pumping,[7] and the principle of detailed balance (1) is violated. The objective of the present letter is to describe such a mechanism of nondissipative deviation from thermodynamic equilibrium for 2D electrons in an external field of terahertz radiation and to discuss the possibilities of observing it.

The electron distribution function $f_{\mathbf{p}t}$ over the canonical 2D momenta in a high-frequency electric field $\mathbf{E}\cos\omega t$ is determined from the kinetic equation

$$\partial f_{\mathbf{p}t}/\partial t = J(f|\mathbf{p}t), \quad f_{\mathbf{p}t+2\pi/\omega} = f_{\mathbf{p}t}, \tag{2}$$

where a periodicity condition ($2\pi/\omega$ is the period of the oscillations of the distribution) is used instead of an initial condition. The collision integral $J(f|\mathbf{p}t)$ for the case of scattering with emission of acoustic phonons has the form

$$J^{(e)}_{e-ph}(f|\mathbf{p}t) = \frac{1}{\hbar^2}\int_{-\infty}^{\infty}\frac{dq_\perp}{2\pi}\int\frac{d\mathbf{p}_1}{(2\pi\hbar)^2}|C_Q|^2(N_Q+1)$$

$$\times\int_{-\infty}^{t}dt'\,e^{\lambda t'}\{e^{-i\omega_Q(t-t')}(0|e^{-iq_\perp z}|0)[S_{\mathbf{p},0}(t,t')S_{\mathbf{p}_1,-q_\perp}(t,t')^*$$

$$\times(1-f_{\mathbf{p}t'})f_{\mathbf{p}_1 t'} - S_{\mathbf{p}_1,q_\perp}(t,t')S_{\mathbf{p},0}(t,t')^*(1-f_{\mathbf{p}_1 t'})f_{\mathbf{p}t'}] + \text{c.c.}\}. \tag{3}$$

Here $\omega_Q = sQ$ is the dispersion law of acoustic phonons with sound velocity s and wave vector $\mathbf{Q} = (\mathbf{p}-\mathbf{p}_1)/\hbar\times\mathbf{q}_\perp$, N_Q is the Planck distribution, C_Q is the volume matrix element of the electron–phonon interaction, the form factor $(0|e^{-iq_\perp z}|0)$ is calculated with respect to the wave functions of the ground state $|0\rangle$, and $\lambda\to+0$. The dynamics of a 2D electron in a collision process is described by the factor

$$S_{\mathbf{p},q_\perp}(t,t') = (\mathbf{p}0|e^{iq_\perp z}\hat{S}(t,t')|0\mathbf{p}), \tag{4}$$

where S — the operator $\hat{S}(t,t')$ — satisfies the Schrödinger equation with the initial condition $\hat{S}(t,t')=1$. If the intersubband energy exceeds $\hbar\omega$ and the average energy of the 2D electrons, we write the equation of motion for (4) taking into account only the ground state $|0\rangle$ with energy ε_0:

$$
i\hbar \frac{\partial S_{\mathbf{p},q_\perp}(t,t')}{\partial t} = \left[\varepsilon\left(\mathbf{p} + \frac{e}{\omega}\mathbf{E}_\parallel \sin \omega t \right) + \varepsilon_0 - \frac{eE_\perp \hbar q_\perp}{m\omega} \sin \omega t \right.
$$
$$
\left. + \frac{(eE_\perp)^2}{2m\omega^2} \sin^2 \omega t \right] S_{\mathbf{p},q_\perp}(t,t'). \tag{5}
$$

Here $\varepsilon(\mathbf{p}) = p^2/2m$ is the kinetic energy of longitudinal motion with effective mass m, while the initial condition has the form $S_{\mathbf{p},q_\perp}(t,t) = (0|\exp(iq_\perp z)|0)$. Solving Eq. (5), we transform the products of the factors (4) appearing in the collision integral (3) to the form

$$
S_{\mathbf{p},0}(t,t') S_{\mathbf{p}_1,-q_\perp}(t,t')^* = \exp\left[\frac{i}{\hbar}(\varepsilon_p - \varepsilon_{p_1})(t-t') + i(\mathbf{v}_\omega \cdot \mathbf{Q}) \int_t^{t'} dt_1 \sin \omega t_1 \right] (0|e^{iq_\perp z}|0) \tag{6}
$$

with characteristic velocity $\mathbf{v}_\omega = e\mathbf{E}/(m\omega)$, determining the amplitude of the electron oscillations in the field of the wave. Using the periodicity of $f_{\mathbf{p}t}$ and expanding the product (6) in a series in Bessel functions it is possible to calculate the time integrals in $J_{e-ph}^{(e)}(f|\mathbf{p}t)$. The contribution to the collision integral from processes involving phonon absorption is obtained from Eq. (3) after making the substitutions $(N_Q+1) \rightarrow N_Q$, $\omega_Q \rightarrow -\omega_Q$, and $\mathbf{Q} \rightarrow -\mathbf{Q}$.

When the inequality $\omega\bar{\tau} \gg 1$ holds ($\bar{\tau}$ is the characteristic relaxation time, an estimate of the collision integral), $f_{\mathbf{p}t}$ can be written as $\bar{f}_\mathbf{p} + \delta f_{\mathbf{p}t}$, where the period-averaged distribution $\bar{f}_\mathbf{p}$ is found from the equation

$$
\frac{\omega}{2\pi} \int_{-\pi/\omega}^{\pi/\omega} dt\, J(\bar{f}|\mathbf{p}t) = 0, \tag{7}
$$

and the oscillating correction $\delta f_{\mathbf{p}t}$ is small. Carrying out here the integration over t and t', we write the equation for $\bar{f}_\mathbf{p}$ as the balance of the incoming and outgoing contributions:

$$
\int \frac{d\mathbf{p}_1}{(2\pi\hbar)^2} [W(\mathbf{p},\mathbf{p}_1)(1-\bar{f}_\mathbf{p})\bar{f}_{\mathbf{p}_1} - W(\mathbf{p}_1,\mathbf{p})(1-\bar{f}_{\mathbf{p}_1})\bar{f}_\mathbf{p}] = 0. \tag{8}
$$

The probabilities of transitions between the states of 2D electrons with momenta $\mathbf{p}$ and $\mathbf{p}_1$ have the form

$$
W(\mathbf{p},\mathbf{p}_1) = \frac{2\pi}{\hbar} \int_{-\infty}^{\infty} \frac{dq_\perp}{2\pi} |C_Q|^2 (N_Q+1) \chi(q_\perp d) \Delta(\varepsilon_p - \varepsilon_{p_1} + \hbar\omega_Q)
$$
$$
+ [(N_Q+1) \rightarrow N_Q, \omega_Q \rightarrow -\omega_Q, \mathbf{Q} \rightarrow -\mathbf{Q}]. \tag{9}
$$

Here the form factor $\chi(q_\perp d) = |(0|e^{iq_\perp z}|0)|^2$ appears (d is the width of the QW; see Ref. 7 for the explicit form of $\chi(x)$), and instead of the law of conservation of energy with a delta function there arises the sum

$$
\Delta(E) = \sum_{l=-\infty}^{\infty} J_l[(\mathbf{v}_\omega \cdot \mathbf{Q})/\omega]^2 \delta(E + l\hbar\omega), \tag{10}
$$

describing the contribution of multiphoton transitions;[1,4] $J_l(x)$ is a Bessel function. We note that even for transverse pumping, in which case there is no absorption of radiation, the contribution of multiphoton transitions in Eq. (10) will be substantial for $\mathbf{v}_\omega/d\omega \sim 1$ (d is the width of the QW; here the transverse-wave-vector transfer is estimated as d^{-1}). The condition (1) for the probabilities $W(\mathbf{p},\mathbf{p}_1)$ breaks down, and the solution of Eq. (8) will be the nonequilibrium solution.

Equation (8) is studied below for highly degenerate 2D electrons in the quasielastic scattering approximation

$$sp_F, s\hbar/d \ll T, T_e. \tag{11}$$

Here p_F is the Fermi momentum, so that the left-hand side of Eq. (11) estimates the energy transferred by acoustic phonons propagating along and across the QW;[8] T_e is the characteristic temperature of the electrons. The zero-photon contribution (transformed in the standard manner[9]) is of the order of $(\hbar\omega_Q/T_e)^2$ for the spherically symmetric part of the distribution f_ε (the contributions to $\overline{f}_\mathbf{p}$ which are asymmetric in the $\mathbf{p}$ plane are small, just as for the standard theory of hot electrons), and the contribution of multiphoton processes can be described in the elastic approximation. The result is the differential–difference equation

$$\frac{d}{d\varepsilon} E_\varepsilon \left[T\frac{df_\varepsilon}{d\varepsilon} + f_\varepsilon(1-f_\varepsilon) \right] + \sum_{l=-\infty}^{\infty} \alpha_l(\varepsilon)(f_{\varepsilon+l\hbar\omega} - f_\varepsilon) = 0, \tag{12}$$

where the characteristic energy E_ε and the dimensionless coefficients $\alpha_l(\varepsilon)$ are given for the deformational electron–phonon interaction by the integrals

$$E_\varepsilon = d\int_{-\infty}^{\infty} dq_\perp \chi(q_\perp d) \int_0^{2\pi} \frac{d\varphi}{2\pi} J_0[(\mathbf{v}_\omega \cdot \mathbf{Q}_0)/\omega]^2 \frac{(\hbar\omega_Q)^2}{2T}, \tag{13}$$

$$\alpha_l(\varepsilon) = \theta(\varepsilon+l\hbar\omega) d\int_{-\infty}^{\infty} dq_\perp \chi(q_\perp d) \int_0^{2\pi} \frac{d\varphi}{2\pi} J_l[(\mathbf{v}_\omega \cdot \mathbf{Q}_l)/\omega]^2,$$

where $\varphi = \widehat{\mathbf{p},\mathbf{p}_1}$, and the longitudinal wave-vector transfers in the arguments of the delta functions take into account the conservation of energy in multiphoton transitions:

$$\frac{(\mathbf{v}_\omega \cdot \mathbf{Q}_l)}{\omega} = \frac{\mathbf{v}_\omega^\parallel}{\hbar\omega}\left[\sqrt{2m\varepsilon}\cos\varphi - \sqrt{2m(\varepsilon+l\hbar\omega)} \right] + \frac{\mathbf{v}_\omega^\perp}{\hbar\omega}. \tag{14}$$

For the 2D case $p_F \ll \hbar/d$, and the contribution of the longitudinal field component, which described by $\mathbf{v}_\omega^\parallel$ and determines the Drude absorption, is small, so that the non-equilibrium distribution is formed solely by the field component perpendicular to the 2D layer, which is not absorbed in the absence of intersubband transitions. Confining our attention to this case, we shall not discuss the polarization dependence of the response arising in heavily doped QWs or when $\mathbf{v}_\omega^\parallel \gg \mathbf{v}_\omega^\perp$ (for almost normal propagation of the radiation; the case of pumping with $\mathbf{v}_\omega^\perp = 0$ was studied in Refs. 6, 10, and 11). Since the zero-photon contribution in Eq. (12) is small by the parameter $(\hbar\omega_Q/T_e)^2$, strong electron redistribution occurs even for $\mathbf{v}_\omega^\perp/d\omega \ll 1$, when only single-photon transitions need be taken into account. This case is described by the equation

$$\frac{d}{d\varepsilon}\left[T\frac{df_\varepsilon}{d\varepsilon}+f_\varepsilon(1-f_\varepsilon)\right]+\eta[f_{\varepsilon+\hbar\omega}+\theta(\varepsilon-\hbar\omega)f_{\varepsilon-\hbar\omega}-2f_\varepsilon]=0,\tag{15}$$

where the characteristic inverse energy $\eta=T(\mathbf{v}_\omega^\perp/s\hbar\omega)^2/2$ arises. Equation (12) or (15) must be solved with the normalization condition $\int_0^\infty d\varepsilon f_\varepsilon=\varepsilon_F$, where ε_F is the Fermi energy for zero temperature.

The simplest solution of Eq. (15) is obtained for classical frequencies $\omega<T_{\mathrm{eff}}/\hbar(T_{\mathrm{eff}}$ is the effective temperature; see below), for which the difference operator on the right-hand side can be replaced by $\eta(\hbar\omega)^2 d^2 f_\varepsilon/d\varepsilon^2$. For the energy range $\varepsilon\gg\hbar\omega$ we obtain a Fermi distribution with temperature

$$T_{\mathrm{eff}}=T\left[1+\frac{1}{2}\left(\frac{\mathbf{v}_\omega^\perp}{s}\right)^2\right].\tag{16}$$

For the quantum frequency range $\hbar\omega>T_{\mathrm{eff}}$ the solution of Eq. (15) can be written down by iterations on the difference operator, which is proportional to η, and the distribution f_ε has kinks at energies $\varepsilon_F\pm\hbar\omega$, $\varepsilon_F\pm 2\hbar\omega$, ... Such anomalies in the distribution have been discussed for the 3D case,[5] and they can be appear at low carrier densities, for which electron–electron collisions are negligible.

In heavily doped QWs electron–electron collisions impose a Fermi distribution $\tilde{f}_\varepsilon$ with an effective temperature T_e that is determined from the balance equation:

$$(T_e-T)\tilde{f}_{\varepsilon=0}=\eta\int_0^\infty d\varepsilon\,\varepsilon[\tilde{f}_{\varepsilon+\hbar\omega}+\theta(\varepsilon-\hbar\omega)\tilde{f}_{\varepsilon-\hbar\omega}-2\tilde{f}_\varepsilon]$$

$$=\eta\left[\hbar\omega\int_0^{\hbar\omega}d\varepsilon\tilde{f}_\varepsilon-\int_0^{\hbar\omega}d\varepsilon\,\varepsilon\tilde{f}_\varepsilon\right],\tag{17}$$

which describes energy redistribution between the 2D electrons and the thermostat (and not the balance of energy transfer from the field to the thermostat via the 2D electrons, as in the case of ordinary heating). Since here the contribution of scattering by optical phonons is neglected, T_e is less than the typical Fermi energies, and the right-hand side of Eq. (17) can be calculated in the zero-temperature approximation everywhere except in a narrow interval where $|\hbar\omega-\varepsilon_F|<T_e$. The result is a correction to the electron temperature

$$T_e-T=T\left(\frac{\mathbf{v}_\omega^\perp}{2s}\right)^2\begin{cases}1,&\hbar\omega<\varepsilon_F\\(\varepsilon_F/\hbar\omega)[2-(\varepsilon_F/\hbar\omega)],&\hbar\omega>\varepsilon_F\end{cases}.\tag{18}$$

Since the expressions for $\hbar\omega<\varepsilon_F$ and $\hbar\omega>\varepsilon_F$ match up, we shall not solve Eq. (17) in the transitional region. We note that Eq. (18) for small $\hbar\omega$ differs from Eq. (16) by a factor of 1/2 on account of the contribution of $\theta(\varepsilon-\hbar\omega)$ in Eq. (17), while the expansion of the difference operator in Eq. (15) is applicable only for high energies. The increase in electron temperature is determined here and in Eq. (16) by the dimensionless parameter $(\mathbf{v}_\omega^\perp/s)^2$; for GaAs-based QWs this parameter is close to 1 with 100 μm pump intensity 2.9 kW/cm^2 (as the frequency decreases, this characteristic intensity decreases as ω^2).

The character of the nonequilibrium distribution is determined, just as for ordinary heating with absorption of energy, by the competition between the important scattering

mechanisms, so that a complete description requires taking into account the scattering on *LO* phonons (for a longitudinal terahertz pumping such scattering is substantial for intensities exceeding 10 kW/cm^2).[10,11] In the present letter it is not so much that the electron distribution is described quantitatively (which requires solving Eq. (8) numerically with all of the important types of scattering taken into account), as a qualitatively new mechanism is considered for the formation of a nonequilibrium distribution under nonresonant transverse terahertz pumping, for which there is no heating of electrons on account of absorption of radiation, but energy redistribution occurs between the 2D electrons and the phonon thermostat. Transverse terahertz pumping of wide QWs leads to an optical Stark effect on intersubband transitions.[12] The results presented demonstrate the appearance of a highly nonequilibrium electron distribution in narrow QWs (which can be observed in the photoconductivity or interband photoluminescence[6,10]), which is associated not with a change in intersubband transitions in the field of the wave but rather with the breakdown of the principle of detailed balance in the interactions of electrons in the lowest subband with the phonon thermostat.

[a])e-mail: zinovi@lab2.kiev.ua

[1] V. I. Mel'nikov, JETP Lett. **9**, 120 (1969).

[2] J. R. Barker, J. Phys. C **6**, 2663 (1973).

[3] H. Haug and A.-P. Jauho, *Quantum Kinetics in Transport and Optics of Semiconductors,* Springer, Berlin, 1997.

[4] F. T. Vas'ko, Fiz. Tverd. Tela (Leningrad) **27**, 2647 (1985) [Sov. Phys. Solid State **27**, 1587 (1985)].

[5] F. T. Vas'ko, Fiz. Tverd. Tela (Leningrad) **17**, 2288 (1975) [Sov. Phys. Solid State **17**, 1514 (1975)]; Fiz. Tverd. Tela (Leningrad) **16**, 532 (1974) [Sov. Phys. Solid State **16**, 337 (1974)].

[6] J. Cerne, A. G. Markelz, M. S. Sherwin *et al.*, Phys. Rev. B **51**, 5253 (1995).

[7] P. Price, Ann. Phys. **133**, 217 (1981).

[8] S. M. Badalyan and I. B. Levinson, Fiz. Tverd. Tela (Leningrad) **30**, 2764 (1988) [Sov. Phys. Solid State **30**, 1592 (1988)]; V. Karpus, Fiz. Tekh. Poluprovodn. **20**, 12 (1986) [Sov. Phys. Semicond. **20**, 6 (1986)].

[9] F. G. Bass and Yu. G. Gurevich, *Hot Electrons and Strong Electromagnetic Waves in the Plasma of Semiconductors and Gas Discharges* [in Russian], Nauka, Moscow, 1975

[10] N. G. Asmar, A. G. Markelz, E. G. Gwinn *et al.*, Phys. Rev. B **51**, 18041 (1995).

[11] W. Xu and C. Zhang, Phys. Rev. B **55**, 5259 (1997).

[12] K. Craig, C. L. Felix, J. N. Heymann *et al.*, Semicond. Sci. Technol. **9**, 627 (1994); B. Birnir, B. Galdrikian, R. Cramer, and M. S. Sherwin, Phys. Rev. B **47**, 6795 (1993).

Translated by M. E. Alferieff

Anisotropy of optical phonons in semiconductor superlattices: Raman scattering experiments

D. A. Ténné,[a] V. A. Gaĭsler, N. T. Moshegov, and A. I. Toropov

Institute of Semiconductor Physics, Siberian Branch of the Russian Academy, of Sciences, 630090 Novosibirsk, Russia

A. P. Shebanin

Joint Institute of Geology, Geophysics, and Mineralogy, Siberian Branch of the Russian Academy of Sciences, 630090 Novosibirsk, Russia

Experiments on Raman scattering in the ''forward'' geometry, permitting observation of anisotropy of the optical phonons, are performed on specially prepared short-period GaAs/AlAs superlattice structures with the substrates removed and the surfaces covered with an antireflective layer. The experimental data agree well with the computational results obtained for the angular dispersion of optical phonons in superlattices on the basis of a modified continuum model. © *1998 American Institute of Physics.* [S0021-3640(98)00913-X]

PACS numbers: 78.66.Fd, 78.30.Fs

The phonon spectrum of semiconductor superlattices (SLs) has been a subject of intense experimental and theoretical investigation for the last few years.[1] It has been established[1,2] that optical phonons propagating along an axis of a SL (the angle Θ between the phonon wave vector q and the direction of growth of the SL equals 0) are localized within a single layer of the SL. As has been shown in a number of theoretical papers,[3–6] when the phonon wave vector tilts away from the axis of the SL, localized optical phonons show strong angular dispersion. The frequencies of the odd-order localized modes depend strongly on the angle Θ, even at the center of the Brillouin zone, i.e., when the absolute value of q approaches zero. This so-called anisotropy of optical-phonon frequencies is due to the macroscopic electric field produced by optical phonons. The dipole moment produced by even-order localized modes equals zero on account of the symmetry of the modes, and for this reason they do not show angular dispersion for small q.[5,6]

One of the main methods of experimental investigation of the phonon properties of SLs is Raman scattering (RS) spectroscopy.[1] Many papers on RS by optical phonons localized in GaAs[1,2] and AlAs[7] layers have now been published. However, in most studies the experiments are performed in the conventional geometry of backscattering from a (001) surface. As a result of the large index of refraction of semiconductors, such a geometry makes it possible to observe in the spectra only phonons whose wave vector is close to the normal to the SL. Raman scattering experiments investigating phonons

which propagate along the layers of the SL are still rare. They include investigations by the method of RS microspectroscopy with excitation in the plane of the SL layers.[8–10]

The optimal variant for investigating the anisotropy of optical phonons in SLs is the study of RS in the forward geometry, where the exciting radiation is directed along the axis of the SL while the scattered radiation makes a small angle with this axis. Such an experimental geometry makes it possible to analyze the frequencies of phonons with small vectors and to obtain information about their angular dispersion. The fundamental difficulties in performing such experiments are due to the need to remove the thick (400–500 μm) opaque GaAs substrate without damaging the thin (0.1–0.5 μm) SL layer as well as the need to eliminate the reflection of light from the SL–vacuum boundary, which results in the appearance of backscattering.

In the present work we investigated samples of short-period SLs $(GaAs)_m(AlAs)_m$, where $m=5$ and 7 monolayers, grown on (001) GaAs substrates by molecular-beam epitaxy, at the Institute of Semiconductor Physics of the Siberian Branch of the Russian Academy of Sciences, and specially prepared for performing the experiment. The GaAs substrates were removed by highly selective etching, and a quarter-wave antireflective ZrO_2 layer, which efficiently suppressed reflection of both the exciting and scattered light, was deposited on the SL surface. Light scattering was studied at $T=80$ K and was excited in the transmission region of these SLs by 647.1 nm Kr^+-laser light. The RS spectra were recorded on a Jobin Yvon U1000 spectrometer.

Figure 1 shows the RS spectra in the range of GaAs optical phonons of a sample SL $(GaAs)_7(AlAs)_7$: a) in the geometry of backscattering from the (001) surface under normal incidence ($\Theta=0$); b) incidence at the Brewster angle ($\sim 75°$) with respect to the surface of the sample (the angle Θ inside the SL is 16°); and, c) under conditions of forward scattering ($\Theta=90°$). The backscattering spectra are typical for SLs grown in the (001) direction. They contain lines of odd-order localized LO phonons in the $z(x,y)\bar{z}$ geometry, while even-order localized phonons (LO_2) dominate in the parallel polarization configuration $z(x,x)\bar{z}$. However, when the phonon wave vector deviates from the normal direction (spectrum b), a shift of the LO_1-phonon line in the low-frequency direction is noticed, while the LO_2-phonon frequency remains unchanged. The LO_1 line is absent in the forward scattering spectra, and the LO_2 line is strongest and has the highest frequency in both polarization configurations. Similar behavior was also observed in the RS spectra of the sample SL $(GaAs)_5(AlAs)_5$.

The experimental results obtained can be explained on the basis of a calculation of the angular dispersion of GaAs optical phonons, which we performed using a modified continuum model.[6] The computational results for the SL $(GaAs)_7(AlAs)_7$ are presented in Fig. 2. In the calculation, the effective thickness of the localization layer (GaAs) was assumed to be 8 monolayers in order to take account of the nonzero displacements of the As atoms at the boundaries. The continuum model of Ref. 6 gives results which are in good agreement with a microscopic calculation in Ref. 9. We performed the calculation for the absolute value of the phonon wave vector $q=6.6\times 10^5$ cm^{-1}, corresponding to backscattering, and $q=1.4\times 10^4$ cm^{-1} (forward scattering at an angle of $\sim 2.5°$). The computational results for the angular dispersion for these values of q are virtually identical. A dependence on the absolute magnitude of the wave vector first appears for much larger values of q (of the order of 10^7 cm^{-1}).[6] For this reason, when comparing the
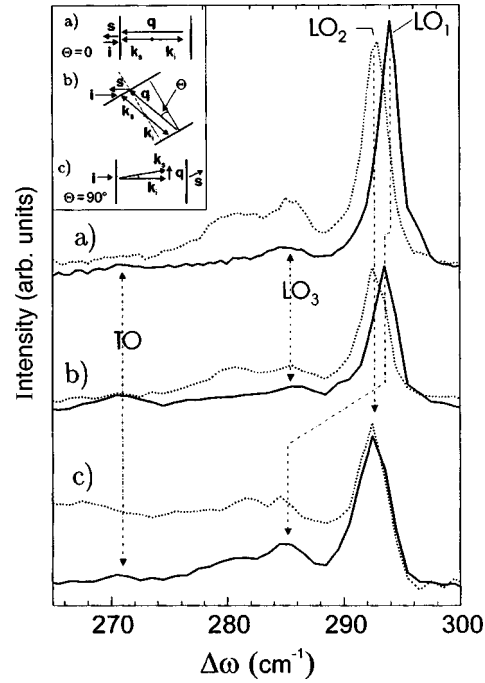
FIG. 1. Raman scattering spectra of the SL $(GaAs)_7(AlAs)_7$ in three different geometries, shown schematically in the inset. The solid and dotted lines correspond to perpendicular (x,y) and parallel (x,x) polarization configurations.
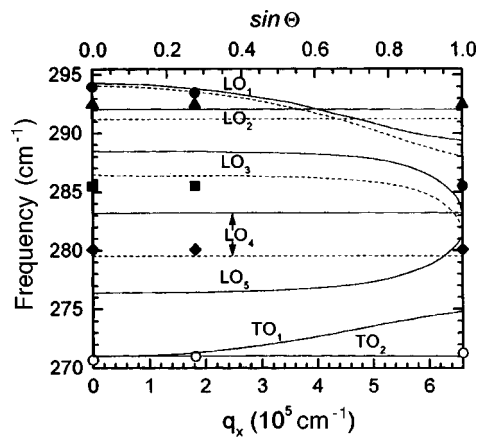

FIG. 2. Angular dispersion of optical phonons in the GaAs region for the SLs $(GaAs)_7(AlAs)_7$ (solid line) and $(GaAs)_6(AlAs)_7$ (dotted line; the first four LO modes are shown). The calculation was performed with a fixed value of the modulus of the phonon wave vector $q = 6.6 \times 10^5$ cm^{-1}. Symbols — Raman scattering data.

experimental data on backward and forward scattering, the difference in the absolute magnitude of the phonon wave vector can be neglected.

As one can see from Fig. 2, as the angle Θ increases, the LO_1-phonon frequency decreases and crosses the zero-dispersion line LO_2, and as it approaches the line of the LO_3 phonon, which possesses the same symmetry relative to the central plane of the GaAs layer, mode mixing (anticrossing) appears. It should be noted that the designations of the vibrational modes according to polarization and order (LO_1, LO_2, and so on) make sense only for $\Theta = 0$, but we use them to identify the lines. At $\Theta = 90°$ a LO_1 phonon evolves into a vibration with a frequency close to the LO_3 frequency at $\Theta = 0$. This explains the fact that peaks at such a frequency are observed in both the backward and forward scattering spectra. The experimental values of the phonon frequencies in the SL $(GaAs)_7(AlAs)_7$ are indicated in Fig. 2 by symbols. As one can see from the figure, the LO_1- and LO_2- phonon frequencies agree well with the computational results. The deviation of the frequencies of higher-order phonons from the computed values is probably due to the nonideality of the heterointerfaces. The roughness of the interfaces results in a decrease of the thickness of the phonon localization layer and, correspondingly, a decrease in the phonon frequency,[11,12] the shift being greater for higher-order phonons. For comparison, the angular dispersion of the first four GaAs LO modes, which is calculated for the smallest thickness (one monolayer) of the localization layer, is also presented in Fig. 2.

It should be noted that the above-described angular dispersion of optical phonons was observed only with excitation of RS in the transmission region of the SL. For the SLs $(GaAs)_9(AlAs)_9$ and $(GaAs)_9(AlAs)_5$ investigated in the present work, which have thicker GaAs layers, the RS excitation conditions ($\lambda = 647.1$ nm, $T = 80$ K) are resonance conditions. In this case the spectra in both the forward and backward scattering geometries in both polarization configurations (Fig. 3b) contain the same GaAs LO_2-phonon lines and the lines IF_1 and IF_2 in the GaAs and AlAs regions, respectively. The absence of large differences in the resonance RS spectra accompanying a change in the scattering geometry is explained by the fact that under resonance excitation conditions the wave vector conservation law in its simplest form ($\mathbf{k}_s = \mathbf{k}_i \pm \mathbf{q}$, where $\mathbf{k}_i$ and $\mathbf{k}_s$ are the wave vectors of the incident and scattered light) is not satisfied. As has been shown in a number of works,[13,14] the process of resonance RS by phonons in quantum wells is governed by a higher-order scattering mechanism, which includes elastic scattering of electrons (holes) by defects (nonideality of the heterointerfaces, impurities) in addition to the electron–phonon interaction. For this reason, the phonon wave vector in the RS process can possess a component q_x parallel to the SL layers, in both forward and backward scattering geometries.

The lines in the RS resonance spectra of superlattices below the LO_2-phonon frequency were compared earlier with even-order localized higher-order LO phonons (LO_4, LO_6).[2] However, a new interpretation of these lines[15] as wide features of so-called interface phonons (IF) was recently formulated. Interface phonons are simply vibrations obtained as a result of the evolution of localized LO_1 and TO_1 phonons as the wave vector deviates from the normal to the SL layers, i.e., the appearance of a nonzero component q_x.[5,9,10] Since phonons with different components q_x can participate in resonance RS with participation of defects, a wide feature appears in the spectra between the LO_1- and TO_1-phonon frequencies. Near GaAs frequencies this feature has minima at
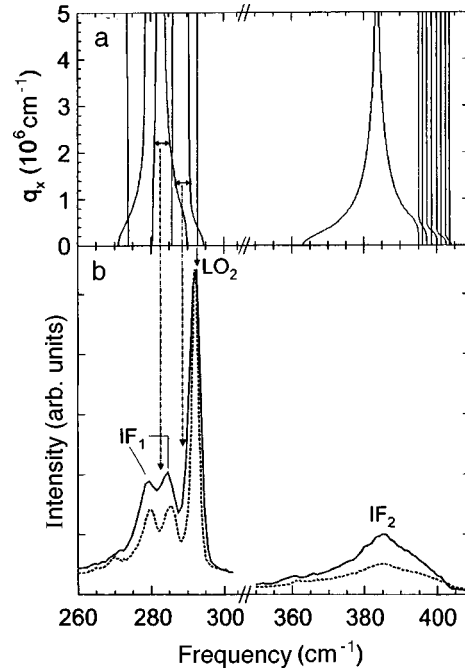
FIG. 3. a) Dependence of the frequencies of optical phonons in the SL $(GaAs)_9(AlAs)_9$ on the wave vector component q_x in the plane of the layers, as calculated in a modified continuum model[6] with a fixed value of the component in a direction along the SL axis ($q_z = 6.6 \times 10^5$ cm^{-1}). b) Resonance Raman scattering spectra in the SL $(GaAs)_9(AlAs)_9$ in the forward scattering geometry $z(x,x)z$ (solid line) and backscattering geometry $z(x,x)\bar{z}$ (dotted line). The spectra are normalized to the intensity of the LO_2 peak.

the locations of anticrossings with the dispersion lines of vibrations with the same symmetry (odd-order LO modes, see Fig. 3a). Interface phonons are not observed near the AlAs minima in the wide line because the AlAs LO phonons exhibit very weak dispersion in the (001) direction.[7,11] All anticrossings (Fig. 3a) fall in a narrow spectral region (395–403 cm^{-1}), and the corresponding minima are not resolved in the experiment.

We observed that in the case of forward scattering the ratio of the intensity of the IF lines to the intensity of the LO_2-phonon line is higher (by a factor of 1.6–1.9) than in the backscattering spectra (Fig. 3b). This can be explained by the fact that lines due to interface phonons having a nonzero component q_x are present in the backscattering spectra on account of the above-mentioned higher-order scattering mechanism with participation of defects. This mechanism also occurs in the case of forward scattering, but phonons with wave vector parallel to the SL layers also participate in a simple scattering process. For this reason, an additional increase in the intensity of the IF lines in the spectra occurs.

In summary, the investigation of Raman scattering in GaAs/AlAs superlattices in different geometries (forward scattering, backward scattering in a direction normal to the surface and at an angle to the normal) made it possible to observe anisotropy of the frequencies of optical phonons in SLs. The experimental results are described well by the angular dispersion of the optical phonons calculated in the continuum model. Comparing

the spectra of resonance RS in the forward and backward directions confirms the new interpretation of the lines in the region of GaAs optical vibrations as features due to interface phonons.

[a]e-mail: tenne@thermo.isp.nsc.ru

[1] B. Jusserand and M. Cardona in *Light Scattering in Solids V*, edited by M. Cardona and G. Güntherodt, Springer, Heidelberg, 1989, p. 49.
[2] A. K. Sood, J. Menendez, M. Cardona, and K. Ploog, Phys. Rev. Lett. **54**, 2111 (1985).
[3] E. Richter and D. Strauch, Solid State Commun. **64**, 867 (1987).
[4] S. F. Ren, H. Y. Chu, and Y.-C. Chang, Phys. Rev. B **40**, 3060 (1989).
[5] H. Rücker, E. Molinari, and P. Lugli, Phys. Rev. B **45**, 6747 (1992).
[6] M. P. Chamberlain, M. Cardona, and B. K. Ridley, Phys. Rev. B **48**, 14356 (1992).
[7] V. A. Gaĭsler, D. A. Ténné, N. T. Moshegov *et al.*, JETP Lett. **61**, 376 (1995).
[8] R. Hessmer, A. Huber, T. Egeler *et al.*, Phys. Rev. B **46**, 4071 (1992).
[9] G. Scamarcio, M. Haines, G. Abstreiter *et al.*, Phys. Rev. B **47**, 1483 (1993).
[10] A. Fainstein, P. Etchegoin, M. P. Chamberlain *et al.*, Phys. Rev. B **51**, 14448 (1995).
[11] E. Molinari, S. Baroni, P. Giannozzi, and S. de Gironcoli, Phys. Rev. B **45**, 4280 (1992).
[12] V. A. Gaĭsler, D. A. Ténné, N. T. Moshegov *et al.*, Fiz. Tverd. Tela (St. Petersburg) **38**, 2242 (1996) [Phys. Solid State **38**, 1235 (1996)].
[13] A. J. Shields, C. Trallero-Giner, M. Cardona *et al.*, Phys. Rev. B **46**, 6990 (1992).
[14] W. Kauschke, A. K Sood, M. Cardona, and K. Ploog, Phys. Rev. B **36**, 1612 (1987).
[15] A. J. Shields, M. P. Chamberlain, M. Cardona, and K. Eberl, Phys. Rev. B **51**, 17728 (1995).

Translated by M. E. Alferieff

Mechanism of field emission from carbon materials

A. N. Obraztsov, A. P. Volkov, and I. Yu. Pavlovskiĭ

M. V. Lomonosov Moscow State University, 119899 Moscow, Russia

Field emission in diamond and graphite-like polycrystalline films is investigated experimentally. It is shown that the emission efficiency increases as the nondiamond carbon phase increases; for graphite-like films the threshold electric field is less than 1.5 V/μm, and at 4 V/μm the emission current reaches 1 mA/cm^2, while the density of emission centers exceeds 10^6 cm^{-2}. A general mechanism explaining the phenomenon of electron field emission from materials containing graphite-like carbon is proposed. © *1998 American Institute of Physics.* [S0021-3640(98)01013-5]

PACS numbers: 79.70.+q, 81.05.Tp

Despite the considerable interest in the problem of field emission from polycrystalline diamond films, the mechanism of this phenomenon remains unexplained. On the one hand, it is generally acknowledged that negative electron affinity (NEA) on the diamond surface has a determining influence.[1,2] On the other hand the emission efficiency increases considerably as the fraction of nondiamond carbon, present on the intercrystallite boundaries in polycrystalline films, increases.[3,4]

In the present letter a comparative investigation is made of field emission from carbon films with different structure and phase composition. The films were obtained by gas-phase chemical deposition in the apparatus described in Ref. 5. Depending on the chosen parameters of the deposition process, the composition of the films varied over wide limits from polycrystalline diamond to graphite-like material. As an illustration, Fig. 1 displays Raman scattering (RS) spectra obtained for a typical polycrystalline diamond film consisting of micron-size faceted diamond crystallites (*1*), for a diamond film consisting of crystallites several nanometers in size (*2*), and for a film which can be classified as graphite-like, since its spectrum (*3*) does not contain any lines belonging to carbon with diamond structure, while the strongest line (near 1575 cm^{-1}) coincides with the RS line of graphite.[6]

The electron emission efficiency increased as the diamond crystallites decreased in size and, correspondingly, the fraction of nondiamond carbon increased, just as in the investigations mentioned earlier.[3,4] Unexpected, however, was the observation that the best field emission parameters were for films consisting of graphite-like carbon, where according to RS spectroscopy and reflection electron diffraction data the diamond phase is completely absent.

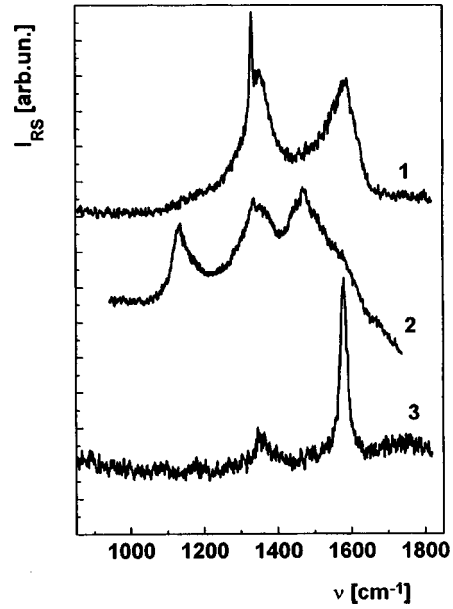Figure 2 shows the current–voltage characteristics, plotted in Fowler–Nordheim

FIG. 1. Raman scattering spectra $I_{RS}(\nu)$ for typical polycrystalline (*1*) and nanocrystalline (*2*) diamond films and for a graphite-like (*3*) film.
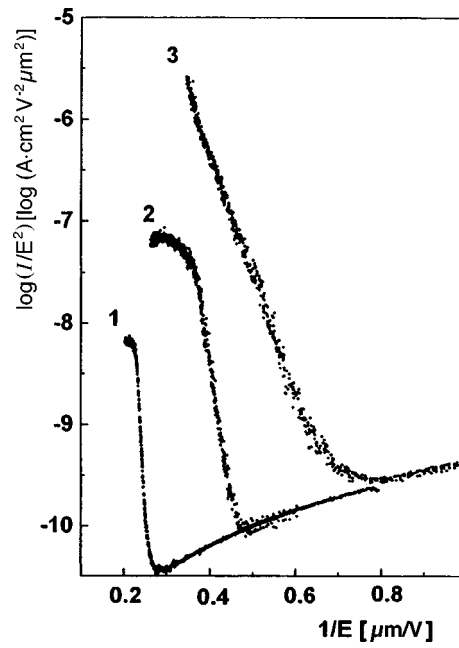

FIG. 2. Current–voltage characteristics of field emission for polycrystalline (*1*) and nanocrystalline (*2*) diamond films and for a graphite-like film (*3*).

coordinates, for the same typical films whose spectra are shown in Fig. 1. It follows from this figure that the threshold value E_{th} of the electric field giving rise to electron emission equals about 4 V/μm for polycrystalline diamond, 2 V/μm for nanocrystalline films, and less than 1.5 V/μm for graphite-like films. At the same time as E_{th} decreases, the emission current increases appreciably, reaching for graphite-like films 1 mA/cm^2 in a 4 V/μm field. The density of emission centers also increases considerably — from 10^2–10^3 cm^{-2} for diamond films up to 10^6–10^7 cm^{-2} for graphite-like films.

Each curve presented in Fig. 1 has a linear section corresponding to the dependence expressed by the well-known Fowler–Nordheim formula

$$I = A(\beta E)^2 \exp(-B\varphi^{3/2}/\beta E), \tag{1}$$

where $A = 1.4 \times 10^{-2}$ and $B = 6.8 \times 10^9$ for the current I in A/m^2, the electric field E in V/m, and the effective electron work function φ in eV; the parameter β characterizes the intensification of the electric field as a function of the surface morphology of the emitter. Formula (1) makes it possible to estimate from the experimental current–voltage characteristics (Fig. 2) the effective work function, which, assuming an ideally flat cathode surface ($\beta = 1$), varies from 0.08 for polycrystalline diamond films to 0.02 eV for graphite-like material. Such a low value of φ for polycrystalline films is ordinarily explained by the fact that electron emission occurs from the region of intercrystallite boundaries, which have a high conductivity compared with the main portion of the film material, which results in a local change in the electric field and a corresponding increase of the coefficient β in Eq. (1) occur. However, in contrast to polycrystalline diamond, graphite-like films consist of a material which is quite uniform with respect to the electrical conductivity, and according to scanning electron microscopy data their surface does not have any large protrusions.

At the same time, high-resolution transmission electron microscopy and reflection electron diffraction have established that these films consist of close-packed graphite crystals in the form of thin (1–10 nm) plates with transverse dimensions up to 1 μm, oriented predominantly in a manner so that the graphite basal crystallographic (001) planes are perpendicular to the substrate surface.[7] Thus, the surface of the film is formed by parallel (within the boundaries of each crystallite) rows of carbon atoms located on the borders of the layers of atoms with a typically graphitic structure. The distance between the rows equals the interplanar distance in graphite (about 0.34 nm).

It is well known that graphite is a semimetal (free electron density about 10^{18} cm^{-3}). The conductivity of graphite is due to partial overlapping of the $p\pi$ electron orbitals (one orbital from each carbon atom), oriented perpendicular to the basal plane and forming weak π bonds between neighboring atoms. The other three of the four valence electrons of carbon form strong σ bonds, lying in a plane which coincides with the basal plane. The weak π bonds are responsible for the formation of the electronic levels lying near the Fermi level, while the levels due to the strong σ bonds are displaced from the Fermi level, forming an energy gap of several electron-volts between the filled and vacant σ states. This situation is shown schematically in Fig. 3a in the form of the electron density of states.

Such arguments are evidently valid only for carbon atoms surrounded on all sides by the same atoms. If an atom is located at the edge of the basal plane, then some of its valence bonds will be dangling. This changes the electronic configuration of such atoms,
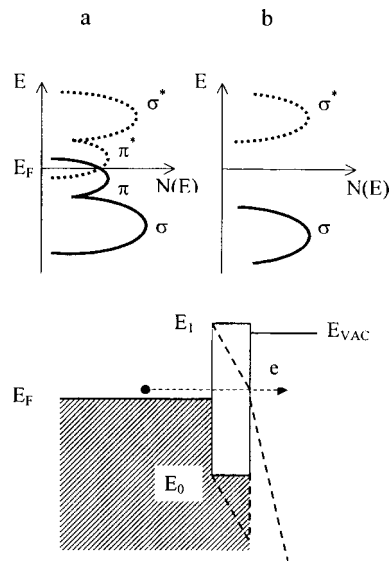
FIG. 3. Schematic representation of the electronic density of states $N(E)$ for graphite-like material (a) and for a layer of atoms with a modified electronic configuration (b). Energy diagram for an emitter, consisting of graphite-like material, in the absence of an external electric field (solid lines) and in the presence of a field giving rise to field emission into vacuum (dotted lines).

which, specifically, should be accompanied by the absence of overlap of the $p\pi$ electronic orbitals, vanishing of states located next to the Fermi level from the energy spectrum of the electrons, and formation of an energy gap similar to the band gap in diamond. The corresponding electronic density of states is shown schematically in Fig. 3b.

On account of the close packing of the graphite crystals comprising the film, carbon atoms with a modified electronic configuration form a virtually continuous monatomic layer on its surface. This layer can be characterized by a corresponding energy band structure (see Fig. 3). The validity of these considerations is confirmed indirectly by the fact that lines corresponding to photons with energies of about 4 and 2.5 eV are found in the cathodoluminescence (CL) spectra of the graphite-like films under discussion.[7] These lines could be due to radiative recombination accompanying the transition of electrons from the excited upper level E_1 into the ground state E_0 or the Fermi level (E_F) in the unmodified graphite part of the film (see Fig. 3).

On the basis of the general pattern for wide-gap materials,[1,2] it can be assumed that the surface of such graphite-like films has negative electron affinity, which is why the work function decreases. The electrical conductivity of the main part of the film is close to metallic, which allows the flow of a high current density. Under the influence of an electric field the electrons tunnel through the thin energy barrier at the interface of the two carbon phases and leave the surface of the emitter.

The proposed mechanism can, evidently, also occur in polycrystalline diamond films, which virtually always contain graphite-like carbon at the interface of the diamond crystallites. Moreover, this mechanism can explain the recently published results of investigations of field emission in carbon nanotubes, which consist of atoms with a typi-

cally graphite bond type. As was shown in Ref. 8, emission is observed only from the so-called ''open'' tubes, which contain carbon atoms located on the edge of the cylindrical surface. In Ref. 9 it is shown that electrons are emitted, forming a conical beam with a ring-shaped section, by atoms which are located on the edge of the graphite-like layer forming the tube.

In summary, field emission from graphite-like carbon films deposited by vaor-phase chemical deposition was obtained in our work. The mechanism proposed on the basis of the experimental facts makes it possible to explain the field emission observed for emitters consisting of different carbon materials, including polycrystalline and amorphous diamond films as well as carbon nanotubes.

[1] C. Bandis and B. B. Pate, Phys. Rev. B **52**, 12056 (1995).
[2] A. A. Dadykin, JETP Lett. **65**, 857 (1997).
[3] W. Zhu, G. P. Kochanski, S. Jin, and L. Seibles, J. Appl. Phys. **78**, 2707 (1995).
[4] B. S. Satyanarayana, A. Hart, W. I. Milne, and J. Robertson, Appl. Phys. Lett. **71**, 1430 (1997).
[5] I. Yu. Pavlovskiĭ and A. N. Obraztsov, Prib. Tekh. Eksp. **41**, 152 (1998).
[6] R. E. Shroder, R. J. Nemanich, and J. T. Glass, Phys. Rev. B **41**, 3738 (1990).
[7] A. N. Obraztsov, I. Yu. Pavlovsky, A. P. Volkov *et al.*, *Abstracts of the 2nd International Symposium on Diamond Electronics Devices,* Osaka, Japan, March 9–10, 1998, p. 10.
[8] A. G. Rinzler, J. H. Hafner, P. Nikolaev *et al.*, Science **269**, 1550 (1995).
[9] Y. Saito, K. Hamaguchi, K. Hata *et al.*, Nature **389**, 554 (1997).

Translated by M. E. Alferieff

Investigation of acceptor centers in semiconductors with the diamond crystal structure by the μ^-SR method

T. N. Mamedov,[a] V. N. Duginov, A. V. Stoykov, and I. L. Chaplygin
Joint Institute of Nuclear Research, 141980 Dubna, Moscow Region, Russia

D. Herlach and U. Zimmermann
Paul Scherrer Institute, CH-5232 Villigen PSI, Switzerland

V. N. Gorelkin
Moscow Physicotechnical Institute, 141700 Dolgoprudnyĭ, Moscow Region, Russia

J. Major and M. Schefzik
Max-Planck-Institut für Metallforschung, D-70569 Stuttgart, Germany

The residual polarization of negative muons in crystal silicon samples with phosphorus (P : 1.6×10^{13} cm^{-3}) and antimony (Sb : 2×10^{18} cm^{-3}) impurities is investigated. The measurements are made in a 1000 G magnetic field oriented in a direction transverse to the muon spin in the temperature range 4–300 K. The relaxation rate and shift of the precession frequency in the silicon sample with the phosphorus impurity are measured more accurately than previously. It is found that in antimony-doped silicon the acceptor center $_\mu$Al at temperatures below 30 K can be in both ionized and neutral states. The experimental data are interpreted on the basis of spin–lattice relaxation of the magnetic moment of an acceptor center, formation of acceptor–donor pairs, and recombination of charge carriers at the acceptor. Preliminary measurements showed a nonzero residual polarization of negative muons in germanium. © *1998 American Institute of Physics.*
[S0021-3640(98)01113-X]

PACS numbers: 76.75.+i, 61.72.Ss

The relaxation[1–3] and shift of the precession frequency[3] of the spin of negative muons was observed earlier in samples of *n*- and *p*-type silicon at temperatures below 30 K. The observation of the muon spin relaxation in silicon, which is a diamagnetic material, was explained by the paramagnetism of the intrinsic electronic shell of a silicon atom that has captured a negative muon. The radius of the muon orbit in the 1*S* state is 207 times smaller than the radius of the *K*-electron orbit, and the muon screens a unit of nuclear charge. A muonic atom has an electronic shell similar to that of an atom with nuclear charge $Z-1$, and in the medium it imitates an impurity atom. In the case of semiconductors a muonic atom is an acceptor impurity. Therefore investigation of the

behavior of the polarization of negative muons in semiconductors yields information about the interaction of an isolated acceptor center with the medium.

The application of the conventional methods (ESR, DESR, and so on) for investigating shallow acceptor centers in semiconductors with the diamond crystal structure are substantially limited because of the high spin–lattice relaxation rate and broadening of the resonance line by random deformations of the crystal.

The ESR signal corresponding to a boron atom in silicon was first observed[4] in 1960 with uniaxial compression of the crystal by a force of 300 kg/cm^2 and larger (see also Refs. 5 and 6). At present there is only one known work[7] reporting the observation of the ESR spectrum of a boron atom in silicon in an undeformed sample.

The present letter reports the results of an investigation of the temperature dependence of the residual polarization of negative muons in silicon with phosphorus and antimony impurities. Measurements were also made in graphite, germanium,[8] and copper.

The measurements were performed on the Stuttgart LFQ spectrometer[9] placed in the channel of the μE4 accelerator at the Paul Scherrer Institute (Switzerland). The transverse (with respect to the spin) external magnetic field produced at the sample by Helmholtz coils was equal to 1000 G. The impurity density in the silicon samples was (P) $= -1.6 \times 10^{13}$ cm^{-3} and (Sb) $= 2 \times 10^{18}$ cm^{-3}, respectively. The temperature of the sample was stabilized to within 0.1 K. The width of the time channel of the spectrometer was equal to 0.625 ns, and there were a total of 16000 channels in the spectrum.

Besides the target, some muons stop in the cryostat materials and in the scintillation counters and contribute to the observed spectrum. Since the lifetime of negative muons in the $1S$ state depends on the charge of the atomic nucleus, the instrumental spectrum of the temporal distribution of $\mu^- \to e^-$ decay electrons can be represented in the form

$$f(t) = \sum_X N_X e^{-t/\tau_X}[1 + \alpha p_X(t)] + B(t), \tag{1}$$

where N_X, τ_X, and p_X are, respectively, the pre-exponential factor, the muon lifetime, the projection of the polarization vector of a muon in the $1S$ state of the element X on the observation direction, α is the experimentally observed asymmetry factor of the spatial distribution of the decay electrons, with allowance for the electron detection solid angle, and B is the background of random coincidences.

The scintillation counters consist of hydrocarbons, while the cryostat is made of brass. Correspondingly, the components corresponding to muon capture by carbon and copper are always present in the spectra.

The experimental data were processed by the least-squares method. The lifetimes τ_X of negative muons in the $1S$ state of the atoms were fixed according to the average value of the experimental data[10] (2030, 760, 167, and 163 ns for carbon, silicon, germanium, and copper, respectively).

Independent measurements in graphite and copper established that: a) the contributions from the counters can be described by a polarization function of the form $p_C(t) = p_0 \cos(\omega t + \phi)$ with $\alpha p_0 = 0.009 \pm 0.002$; b) muons which have stopped in the cryostat walls (copper) become completely depolarized in a time shorter than 10^{-9} s, i.e.,

TABLE I. Amplitude and frequency of muon spin precession in graphite.

T, K	ω (fwd.), rad/μs	ω (bkwd.), rad/μs	a (fwd.), %	a (bkwd.), %
4	85.112 ± 0.017	85.102 ± 0.020	3.70 ± 0.09	4.14 ± 0.10
20	85.135 ± 0.018	85.121 ± 0.022	3.75 ± 0.10	4.20 ± 0.11
300	85.083 ± 0.017	85.128 ± 0.021	3.55 ± 0.09	4.14 ± 0.11
average	85.113 ± 0.008		3.65 ± 0.06	4.16 ± 0.07

$p_{Cu}(t) = 0$; and, c) the background of random coincidences has the form $B(t) = b_0 + \Sigma_{n=1}^2 b_n \cos(n\omega_{hf} t + \phi_n)$, where $\omega_{hf} = 2\pi\nu_{hf}$ is due to the temporal structure of the proton beam.

Table I gives the values of the amplitude $a = \alpha p_0$ and of the frequency of the precession of the muon spin in graphite, which were determined at different temperatures from the spectra from muon decay in the forward (fwd.) and backward (bkwd.) directions.

As one can see, $\delta\omega/\omega$ for separate measurements equals approximately 2×10^{-4}. The scatter in the data relative to the average value does not exceed the error of separate measurements. Therefore the long-time stability of the external magnetic field at the target is not less than 2×10^{-4}.

The lifetimes of negative muons in germanium and copper are close. For this reason, in processing the data for germanium the contributions of the target and copper in Eq. (1) were taken into account by a single exponential term, the lifetime being treated as a freely adjustable parameter. After a correction for the copper contribution, the following values were obtained for $a = \alpha p_0$ in germanium: (2.2 ± 0.2), (2.4 ± 0.2), (2.3 ± 0.2), and $(2.7 \pm 0.2)\%$ at 4.5, 30, 100, and 290 K, respectively.

The possible systematic errors arising in the calculation of the copper contribution were not taken into account. It follows from the data that the polarization of a muon in the $1S$ state of germanium is only 30–40% less than in carbon. To within the accuracy of the present measurements, relaxation of muon spin was not observed in germanium. The average value of the precession frequency of the muon spin, according to the data for 4.5, 30, 100, and 300 K, was equal to 84.9 ± 0.4 rad/μs.

Taking into consideration the relaxation of the muon spin at low temperatures, the polarization function for silicon was represented in the form

$$p(t) = p_0 e^{-\lambda t} \cos(\omega t + \phi),   \qquad (2)$$

where λ is the relaxation rate of the muon spin.

Figure 1 shows the temperature dependence of the relaxation rate λ and frequency shift $\delta\omega/\omega_0$, where ω_0 is the precession frequency at room temperature. The temperature dependence of the relaxation rate is described well by a power-law function $\lambda = dT^{-q}$, where $d = (4.0 \pm 0.7) \times 10^3$ μs^{-1}, $q = 2.73 \pm 0.06$, and temperature is expressed in kelvins. In the present work the value of the parameter q was determined to approximately four times better accuracy than in Refs. 2 and 3. The data presented in Fig. 1
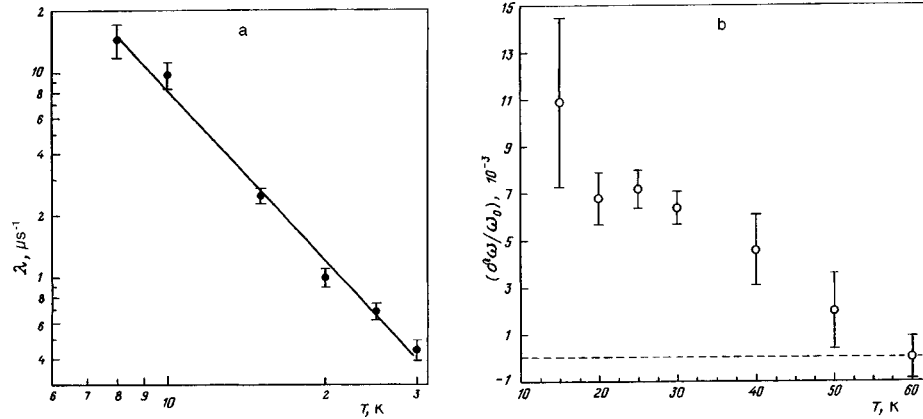
FIG. 1. Temperature dependences of the relaxation rate (a) and shift of the precession frequency (b) for a silicon sample doped with phosphorus ($\omega_0 = 84.89 \pm 0.04$ rad/μs) .

confirm the results of Ref. 3 that in phosphorus-doped silicon at temperatures $T < 30$ K there is a shift of the precession frequency of the muon spin. The accuracy of the measurements of $\delta\omega/\omega_0$ is approximately two times better than in Ref. 3.

In the case of antimony-doped silicon, preliminary analysis of the experimental data showed that the polarization function (2) presented above cannot be used to describe the experimental data at low temperatures. It was established that in the present case the polarization function is a sum of relaxing and nonrelaxing components. Therefore, for further analysis of the experimental data, the polarization function $p(t)$ was represented in the form:

$$\alpha p(t) = a_1 e^{-\lambda t} \cos(\omega_1 t + \phi_1) + a_2 \cos(\omega_2 t + \phi_2). \tag{3}$$

As a result of an analysis of the experimental data for antimony-doped silicon using the polarization function (3), it was found that the total amplitude $a_1 + a_2$ of the components is constant and equals the amplitude of the muon spin precession observed at the frequency of the free spin at room temperature. The amplitude a_1 of the relaxing component at 4.1 K equals approximately 85% of the total amplitude. The amplitude a_1 decreases as the temperature increases, and at 17 K one has $a_1 \simeq a_2$ (see Fig. 2a). along with the decrease in a_1, a decrease is observed in the relaxation rate of this component as the temperature increases. For this reason, the errors in determining a_1 and a_2 increase as temperature increases, and at 27 K and higher it is impossible to separate the components. Analysis of the data for 40 K with the function (2) shows that at this temperature a component decaying at a rate higher than 5×10^4 s^{-1} is absent in the spectrum. The temperature dependence of the relaxation rate λ of the relaxing component is much weaker in the present sample than in previously studied samples (see Fig. 2b). It is described better by an exponential function than a power-law function, though the existing data do not rule out a power-law dependence. Describing the data presented in Fig. 2b by a temperature dependence $\lambda = \eta \cdot e^{-\beta T}$, we obtained the following parameter values: $\eta = 16 \pm 2$ μs^{-1} and $\beta = 0.167 \pm 0.014$ K^{-1}. The precession frequencies of the muon spin for the relaxing and nonrelaxing components are different from one another. For the nonrelaxing component, it corresponds to the precession frequency of a free muon spin,
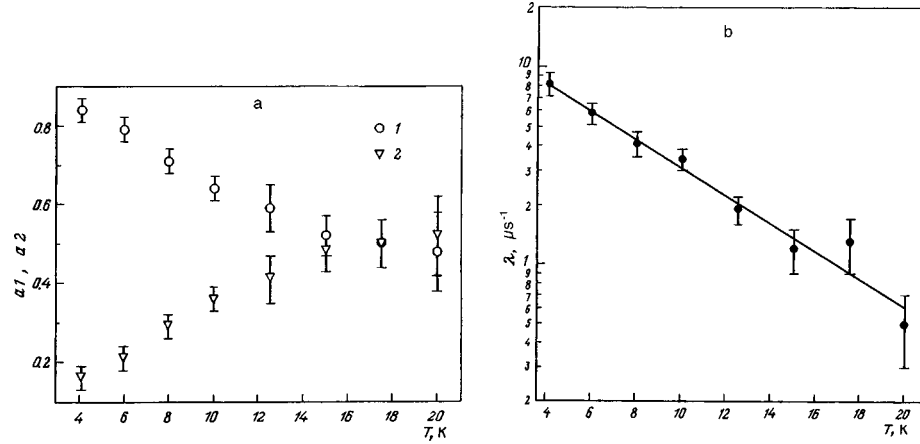
FIG. 2. Silicon sample doped with antimony: temperature dependences of the relative amplitudes of the relaxing (a1) and nonrelaxing (a2) polarization components (a) and of the relaxation rate (b).

while for the relaxing component at temperatures below 20 K a shift of the precession frequency is observed. The average frequency shift $\delta\omega/\omega$ in the temperature interval 8–20 K equals $(8.0 \pm 2.2) \times 10^{-3}$.

The observation of relaxing and nonrelaxing components of the residual polarization of negative muons attests to the fact that during the observations the muonic atom (acceptor center) can be found both in ionized (diamagnetic) $_\mu$Al$^-$ and un-ionized (paramagnetic) $_\mu$Al^0 states. Therefore it must be assumed that either the muonic atom initially forms (in a time shorter than $1/\Omega_{hf}$) in both the ionized and un-ionized states or it forms initially in one of these states and then makes a transition into the other state at a rate comparable to $1/\tau_{\mathrm{Si}}$.

Let us assume that a muonic atom is formed initially in the state 1, in which the muon spin relaxes at the rate λ and passes at the rate ν into the state 2, the reverse transition being absent. In an external magnetic field ($H\|z$) transverse to the muon spin, the time dependence of the complex polarization ($\mathbf{p}=p_x+ip_y$) in the states 1 and 2 obeys the following system of differential equations:

$$\frac{d}{dt}\begin{pmatrix} \mathbf{p}_1 \\ \mathbf{p}_2 \end{pmatrix} = \begin{pmatrix} -(\nu+\lambda)+i\omega_1 & 0 \\ \nu & i\omega_2 \end{pmatrix}\begin{pmatrix} \mathbf{p}_1 \\ \mathbf{p}_2 \end{pmatrix}. \tag{4}$$

The solution of this system with the initial conditions $\mathbf{p}_1(0)=1$ and $\mathbf{p}_2(0)=0$ gives the following dependence for $p_x=p_{1x}+p_{2x}$:

$$p_x(t)=C_1e^{-(\nu+\lambda)t}\cos(\omega_1 t+\phi_1)+C_2\cos(\omega_2 t+\phi_2), \tag{5}$$

where $C_1=\sqrt{\lambda^2+\delta^2}/\sqrt{(\nu+\lambda)^2+\delta^2}$ and $C_2=\nu/\sqrt{(\nu+\lambda)^2+\delta^2}$.

As one can see, the function $p_x(t)$ (5) is identical to the function (3) describing the experimental data for the antimony-doped silicon sample.

As was noted in the introductory remarks, the relaxation of muon spin in semiconductors is due to the relaxation of the magnetic moment of the electronic shell of a

muonic atom, which in the present case is an acceptor impurity. In the hydrogenlike atom approximation, often employed for describing the system acceptor center + hole, the relaxation rate λ of the muon spin can be expressed[14] in terms of the relaxation rate ν_r of the magnetic moment of the electronic shell of the acceptor center and the frequency Ω_{hf} of the hyperfine interaction of the magnetic moments of the muon and the electronic shell of an acceptor center:

$$\lambda = \Omega_{hf}^2/4\nu_r. \tag{6}$$

Using the value $\Omega_{hf}/(2\pi) \approx 650$ MHz from Ref. 11 and our value of λ, we find for phosphorus-doped silicon that $\nu_r = 1.6 \times 10^{12}$ s^{-1} at $T = 15$ K. For $T = 4$ K, finding λ by extrapolating the function $\lambda = dT^{-q}$, we obtain $\nu_r = 5 \times 10^{10}$ s^{-1}.

In the theoretical works[12,13] it was shown that one of the following processes makes the main contribution to the temperature dependence of the spin–lattice relaxation of shallow acceptor centers in silicon: a direct one-phonon process, Raman scattering of phonons (Raman process), and the Orbach process. The one-phonon process predominates at temperatures below 1 K, the Raman process predominates at intermediate temperatures, and the Orbach process predominates at high temperatures. However, the temperature at which the contribution of the Orbach process starts to exceed that of the Raman process is different according to data obtained by different authors[12,13] and lies in the interval 10–100 K. The spin–lattice relaxation rate is proportional to T for the one-phonon process, to T^5 (T^7) for Raman scattering, and to $\exp(-\Delta/T)$ for the Orbach process (Δ is the energy splitting of the levels of the acceptor center). The expected value of the relaxation rate at 4 K equals approximately 10^9 s^{-1} and in order of magnitude is consistent with the ESR measurements in silicon under uniaxial compression of the crystal.[5]

Our data do not permit drawing the conclusion that one of the above mechanisms of the relaxation of the magnetic moment of the electronic shell of an acceptor center predominates. Apparently, in the temperature range 4–40 K the one-phonon process makes a negligible contribution to the relaxation of the magnetic moment of an acceptor center. Our preliminary estimates show that in antimony-doped silicon the observation of a nonrelaxing component of the polarization of the muon spin could be due to the formation of acceptor–donor pairs and recombination of charge carriers and excitons on acceptor–donor pairs. In the event that the role of the acceptor–donor pair formation mechanism in the process of formation of an acceptor center in an ionized state is confirmed, the μ^-SR method can be used to study the kinetics of recombination of charge carriers on isolated acceptor centers.

[a]e-mail: tmamedov@nusun2.jinr.dubna.su

[1] T. N. Mamedov, V. N. Duginov, V. G. Grebinnik *et al.*, Hyperfine Interact. **86**, 717 (1994).
[2] W. Beez, T. Grund, M. Hampele *et al.*, PSI Newsletter, Annex **I**, 125 (1993).
[3] T. N. Mamedov, I. L. Chaplygin, V. N. Duginov *et al.*, Hyperfine Interact. **105**, 345 (1997).
[4] G. Feher, J. C. Hensel, and E. A. Gere, Phys. Rev. Lett. **5**, 309 (1960).
[5] G. W. Ludwig and H. H. Woodbury, Bull. Am. Phys. Soc. **6**, 118 (1961).
[6] T. Shimizu and N. Tanaka, Phys. Lett. A **45**, 5 (1973).
[7] H. Neubrand, Phys. Status Solidi B **86**, 209 (1978).

[8] Th. Stammler, R. Abela, Th. Grund *et al.*, Phys. Status Solidi A **137**, 381 (1993).
[9] R. Scheuermann, J. Schmidl, A. Seeger *et al.*, Hyperfine Interact. **106**, 295 (1997).
[10] T. Suzuki, D. F. Measday, and J. P. Roalsvig, Phys. Rev. C **35**, 2212 (1987).
[11] M. Koch, K. Maier, J. Major *et al.*, Hyperfine Interact. **65**, 1039 (1990).
[12] T. Shimizu and M. Nakayama, J. Phys. Soc. Jpn. **19**, 930 (1964).
[13] Y. Yafet, J. Phys. Chem. Solids **26**, 647 (1965).
[14] V. N. Gorelkin and D. V. Rubtsov, Hyperfine Interact. **105**, 315 (1997).

Translated by M. E. Alferieff

Low-energy inelastic collisions of excited hydrogen mesic atoms

L. I. Ponomarev

Kurchatov Institute Russian Science Center, 123182 Moscow, Russia

E. A. Solov'ev[a]

Macedonian Academy of Science and Art, Skopje, Macedonia

The advanced adiabatic approach (AAA) previously proposed for the description of collision problems in atomic physics is extended to the specific case of mesic atom collisions in excited states $n \geq 2$. Calculations of the muon transfer and Coulomb deexcitation rates in collisions of $(p\mu)_n$, $(d\mu)_n$, and $(t\mu)_n$ muonic atoms in excited states $n = 3,4,5$ with hydrogen isotopes p,d,t are presented. © *1998 American Institute of Physics.* [S0021-3640(98)00213-8]

PACS numbers: 36.10.Gv, 34.10.+x

1. There are several problems in muonic physics, weak interaction physics, and especially in the physics of muon-catalyzed fusion (see, e.g., Ref. 1) which require knowledge of the cross sections of different collisional processes of hydrogen isotope mesic atoms in the excited states $n \leq 6$ at collision energies $0.001 \leq \varepsilon \leq 100$ eV, $(a,b) = (p,d,t)$, in particular, muon transfer:

$$(b\mu)_n + a \xrightarrow{\lambda_n} (a\mu)_n + b, \tag{1}$$

and Coulomb deexcitation:

$$(a\mu)_n + b \xrightarrow{\lambda_{nn'}} (a\mu)_{n'} + b, \quad n' < n. \tag{2}$$

The main and only difference of processes (1)–(2) from the analogous atomic processes is the muon mass $m_\mu = 206.769 m_e$, which leads, nevertheless, to a substantial modification of the code based on the advanced adiabatic approach (AAA) which was previously proposed[2–4] for the description of the analogous collisional processes in atomic physics.

In the collision energy range $E \lesssim 100$ eV processes (1)–(2) are deeply adiabatic ($v/\alpha c \lesssim 0.1$) and the relative motion of the nuclei takes place in the almost static potential formed by the averaged muon and electron motion. In contrast to atomic collisions, where the classical description of the nuclear motion is well justified, low-energy mesic atom collisions (1)–(2) at $n \geq 2$ must be treated semiclassically.

In what follows we will present a self-consistent method of calculation of the rates of processes (1) and (2) which takes into account their peculiarities mentioned. It is based

      7

on the advanced adiabatic approach[2-6] modified to the specific case of mesic atom collisions. The first applications of this method were presented in Refs. 7 and 8, where the rates λ_n of the muon transfer (1) and the rates $\lambda_{nn'}$ of the Coulomb deexcitation in $(p\pi)_n$ atoms,

$$(p\pi)_n + p \rightarrow (p\pi)_{n'} + p \tag{3}$$

were calculated.

2. The Hamiltonian $\hat{H}$ of the Coulomb three-body problem (two nuclei + a muon) in Jacobi coordinates $(\mathbf{R}, \mathbf{r})$ has the form

$$\hat{H} = -\frac{1}{2M}\Delta_{\mathbf{R}} - \frac{1}{2m}\Delta_{\mathbf{r}} - \frac{Z_a}{r_a} - \frac{Z_b}{r_b} + \frac{Z_a Z_b}{R}. \tag{4}$$

Here Δ is the Laplacian operator, $\mathbf{R}$ is the vector of the internuclear distance, $\mathbf{r}$ is the muon coordinate, $M = (1/M_a + 1/M_b)^{-1}$ is the reduced mass of the two nuclei $(M_a \geqslant M_b)$, Z_a and Z_b are the charges of the nuclei, $Z_\mu = -1$ is the muon charge, $m = (1 + 1/(M_a + M_b))^{-1}$ is the reduced mass of the muon moving around the nuclei, and mesic atomic units (m.a.u.) are used ($\hbar = e = m_\mu = 1$).

The wave functions $\Psi(\mathbf{r},\mathbf{R})$ describing reactions (1)–(2) can be decomposed over the solutions $\varphi_j(\mathbf{r};R)$ of the Coulomb two-center problem[9]

$$\Psi(\mathbf{r},\mathbf{R}) = \sum_j \varphi_j(\mathbf{r};R)\frac{1}{R}F_j^J(R)Y_J(\Theta,\Phi). \tag{5}$$

Here J is the total angular momentum of the three-body problem, $\varphi_j(\mathbf{r};R)$ is the complete set of solutions of the Coulomb two-center problem

$$\hat{h}\varphi_j(\mathbf{r};R) = E_j(R)\varphi_j(\mathbf{r};R), \quad \hat{h} = -\frac{1}{2m}\Delta_{\mathbf{r}} - \frac{Z_a}{r_a} - \frac{Z_b}{r_b}, \tag{6}$$

describing the muon motion around fixed nuclei separated by a distance R; $j = [nn_1 n_2 mp]$ is the set of parabolic quantum numbers specifying the quantum state of the muon motion (p is the state parity: g stands for *gerade*, u for *ungerade*), $E_j(R)$ is the energy of a muon in the state j as a function of R.

After averaging over the muon motion, the nuclear motion is described by the set of equations

$$\frac{1}{2M}\frac{d^2 F_i^J(R)}{dR^2} + \left[\varepsilon - U_i(R) - \frac{J(J+1)}{2MR^2}\right]F_i^J(R) = \frac{1}{2M}\sum_j U_{ij}(R)F_j^J(R), \tag{7}$$

where $U_{ij}(R)$ are the nonadiabatic coupling potentials,[9] ε is the collision energy in the entrance channel, and $U_i(R)$ is the effective potential including the term $E_i(R)$, the Coulomb repulsion of the nuclei, and the electron screening effects at $R \gg 1$.[10]

In the limit $R \rightarrow \infty$ the adiabatic terms $E_i(R)$ converge to the energies of the isolated atoms $(\mu a)_i$ and $(\mu b)_i$ with a relative accuracy of only $\sim M^{-1}$. To incorporate isotopic effects, which play an important role in processes (1)–(2), the standard adiabatic approach should be modified, using the additional transformation suggested by Solov'ev.[11]
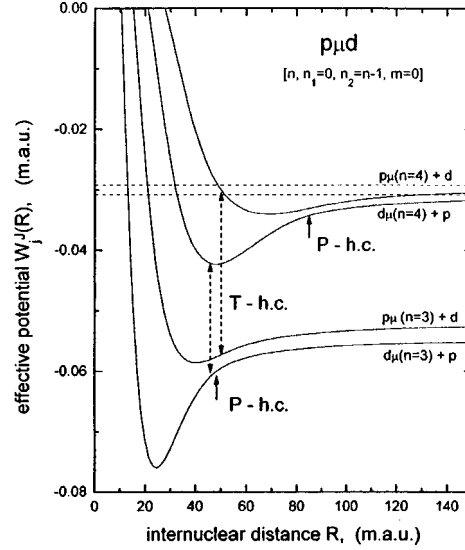
FIG. 1. The scheme of transitions $i=[nn_1n_2m] \rightarrow j=[n'n_1'n_2'm]$ in the system $pd\mu$ via P and T hidden crossings for the Coulomb deexcitation reaction (2).

It improves the accuracy of $E_i(\infty)$ to a level $\sim M^{-2}$ and splits the degenerate pair $E_{ig}(R)$ and $E_{iu}(R)$ into a pair $E_{ia}(R)$ and $E_{ib}(R)$, which represent the atoms $(a\mu)_n$ and $(b\mu)_n$, respectively, at $R \rightarrow \infty$ (see Fig. 1).

3. To leading order the solutions $F_i^J(R)$ of equation (7) can be written in the semi-classical form

$$F_i^J(R) = C_i[p_i^J(R)]^{-1/2} \exp\left\{ i \int_{c_{ij}} p_i^J(R)dR \right\}, \tag{8}$$

$$p_i^J(R) = \left[2M\left(\varepsilon - U_i(R) - \frac{J(J+1)}{2MR^2} \right) \right]^{1/2}.$$

According to the AAA, the nonadiabatic transitions from the adiabatic state i to the state j are determined by the hidden crossings of terms $E_i(R)$ and $E_j(R)$ in the complex plane R at $R=R_c=\mathrm{Re}\,R_c+i\,\mathrm{Im}\,R_c$, where $E_i(R_c)=E_j(R_c)$.

The cross sections of the transitions $i \rightarrow j$ are calculated with the formulas[2-4]

$$\sigma_{ij}(\varepsilon) = \frac{\pi}{p_i^2} \sum_{J=0} (2J+1)|S_{ji}^J|^2,$$

$$|S_{ji}|^2 = 2P_{ij}(1-P_{ij}), \quad P_{ij} = e^{-2\Delta_{ij}}. \tag{9}$$

$$\Delta_{ij} = \left| \mathrm{Im} \int_{c_{ij}} p(R)dR \right| = \left| \mathrm{Im} \int_{\mathrm{Re}\,R_c}^{R_c} [p_i(R) - p_j(R)]dR \right|,$$

c_{ij} is the contour in the complex R plane in the domain $(0,\infty)$, including the branch point R_c.

There are four types of hidden crossings: S, T, P, and Q series.[2–4] For processes (1)–(2) only the P and T series are essential. The T series connects the states $i = [nn_1 n_2 mp]$ and $j = [n'n_1'n_2'mp]$ with $n_1' = n_1, n_2' = n_2 + 1$, and the same parity p at $Z_a = Z_b$. The P series connects states $E_{ja}(R)$ and $E_{jb}(R)$ with the same set of parabolic quantum numbers $[nn_1 n_2 m]$ at slightly different charges Z_a and Z_b. The lower term $E_{ja}(R)$ belongs to the heavier atom $(a\mu)$ and corresponds at $M_a = M_b$ to the symmetric g state $(l = 2n_2)$, while the upper term $E_{jb}(R)$ corresponds to u state $(l = 2n_2 + 1)$.

4. The numerical code for the calculation of the cross sections of processes (1)–(2) is based on the automated program package ARSENY.[5,6] It includes subprograms for calculation of the terms $E_j(R)$ for states $j = [nn_1 n_2 mp]$, $n \leq 5$ (220 adiabatic states), a search for all branch points $R_c = \mathrm{Re}\, R_c + i\,\mathrm{Im}\, R_c$ of the hidden crossings in the complex R plane connecting pairwise terms $E_i(R_c)$ and $E_j(R_c)$, calculation of the Stueckelberg parameters $\Delta_{ij}(R_c)$, the S_{ji}^J matrix elements, and the cross sections $\sigma_{ij}(\varepsilon)$, the averaged cross sections[b] $\sigma_{nn'}(\varepsilon)$

$$\sigma_{nn'}(\varepsilon) = \sum_{n_1, n_2, n_1', n_2', m} \frac{2 - \delta_{0m}}{n^2} \sigma_{ij}(\varepsilon) \tag{10}$$

and transition rates

$$\lambda_{nn'} = \sigma_{nn'} v \rho_0, \tag{11}$$

where v is the relative velocity and $\rho_0 = 4.25 \times 10^{22} \mathrm{cm}^{-3} = 0.73 \times 10^{-3}$ m.a.u. is the liquid hydrogen density.

In Fig. 1, where only the terms $E_i(R)$ for the $pd\mu$ system with $m = 0$, $\Delta = -(n-1)$ at $n = 4$ and $n = 3$ are plotted as an example, the hidden crossings (h.c.) of the P and T types are marked by arrows. The muon transfer reaction (1) $(p\mu)_n \to (d\mu)_n$ is governed by the P-type series, while the T-type series are solely responsible for the Coulomb deexcitation (2)

$$(d\mu)_n + p \to (d\mu)_{n-1} + p, \tag{12}$$

and a combination of the P and T types is essential for the reactions

$$(p\mu)_n + d \to (p\mu)_{n-1} + d. \tag{13}$$

Relations (9)–(11) give the complete algorithm for the calculation of all cross sections $\sigma_{ij}(\varepsilon)$ and $\sigma_{nn'}(\varepsilon)$ at a given collision energy ε.

5. The calculated rates of processes (1)–(2) are presented in Figs. 2, 3, and 4. We do not compare our results with the results of numerous publications (Refs. 12–17 and many others) because all of them contain a fundamental mistake,[c] the origin of which lies in the following. For the description of mesic atomic collisions they all use the version of the AAA developed by Solov'ev and co-workers for atomic collisions. In the atomic case the typical collision energy (~ 10 keV/nucl) is much higher than the potential energy of the terms (~ 1 eV), and expressions (8) and (9) for $p_i(R)$ and Δ_{ij} can be simplified using a small parameter $2U_i(R)/Mv^2(R) \sim U_i(R)/\varepsilon \sim 10^{-4}$ in the following way:
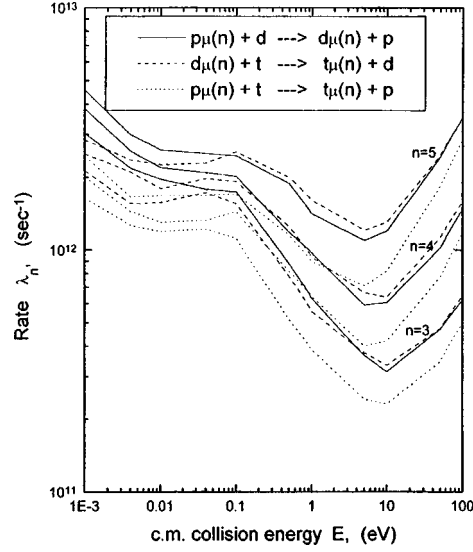
FIG. 2. The rates of the muon transfer reaction (1), $(b\mu)_n + a \rightarrow (a\mu)_n + b$, from the states $n = 3,4,5$.

$$p_i^J(R) = \left[2M\left(\varepsilon - U_i(R) - \frac{J(J+1)}{2MR^2} \right) \right]^{1/2}$$

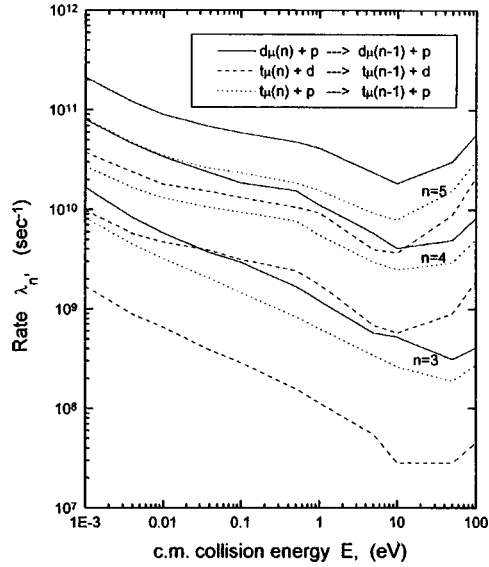$$= [M^2 v^2(R) - 2M U_i(R)]^{1/2} \approx M v(R) - U_i(R)/v(R),$$

where

FIG. 3. The rates of the Coulomb deexcitation $(a\mu)_n + b \rightarrow (a\mu)_{n-1} + b$ from the states $n = 3,4,5$.
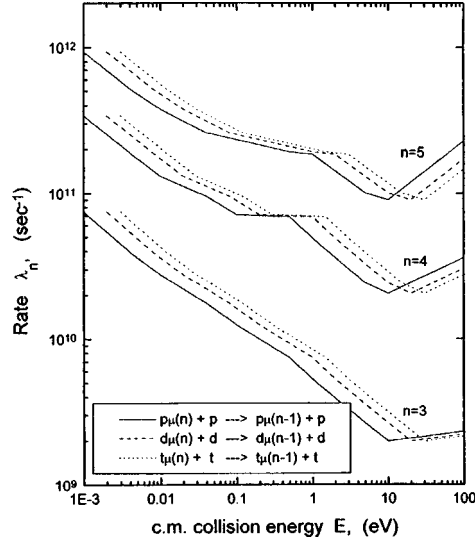
FIG. 4. The rates of the Coulomb deexcitation $(a\mu)_n + a \to (a\mu)_{n-1} + a$ from the states $n = 3,4,5$ in symmetrical systems.

$$v(R) = \left[\frac{2}{M}\left(\varepsilon - \frac{J(J+1)}{2MR^2} \right) \right]^{1/2}.$$

Hence,

$$\Delta_{ij} = \left| \mathrm{Im} \int_{\mathrm{Re}\,R_c}^{R_c} \frac{U_i(R) - U_j(R)}{v(R)} dR \right|. \tag{14}$$

In mesic atomic physics the typical collision energies $\varepsilon \lesssim 1$ eV and $U_i(R)$ ~ 100 eV, and the ratio $U_i(R)/\varepsilon \gtrsim 10^2$ is no longer a small parameter, so that relations (14) are entirely invalid. But just these relations, with the additional dubious assertion

$$v(R) = \frac{1}{2M}[p_i(R) + p_j(R)], \tag{15}$$

were used in Refs. 12–17 for the calculations of the cross sections (1) and (2).

6. The method presented in this paper is illustrated for the processes of muonic physics, but after simple scaling the results obtained also describe collision processes involving $a\pi^-$-, aK^-, and $a\bar{p}$ hydrogen-isotope exotic atoms ($a = p,d,t$). The rates $\lambda_{nn'}$ of the Coulomb deexcitation (2) of muonic atoms are calculated self-consistently for the first time in this paper. This opens the way for the *ab initio* theoretical description of the kinetics cascade of exotic atoms in the hydrogen isotope mixtures.

[a)]Permanent address: Research Coordinative Center on the Problems of Muon Catalyzed Fusion and Exotic Quantum Systems, 123098 Moscow, Russia.

[b)]The numerical results presented in Ref. 8 are calculated with this formula. Equation (9) in Ref. 8 contains a misprint (a factor of 1/2).

[c)]The comparison which was made in our previous paper[8] has shown a disagreement of the results with Ref. 17 by an order of magnitude at low collision energies.

[1] L. I. Ponomarev, Contemp. Phys. **31**, 219 (1990).

[2] E. A. Solov'ev, Zh. Éksp. Teor. Fiz. **81**, 1681 (19981) [Sov. Phys. JETP **54**, 893 (1981)].

[3] E. A. Solov'ev, Usp. Fiz. Nauk **157**, 437 (1989) [Sov. Phys. Usp. **32**, 228 (1989)].

[4] E. A. Solov'ev, in *The Physics of Electronic and Atomic Collisions*, edited by L. J. Dube *et al.*, AIP, Woodbury, New York, 1995, p. 471.

[5] E. A. Solov'ev, in *Proceedings of the Workshop on Hidden Crossings in Ion-Atom Collisions and in other Nonadiabatic Transitions*, Harvard Smithonian Center for Astrophysics, Cambridge, Mass., 1991.

[6] K. Richter and E. A. Solov'ev, Phys. Rev. A **48**, 432 (1993).

[7] V. V. Gusev, L. I. Ponomarev, and E. A. Solov'ev, Hyperfine Interact. **82**, 53 (1993).

[8] L. I. Ponomarev and E. A. Solov'ev, JETP Lett. **64**, 135 (1996).

[9] I. V. Komarov, L. I. Ponomarev, and S. Yu. Slavyanov, *Spheroidal and Coulomb Spheroidal Functions* (in Russian), Nauka, Moscow, 1976.

[10] L. I. Menshikov and L. I. Ponomarev, Z. Phys. D **2**, 1 (1986).

[11] E. A. Solov'ev, Yad. Fiz. **43**, 775 (1986) [Sov. J. Nucl. Phys. **43**, 492 (1986)].

[12] A. V. Kravtsov, A. I. Mikhailov, S. Yu. Ovchinnikov, and N. P. Popov, Muon Catal. Fusion **2**, 183 (1988).

[13] N. P. Popov, Muon Catal. Fusion **2**, 207 (1988).

[14] W. Czaplinski, A. Gula, A. V. Kravtsov *et al.*, Muon Catal. Fusion **5**, 183 (1990).

[15] A. V. Kravtsov and A. I. Mikhailov, Phys. Rev. A **49**, 3566 (1994).

[16] W. Czaplinski, A. Gula, A. Kravtsov, A. Mikhailov, and N. Popov, Phys. Rev. A **50**, 518 (1994).

[17] A. V. Kravtsov and A. I. Mikhailov, Zh. Éksp. Teor. Fiz. **107** 1473 (1995) [JETP **80**, 822 (1995)].

Pseudodipole interaction of ions with nonzero orbital angular momenta

S. V. Maleev[a)]

B. P. Konstantinov St. Petersburg Institute of Nuclear Physics, Russian Academy of Sciences, 188350 Gatchina, Leningrad Region, Russia

It is shown that the direct exchange interaction of ions possessing electrons (holes) with orbital angular momenta L and ℓ always contains a contribution $V_0 \mathbf{L} \cdot \ell + \mathbf{V}_1 (\mathbf{L} \cdot \hat{B})(\hat{B} \cdot \ell)$, where $\hat{B}$ is a unit vector along the bond connecting the ions. As a result, taking the spin–orbit interaction into account gives rise to a pseudodipole interaction of the spins (total angular momenta) of the ions under study and to uniaxial anisotropy. The possibility of using this pseudodipole interaction to explain the magnetic properties of cuprates is discussed. © *1998 American Institute of Physics.* [S0021-3640(98)01213-4]

PACS numbers: 75.30.Et, 71.70.Ej, 71.70.Gm

In recent years it has become clear that the noncollinear magnetic structure of a number of antiferromagnets can be explained only by assuming the existence of a pseudodipole interaction (PDI) between the spins (total angular momenta) of the ions.[1–5] This PDI depends on the relative orientation of the ion spins and the direction of the bond connecting them. In the simplest case it has the same structure as the ordinary magnetic dipole interaction:

$$V_{PD} = \frac{1}{2} \sum_{nn'} Q_{n'n} (\mathbf{S}_n \cdot \hat{R}_{n'n})(\mathbf{S}_{n'} \cdot \hat{R}_{n'n}), \tag{1}$$

where $\hat{R}_{nn'}$ are unit vectors connecting the spins $\mathbf{S}_n$ and $\mathbf{S}_{n'}$. However, for nearest neighbors $Q_{nn'}$ can be considerably greater than the magnetic dipole interaction and can have any sign depending on the particular physical situation. Moreover, at large distances the PDI decreases more rapidly than R^{-3}. Examples of systems with a PDI are the cuprates R_2CuO_4, where R=Pr, Nd, Sm, and Eu,[1,3] the weak ferromagnet $Sr_2Cu_3O_4Cl_2$ with a tetragonal lattice,[2] the compound $PrBa_2Cu_3O_{6-x}$ (Ref. 5), and the intermetallides U_2Pd_2X, where X=In, Sn.[5] Thus far the cuprates R_2CuO_4, where the PDI acts between Cu^{2+} ions in CuO_2 planes and between neighboring planes as well as between Cu^{2+} and R^{3+} ions, have been investigated in greatest detail.[1–3] In Ref. 4 the PDI parameters for Cu^{2+} ions in CuO_2 planes and between neighboring planes were determined from the spin-wave spectrum measured by the neutron-scattering method.

The PDI was postulated by Van Vleck in 1937. Apparently, the first microscopic derivation of this interaction was given in the famous paper by Moriya.[6] For rare-earth

metals it was analyzed in Refs. 7–9. Recently, a large number of works have been devoted to the theoretical analysis of the magnetism of CuO_2 planes in cuprates and, specifically, to the calculation of the PDI. We shall indicate only some of them.[10–13] The most detailed results are contained in Refs. 12 and 13, where, specifically, the magnitude of the PDI in the CuO_2 plane was calculated to be $P = 41$ μeV. However, an order of magnitude higher value $P = 0.45 \pm 0.04$ meV follows for Pr_2CuO_4 from the experimental data of Ref. 4. Such a large value of the PDI in Pr_2CuO_4 is also confirmed by ESR data[14] and by analysis of data[15] on elastic neutron scattering in Pr_2CuO_4 for samples placed in a magnetic field. The PDI also has a close value in $YBa_2Cu_3O_6$ (Ref. 16). Thus there is a discrepancy between the theoretical calculation and the experimental data. The reason for this discrepancy is not clear at present.

In the present letter I propose a new mechanism giving rise to a PDI that thus far has not been discussed in the literature. I shall show that for ions possessing electrons (holes) with nonzero orbital angular momenta, the direct exchange between the ions, with the spin–orbit coupling taken into account, leads to a pseudodipole interaction as well as to uniaxial anisotropy.

Consider two ions 1 and 2 possessing electrons (holes) with angular momenta L and ℓ and lying at the points $\pm a/2$, respectively, on the x axis. Their exchange interaction energy has the form

$$J = \sum_{M',M,m',m} V_{M',M,m',m} d^+_{M',\alpha} p^+_{m',\beta} d_{M,\beta} p_{m,\alpha}, \tag{2}$$

where $d_{M,\beta}$ and $p_{m,\alpha}$ are operators annihilating electrons (holes) in orbital states M and m and with spin projections α and β for the first and second ions, respectively, while the exchange integral has the form

$$V_{M',M,m',m} = \int d\mathbf{r}_1 d\mathbf{r}_2 \psi^*_{LM'}(\mathbf{r}_2) \varphi_{\ell m}(\mathbf{r}_2) V(\mathbf{r}_{12}) \psi_{LM}(\mathbf{r}_1) \varphi^*_{\ell m'}(\mathbf{r}_2), \tag{3}$$

where $V(\mathbf{r}_{12})$ is the Coulomb interaction potential of two electrons, while ψ_{LM} and $\varphi_{\ell m}$ are the wave functions of the first and second ions.

Evidently, $V_{M',M,m',m}$ is a matrix in the space of the quantum numbers of the ions 1 and 2 that can be decomposed in terms of the corresponding irreducible operators. Retaining the first two terms of such a decomposition, we have

$$V_{M',M,m',m} = J_0 \delta_{M',M} \delta_{m',m} + L^i_{M'M} V_{ij} \ell^j_{m'm} + \ldots, \tag{4}$$

where L and ℓ are the angular momentum operators of the ions. The first term in Eq. (4) leads to the standard exchange interaction ($s-d$ exchange), while the second term, as we shall see below, leads to crystallographic anisotropy and a PDI. It might also be mentioned that if one of the ions is replaced by conduction electrons, then the second term in Eq. (4) describes the skew scattering of conduction electrons by a localized orbital moment.[17]

For two isolated ions, it is obvious from symmetry considerations that

$$V_{ij} = V_0 \delta_{ij} + V_1 \hat{B}_i \cdot \hat{B}_j, \tag{5}$$

where $\hat{B}$ is a unit vector along the bond connecting the ions. It follows from Eqs. (3) and (4) that

$$V_{ij} = [(2L+1)(2\ell+1)L(L+1)\ell(\ell+1)]^{-1} Tr(L_i V\ell_j). \tag{6}$$

Following convention, I shall represent the wave functions of the ions in the form $\psi_{LM}(\mathbf{r}) = Y_{LM}(\hat{r})\psi_L(r)$ and $\varphi_{\ell m}(\mathbf{r}) = Y_{\ell m}(\hat{r})\varphi_\ell(r)$, where Y_{LM} are the standard spherical harmonics and $\hat{r} = \mathbf{r}/r$. However, it should be kept in mind that the centers of the ions 1 and 2 lie at the points $-\mathbf{a}/2$ and $\mathbf{a}/2$, respectively. As a result, we obtain from Eqs. (3) and (6) that the integrand in expression for V_{ij} contains the factor

$$\mathbf{R}_L(\hat{r}_1, \hat{r}_2) = [(2L+1)L(L+1)]^{-1} \sum_{M,M'} Y_{LM}(\hat{r}_1)\mathbf{L}_{MM'}Y^*_{LM'}(\hat{r}_2) \tag{7}$$

and an expression that is obtained from Eq. (7) by making the substitutions $L \to \ell$ and $\hat{r}_{1,2} \to \hat{r}_{2,1}$. The quantity $\mathbf{R}_L$ is, evidently, a t-odd axial vector, which depends on the unit vectors $\hat{r}_1$ and $\hat{r}_2$. For this reason, we have in the most general form

$$\mathbf{R}_L(\hat{r}_1, \hat{r}_2) = i[\hat{r}_2 \times \hat{r}_1]g_L, \quad g_L = g_L(\hat{r}_2 \cdot \hat{r}_1). \tag{8}$$

A simple calculation employing specific expressions for the spherical harmonics[18] gives $g_1 = (8\pi)^{-1}$, $g_2 = (\hat{r}_1 \cdot \hat{r}_2)(8\pi)^{-1}$ and $g_3 = [5(\hat{r}_1 \cdot \hat{r}_2)^2 - 1](32)^{-1}$. As a result, taking account of Eq. (5), we find

$$V_0 = \frac{1}{2} \int d\mathbf{r}_1 d\mathbf{r}_2 \{([\hat{r}_2 \times \hat{r}_1]_{\mathrm{I}} \cdot [\hat{r}_2 \times \hat{r}_1]_{\mathrm{II}}) - ([\hat{r}_2 \times \hat{r}_1]_{\mathrm{I}} \cdot \hat{B})([\hat{r}_2 \times \hat{r}_1] \cdot \hat{B})\}$$

$$\times g_{L\mathrm{I}}g_{\ell\mathrm{II}}\psi_L(r_2)\psi_L(r_1)\varphi_\ell(r_2)\varphi_\ell(r_1)V(r_{12}), \tag{9}$$

$$V_1 = \frac{1}{2} \int d\mathbf{r}_1 d\mathbf{r}_2 \{3(\hat{B} \cdot [\mathbf{r}_2 \times \mathbf{r}_1])_{\mathrm{I}}(\hat{B} \cdot [\hat{r}_2 \times \hat{r}_1])_{\mathrm{II}}$$

$$- ([\hat{r}_2 \times \hat{r}_1]_{\mathrm{I}} \cdot [\hat{r}_2 \times \hat{r}_1]_2)\}g_{L\mathrm{I}}g_{\ell\mathrm{II}}\psi_L(r_2)\psi_L(r_1)\varphi_\ell(r_2)\varphi_\ell(r_1)V(r_{12}),$$

where the subscripts I and II indicate that the centers of the first and second ions are the coordinate origin.

Formulas (2), (4), (5), and (9) together with the expression for the energy levels of ions in a crystal field with allowance for the spin–orbit interaction make it possible, in principle, to determine completely the direct bilinear exchange interaction of the spins (total angular momenta) of two ions with nonzero orbital angular momenta. However, this cannot be done in a general form. For this reason, I shall examine below two specific examples of the appearance of the PDI for weak spin–orbit coupling, and then I shall present some qualitative considerations about the PDI for the case of a strong LS interaction.

I. The PDI arising as a result of direct exchange between ions with $L = \ell = 2$ in a tetragonal environment. This example could be pertinent to $Sr_2Cu_3O_4Cl_2$ (Ref. 2). This substance contains planes which are arranged as follows: Additional Cu^{2+} ions (Cu II) are located at the centers of each second plaquette of the CuO_2 lattice (Cu I ions). Below $T_N \simeq 380$ K weak ferromagnetism is observed in this tetragonal material; this ferromagnetism was explained in Ref. 2 by the presence of a pseudodipole interaction between

pairs of ions Cu I and Cu II. Since there are no other ions along the bond connecting these ions, the appearance of a PDI between them as a result of direct exchange seems natural. Here it should be noted that the environment surrounding Cu I ions is different from that surrounding Cu II ions, and for this reason the crystal fields acting on these ions are not the same. What's more, generally speaking, the field acting on a Cu I ion does not possess tetragonal symmetry. However, for simplicity, in what follows I shall neglect these circumstances, taking which into account can only lower the symmetry of the final expression and change the specific form of the coefficients appearing in it. So, choosing the direction of the bond connecting the Cu I and Cu II ions as the $\hat{B}$ axis and taking account of Eqs. (2), (4), and (5), we obtain

$$V_{I,II} = -[V_0 \mathbf{L}_{M_1',M_1} \cdot \mathbf{L}_{M_2',M_2} + V_1(\hat{B} \cdot \mathbf{L}_{M_1',M_1})(\hat{B} \cdot \mathbf{L}_{M_2',M_2})]$$

$$\times (d_{M_1'\alpha}^+ d_{M_1\beta})_I (d_{M_2'\beta}^+ d_{M_2\alpha})_{II}, \tag{10}$$

where $d_{I,II}^+$ describe the creation of a d hole on the ions I and II, respectively, and $\hat{B} = (\hat{a} + \hat{b})2^{-1/2}$, where $\hat{a}$ and $\hat{b}$ are unit vectors along the x and y axes, directed along the Cu–O–Cu bonds in the CuO_2 planes.

I shall employ the following system of wave functions of the copper ions in the tetragonal crystal field:[12] $\psi_O \sim x^2 - y^2$, $\psi_1 \sim 3z^2 - r^2$, $\psi_X \sim yz$, $\psi_Y \sim zx$, and $\psi_Z \sim xy$, where z is the direction along the $\hat{c}$ axis, perpendicular to the CuO_2 planes. These functions are arranged in order of increasing energy. I shall assume below that $E_0 = 0$ and, in addition, that the states ψ_X and ψ_Y are degenerate and correspond to energy E_2. The spin–orbit interaction $\lambda \mathbf{S} \cdot \mathbf{L}$ mixes the states of the ions, and in first order of the perturbation theory the following substitution must be made in Eq. (10):

$$d_{M\alpha}^+ \rightarrow d_{M\alpha}^+ - \lambda \sum_{M_1} d_{M_1\mu}^+ (\mathbf{S}_{\mu\alpha} \cdot \mathbf{L}_{M_1,M}) E_{M_1,M}^{-\perp}. \tag{11}$$

As a result, since both ions are in the ground state, standard calculations yield

$$V_{1,2}^{(B)} = -2V_0 \frac{\lambda^2}{E_2^2}(\mathbf{S}_1 \cdot \mathbf{S}_2) - 2V_0 \lambda^2 \left(\frac{16}{E_Z^2} - \frac{1}{E_2^2}\right) S_{1z}S_{2z} - 2V_1 \frac{\lambda^2}{E_2^2}(\hat{B} \cdot \mathbf{S}_1)(\hat{B} \cdot \mathbf{S}_2). \tag{12}$$

Here the first term is a correction to the isotropic exchange, the second term is the uniaxial anisotropy energy, and the third term is the PDI along the bond connecting the ions Cu I and Cu II.

I shall now examine direct exchange between neighboring Cu^{2+} ions in a CuO_2 plane for a bond along the x axis. For this, in Eq. (12) $\hat{B}$ must be replaced by $\hat{a}$. It is convenient to represent the corresponding expression in the form

$$V_{1,2}^{(a)} = \delta J \mathbf{S}_1 \cdot \mathbf{S}_2 + A S_{1z}S_{2z} + P(S_{1x}S_{2x} - S_{1y}S_{2y}), \tag{13}$$

where $\delta J = -\lambda^2(2V_0 + V_1)E_2^{-2}$, $A = -[2V_0(16E_Z^{-2} - E_2^{-2}) - V_1 E_2^{-2}]\lambda^2$, and $P = -V_1\lambda^2 E_2^{-2}$. Interchanging x and y changes the sign of the last term in Eq. (13). The PDI in this form was used in Refs. 4 and 12 to study the spin-wave spectrum.

II. We have been examining direct exchange between copper ions. In fact, apparently, the main interaction between Cu^{2+} ions in a CuO_2 plane is superexchange via an

intermediate O^{2-} ion.[12] In this case hole transfers from copper ions to oxygen must be taken into account. Once again, for definiteness, I shall assume a bond along the x axis, and I shall characterize the hole states on the oxygen ion as follows:[12] $\varphi_0(\mathbf{r}) = \varphi_{2p_x}(\mathbf{r}) \sim x$, $\varphi_z(\mathbf{r}) = \varphi_{2p_y}(\mathbf{r}) \sim y$, and $\varphi_y(\mathbf{r}) = \varphi_{2p_z}(\mathbf{r}) \sim z$. Here and below the states of oxygen, in contrast to the states of the copper ion, are characterized by small letters.

I shall describe the transfer of a hole from copper to oxygen in the standard manner, introducing the interaction

$$T = \sum_{i=1,2} t_{M,m}(d^+_{iM\alpha}p_{m\alpha} + p^+_{m\alpha}d_{iM\alpha}), \tag{14}$$

where $p^+_{m\alpha}$ is an operator creating a hole on an O^{2-} ion, $t_{M,m} = t_{m,M}$, and the index i enumerates the two neighboring Cu^{2+} ions. According to Ref. 12, for a bond along the x axis the following transition integrals are different from zero: $t_{O,0}$, $t_{1,0}$, $t_{Y,y}$, and $t_{Z,z}$. The interaction (14) mixes p and d states, and as a result the substitution

$$p^+_{m\alpha} \to p^+_{m\alpha} - \sum_M d^+_{M\alpha}t_{M,m}E^{-1}_{M,m} \tag{15}$$

occurs. Now taking into account Eqs. (2), (4), and (5) and the expression for the spin–orbit interaction on the copper ion, I obtain the following expression for the superexchange interaction of copper ions for a bond along the x axis:

$$V^{(x)}_S = V^{(S)}_z S_{1z}S_{2z} + V^{(S)}_0 S_{1y}S_{2y}, \tag{16}$$

where $V^{(S)}_z = -32V_0\lambda^2 t_{O,0}t_{Z,z}(E^2_Z E_{O,0}E_{Z,z})^{-1}$ and $V^{(S)}_0 = -4V_0\lambda^2 t_{O,0}t_{Y,y} \times (E^2_2 E_{O,0}E_{Y,y})^{-1}$. It is obvious that for a bond along the y axis $S_{1y}S_{2y}$ in Eq. (16) must be replaced by $S_{1x}S_{2x}$. This does not change the coefficient $V^{(S)}_0$, since by virtue of the tetragonal symmetry $t_{Y,y} = t_{X,x}$ and $E_{Y,y} = E_{X,x}$. I note also that the product $S_{1x}S_{2x}$ is not present in Eq. (16). This is because $\ell_x\varphi_0 = 0$. Therefore the PDI has appeared as a result of spin–orbit interaction and is not due to the nonisotropic part of expression (5). However, in contrast to the results of Refs. 12 and 13, in the case a hand a PDI is present even in second order with respect to the hopping integrals t_{ab} and does not contain a small factor U^{-1}, where U is the Coulomb repulsion energy of the holes on a copper ion.

It is convenient to rewrite expression (16) in a form similar to Eq. (13):

$$V^{(a)}_S = \delta J_S \mathbf{S}_1 \cdot \mathbf{S}_2 + A_S S_{1z}S_{2z} + P_S(S_{1x}S_{2x} - S_{1y}S_{2y}), \tag{17}$$

where $\delta J_S = -P_S = V^{(S)}_0/2$ and $A_S = V^{(S)}_z - V^{(S)}_0/2$. However, this expression cannot be used directly to describe anisotropy and the PDI in the CuO_2 planes. Actually, according to Refs. 12 and 13, $T_{Z,z} = t_{Y,y}$, $E_Z \simeq E_2$, $E_{Z,z} \simeq E_{Y,y}$ and $A_S = 8V_0$ (the factor 8 in this expression is due to the values of the matrix elements: $L^z_{0z} = 2$ and $|\ell^y_y| = |L^y_y| = 1$). As a result, it turns out that $A_S = -(15/2)P_S$. At the same time, A_S and P_S determine the gaps Δ_{out} and Δ_{in} in the spectrum of spin waves polarized along the z axis and in the (x,y) plane, respectively.[4,12] It follows from the experimental data on neutron scattering in Pr_2CuO_4 that $A > 0$ and $|P| \simeq A/4$. Approximately the same relation holds in $YBa_2Cu_3O_{6+x}$ also.[16] Therefore $|P| > A$ in both cases, which contradicts the result obtained for P_S and A_S. Here it should be noted that the constant A calculated in Refs. 12

and 13 is close to the experimental value. However, the PDI turned out to be an order of magnitude weaker (see above). For this reason, the results of Refs. 12 and 13 also must be refined. In principle, the following variants are possible: 1) Direct exchange, studied above, between neighboring Cu^{2+} ions plays the main role; 2) the parameter data presented in Refs. 12 and 13 do not correspond to reality; and, 3) for a microscopic calculation of A and P it is insufficient to study an isolated triplet of ions $Cu^{2+}-O^{2-}-Cu^{2+}$.

For us, however, only one thing is important: The proposed simple model of direct exchange between ions with electrons possessing nonzero orbital angular momenta leads in a natural manner to both uniaxial anisotropy and a PDI, i.e., a dependence of the interaction of the spins on the direction of the bond connecting them. In other words, the symmetry breaking necessary for this is already present in this model.

III. I have examined the mechanism whereby a PDI appears between ions with weak LS coupling. Uniaxial anisotropy also arises at the same time. It is obvious that similar phenomena also occur in the case where one or both ions in a pair possess strong LS coupling. As a result, formulas of the type (12), (13), and (17), where one or both spins are replaced by the total angular momenta of the corresponding ions, should arise. Such a situation occurs in the compounds R_2CuO_4, where R=Pr, Nd, Sm, and Eu. Actually, noncollinear ordering of the angular momenta of rare-earth ions is explained by the PDI between the ions Cu^{2+} and R^{3+} (Refs. 1 and 3). Further, the two transitions, associated with the relative reorientation of copper spins in neighboring CuO_2 planes, that occur in Nd_2CuO_4 were explained by the PDI arising between Cu^{2+} ions as a result of superexchange along two competing paths, including one and two intermediate Kramers Nd^{3+} ions.[3,4] Here it is inevitably necessary to consider the PDI between two rare-earth ions with strong LS coupling. In this case the superexchange paths Cu–Nd–Cu and Cu–Nd–Nd–Cu are shortest, and for this reason the mechanism studied in the present letter whereby a PDI appears as a result of direct exchange between neighboring ions should play the main role.

In summary, I have examined a new mechanism leading to the appearance of a pseudodipole interaction and to uniaxial anisotropy as a result of direct exchange between ions with electrons (holes) possessing nonzero orbital angular momenta. I have also discussed the possibility of using this mechanism to describe the magnetic properties of cuprates.

[a]e-mail: Maleyev@thd.pnpi.spb.ru

[1] P. Bourges, L. Boudarene, and D. Petitgrand, Physica B **180−181**, 128 (1992).

[2] F. C. Chou, A. Aharony, B. J. Birgeneau, O. Entin-Wohlman *et al.*, Phys. Rev. Lett. **78**, 535 (1997).

[3] R. Sachidanandam, T. Yildirim, A. B. Harris, A. Aharony *et al.*, Phys. Rev. B **56**, 260 (1997).

[4] D. Petitgrand, S. V. Maleyev, P. Bourges, and A. Ivanov, submitted to Phys. Rev. B.

[5] S. V. Maleev, JETP Lett., in press.

[6] T. Moriya, Phys. Rev. **120**, 91 (1960).

[7] T. A. Kaplan and D. H. Lyons, Phys. Rev. **129**, 2072 (1963).

[8] P.-A. Lindgård, Phys. Rev. Lett. **78**, 4641 (1997).

[9] S. V. Maleev, JETP Lett. **61**, 44 (1995).

[10] W. Koshibae, Y. Ohta, and S. Maekawa, Phys. Rev. B **50**, 3767 (1994).

[11] F. Barriquand and G. A. Sawatzky, Phys. Rev. B **50**, 16649 (1994).

[12] T. Yildirim, A. B. Harris, A. Aharony, and O. Entin-Wohlman, Phys. Rev. B **52**, 10239 (1995).

[13] O. Entin-Wohlman, A. B. Harris, and A. Aharony, Phys. Rev. B **53**, 11661 (1996).

[14] V. V. Eremenko, S. A. Zvyagin, V. V. Pishko, S. N. Barilo *et al.*, JETP Lett. **52**, 338 (1990).

[15] I. W. Sumarlin, J. W. Lynn, T. Chattopadhyay, S. N. Barilo *et al.*, Phys. Rev. B **51**, 5824 (1995).

[16] P. Bourlet, J. Y. Henry, and L. P. Regnault, Physica C **296** (1998), in press.

[17] J. Kondo, Prog. Theor. Phys. **27**, 772 (1962).

[18] L. D. Landau and E. M. Lifshitz, *Quantum Mechanics: Non-Relativistic Theory*, 2nd ed., rev., Pergamon Press, New York, 1965 [Russian original, Moscow, 1963].

Translated by M. E. Alferieff

Giant population inversion of hot electrons in GaAs/AlAs type heterostructures with quantum wells

V. Ya. Aleshkin[a)] and A. A. Andronov

Institute of Microstructure Physics, Russian Academy of Sciences, 603600 Nizhniĭ Novgorod, Russia

The heating of electrons in an $Al_xGa_{1-x}As/GaAs$ ($x > 0.42$) hetero-structure in a lateral (directed along the heterointerfaces) electric field is studied. Population inversion on the size-quantization subbands of the Γ valley of GaAs and a giant population inversion between the X-valley states of $Al_xGa_{1-x}As$ and Γ-valley states of GaAs are predicted. The possibility of using these inversions for achieving stimulated IR emission is discussed. © *1998 American Institute of Physics.* [S0021-3640(98)01313-9]

PACS numbers: 42.55.Px, 78.66.Fd, 78.45.+h

Semiconductor heterostructures with quantum wells provide excellent possibilities for creating a new generation of lasers operating on intraband transitions in the mid- and far-IR range. ''Cascade''[1] and ''fountain''[2] lasers have already been made. In the present letter we discuss a new scheme for the formation of a population inversion of electrons and stimulated IR emission in a GaAs/AlAs semiconductor heterostructure grown on the (001) plane. In such heterostructures the GaAs lAyers are potential wells for Γ-valley electrons, while the AlAs layers are wells for X-valley electrons (see Fig. 1).[3] In addition, the conduction-band bottom in the GaAs layers is formed by Γ-valley states, while in AlAs layers it is formed by X-valley states. The method that we propose for producing a population inversion is based on three features of electron transport: First, the probability of electron transitions between GaAs and AlAs layers increases rapidly with increasing electron energy; second, the Γ-valley electron temperature is substantially higher than the X-valley temperature in high electric fields; and, third, the return of electrons from an AlAs X valley into the bottom subband of a GaAs Γ valley is suppressed. These features lead to giant accumulation of hot electrons in AlAs X-valleys, exceeding by more than an order of magnitude the similar accumulation occurring in bulk GaAs under Gunn effect conditions at similar values of the electric field E. At sufficiently high electric fields this accumulation leads both to a population inversion between subbands of GaAs Γ valleys and to a giant population inversion between the Γ and X valleys. Strong accumulation of hot electrons in X valleys of similar heterostructures was noted earlier in connection with an analysis of the spatial transport of hot electrons[4] (see also Ref. 5).

In the heterostructures considered, mixing (interaction) of Γ- and X-valley states occurs at the heterointerface (see, for example, Refs. 6 and 7). This mixing gives an
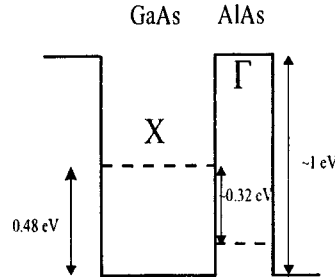
FIG. 1. Position of the edges of Γ and X valleys in a GaAs/AlAs heterostructure.

additional channel for electron transitions between X and Γ valleys, and it also removes the forbiddenness on radiative transitions between the valley states. For this reason, a population inversion of electrons between X and Γ valleys, just as, of course, between Γ-valley subbands, can be used to amplify IR radiation.

As an example, Let us consider an $Al_{0.85}Ga_{0.15}As/GaAs$ heterostructure with layers of the solid solution 35 Å thick and GaAs layers 75 Å thick. As a result of size quantization and deformation of the $Al_{0.85}Ga_{0.15}As$ layers, the X valleys separate into two groups: X_Z valleys and $X_{X,Y}$ valleys. The X_Z valleys are bulk-material X valleys whose minimum is displaced from the center of the Brillouin zone in the direction of growth, and the minima of the $X_{X,Y}$ valleys are displaced in directions lying in the growth plane. Only X_Z-valley states mix with Γ-valley states at the heterointerface.

Strictly speaking, the structure under study is a superlattice. However, the subbarrier states can be regarded as discrete, since the widths of the corresponding allowed bands of the superlattice do not exceed several meV. We shall treat the above-barrier states approximately as three-dimensional.

For electron exchange between the GaAs and $Al_{0.85}Ga_{0.15}As$ layers, above-barrier X-valley states and all size-quantization subbands possessing states with energies less than the bottom of the X valleys in GaAs are important. The positions of the edges of such size-quantization subbands of Γ, L, and X valleys calculated for the heterostructure under study in the Kane model are shown in Fig. 2. One can see from Fig. 2 that in GaAs layers there are five subbands below the X valley: three Γ subbands and two fourfold degenerate L subbands. The $Al_{0.85}Ga_{0.15}As$ layers have six subbands: four X_Z subbands and two twofold degenerate $X_{X,Y}$ subbands. To increase the probability of a radiative X_Z–Γ transition and to obtain an inversion between Γ subbands in GaAs, the parameters of the structure were chosen as follows: First, the X_Z subband was the bottom subband in $Al_{0.85}Ga_{0.15}As$ and, second, not far from the bottom this subband crossed a second Γ subband.

The mobility of the electrons in X valleys is much lower than in Γ valleys, since the electron effective mass in X valleys is larger than in Γ valleys; in addition, in the X valleys there is an additional strong mechanism of electron scattering — intervalley scattering. For this reason, in high fields the average kinetic energy of Γ-valley electrons (effective electron temperature) is much higher than that of X-valley electrons.[8]

Let us now examine electron transitions from states localized in the GaAs into states
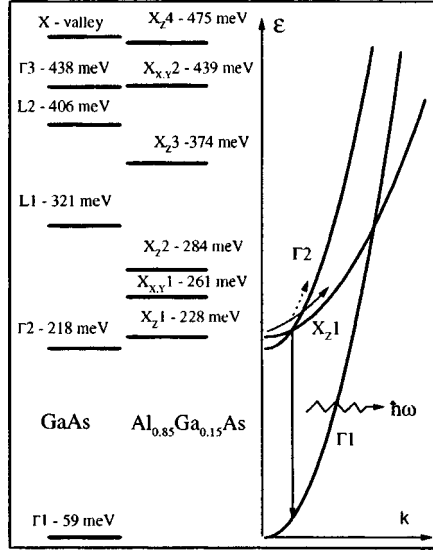
FIG. 2. Position of the edges of the size-quantization subbands in the heterostructure GaAs – 76 Å, $Al_{0.85}Ga_{0.15}As$ – 35 Å. Energy is measured from the Γ-valley bottom in GaAs. The wave number dependences of the electron energy in the $\Gamma1$, $\Gamma2$, and X_Z1 subbands and an optical transition are presented on the right-hand side of the figure. A direct transition from a X_Z1 subband into a $\Gamma2$ subband is indicated schematically (dotted arrow).

localized in the $Al_{0.85}Ga_{0.15}As$. There are four main mechanisms for such transitions. First, an electron with sufficient energy can undergo a direct transition from a Γ valley into one of the X_Z subbands through the heterointerface[3,4] on account of the mixing of the states of these valleys. Second, an electron can pass from a Γ subband into one of the X subbands, having emitted an intervalley phonon. Third, an electron can scatter from a Γ subband into one of the L subbands,[4,7] and then scatter from it into a X subband. In this case, all scatterings occur with emission of intervalley phonons. Finally, fourth, an electron, having emitted an intervalley phonon, can end up in above-barrier states of the X valleys[8] (three-dimensional) and from there scatter into X-valley states localized in the $Al_{0.85}Ga_{0.15}As$.

The probabilities of transitions between the states of subbands i and j with emission of intervalley phonons can be written in the form (the nonparabolicity of the bands is neglected):

$$\nu_{i,j} = \frac{D_{i,j}^2 m_j}{2\rho\hbar^2\omega_0} I^2, \quad I^2 = \int dz |\Psi_i|^2 |\Psi_j|^2, \tag{1}$$

where $D_{i,j}$ is the intervalley coupling constant of the valleys i and j, m_j is the effective mass of the density of states in the jth valley, ρ is the density of GaAs, ω_0 is the intervalley phonon frequency, $\Psi_{i,j}$ are wave functions, I^2 is the overlap integral, and the z axis is aligned along the direction of growth. If the states i and j are localized in different layers, then the overlap integrals are small ($I^2 \sim 10^{-2}$) and increase as the number of the subband increases.

Direct transitions occur at locations where the size-quantization subbands of the Γ and X_Z valleys cross in momentum space (see Fig. 2). The probability of these transitions is strongly affected by the magnitude of the electric field, which works to ''drag'' electrons through the crossing point with no change of subband. If the probability of a direct transition from the Γ subband i into the X_Z subband j is low, then it can be found by perturbation theory:

$$D_{i,j}(k_\perp) = \frac{2\pi V^2}{\hbar^2 e E k_\parallel(k_\perp)} \frac{m_t - m_\Gamma}{m_t m_\Gamma}, \quad V = \alpha|\Psi_{\Gamma i}(0)\Psi_{Zj}(0)|, \tag{2}$$

where $k_\parallel$ is the magnitude of the wave vector component along the electric field, corresponding to the crossing point of the subbands; $k_\perp$ is the wave vector component perpendicular to the electric field; m_t is the transverse electron mass in a X valley; m_Γ is the electron mass in a Γ valley; V is the effective interaction energy of the subbands; $\alpha = 0.155$ eV·Å is the interaction constant between the X and Γ valleys at the heterointerface;[3] and, $\Psi_{\Gamma i}(0)$ and $\Psi_{Zj}(0)$ are the values of the wave functions of the subbands at the heterointerface. In fields of several kilovolts per centimeter the probability of a direct transition is of the order of 10^{-2}. If the distribution function of electrons in the subband i on the line of intersection is assumed to be constant and equal to f, then the corresponding flux from the subband i into subband j does not depend on the magnitude of the electric field:

$$J_d = \frac{2V^2}{\hbar^3} \frac{(m_t - m_\Gamma)f}{m_t m_\Gamma}. \tag{3}$$

Electrons return from the $Al_{0.85}Ga_{0.15}As$ to the GaAs mainly into the $\Gamma 2$ subband (emission of an intervalley phonon and direct transition) and into the $\Gamma 1$ subband (emission of an intervalley phonon). On account of the smaller overlap integral, transitions into the $\Gamma 1$ subband with emission of an intervalley phonon are suppressed compared with transitions into the $\Gamma 2$ subband, while direct transitions into the $\Gamma 1$ subband are unlikely, since the location of the crossing of the first Γ and X_Z subbands lies quite high above the bottom of the first X_Z subband, and there are simply no electrons there. As a result, electrons return mainly into the $\Gamma 2$ subband.

For high electron temperatures in the Γ valley the probability of an electron leaving the GaAs is higher than the probability of an electron entering it. Indeed, electrons with high kinetic energy have a high probability of being scattered both into above-barrier states of the X valleys and into the upper X subbands on account of the large overlap integrals. The probability of direct transitions into the upper X_Z subbands is also higher because of the increase in the effective interaction energy of X and Γ valleys. Conversely, it is actually impossible for electrons to return to the GaAs via above-barrier states of X valleys because of the low electron temperature in the $Al_{0.85}Ga_{0.15}As$. This is what results in the accumulation of electrons in the first X_Z subband in $Al_{0.85}Ga_{0.15}As$. We underscore that the probability of electrons entering the $\Gamma 2$ subband is higher than that of their entering the $\Gamma 1$ subband. This is the reason for the inversion of the populations of the $\Gamma 1$ and $\Gamma 2$ subbands.

Figure 3 shows the computed ratios of the electron densities in the $\Gamma 2$ and $\Gamma 1$ subbands as a function of the electron temperature in the Γ valley for three values of the
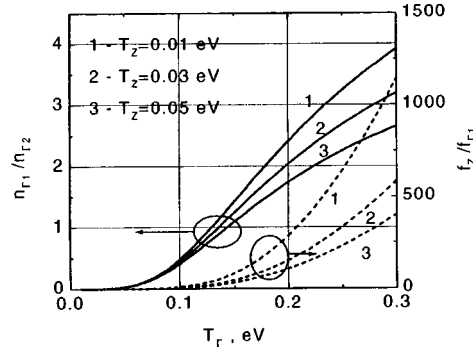
FIG. 3. Ratio of the densities in the second and first size-quantization subbands versus the electron temperature in the Γ valley (solid lines). The broken lines show the ratio of the occupation probabilities of the bottom of the first X_Z and Γ subbands.

electron temperature in the X_Z valley. The figure also shows the ratio of the occupation probabilities of the bottom states in the first X_Z and $\Gamma 1$ subbands. In the calculation, the distribution functions in the Γ and X subbands were assumed to be Maxwellian with corresponding temperatures, and the material parameters were taken from Refs. 3 and 8. One can see from Fig. 3 that a population inversion is realized in a wide interval of electron temperatures. The large (''giant'') values of the ratio of the occupation probabilities of the edges of the first X_Z and $\Gamma 1$ subbands signify that in sufficiently high fields almost all of the electrons are located in the $Al_{0.85}Ga_{0.15}As$ layers.[4]

We note the following about the electric field dependence of the electron temperatures. In GaAs at fields ~ 3 kV/cm a sharp increase of the electron temperature, due to electron runaway,[3] is observed in a Γ valley, and $T_\Gamma \sim 0.1$ eV in a 4 kV/cm field.[8] We feel that there are no grounds for believing that the runaway condition in the heterostructure under study should differ much from that for bulk GaAs. Therefore a population inversion should arise in fields exceeding 3–4 kV/cm. Since the overwhelming majority of the electrons in this case are in X valleys of $Al_{0.85}Ga_{0.15}As$, there should be no domain (Gunn) instability.

As we have said, electronic transitions between $\Gamma 1$ and $\Gamma 2$ subbands and between $\Gamma 1$ and the bottom $X_Z 1$ subbands contribute to the amplification of IR radiation. Estimates of the gain for a structure with doping level $\sim 10^{11}$ cm^{-2} per period give $\sim 10^2$ cm^{-1} for a wavelength of 8 μm. This indicates that there is a realistic possibility of realizing a new family of lasers operating in the mid- and far-IR ranges on intraband transitions in heterostructures. The wavelength of the radiation in such lasers can be changed by using $Al_y Ga_{1-y} As / Al_x Ga_{1-x} As$ ($y < 0.45$, $x > 0.45$) heterostructures.

[a)]e-mail: aleshkin@ipm.sci-nnov.ru

---

[1] J. Faist, F. Capasso, D. L. Sivko *et al.*, Science **264**, 553 (1994).

[2] O. Gauthier-Lafaye, P. Boucaud, F. H. Julien *et al.*, Appl. Phys. Lett. **71**, 3619 (1997).

[3] S. Adachi, J. Appl. Phys. **58**, R1 (1985).

[4] N. Z. Vagidov, Z. S. Gribnikov, and V. M. Ivashchenko, Fiz. Tekh. Poluprovodn. **24**, 1087 (1990) [Sov. Phys. Semicond. **24**, 684 (1990)].

[5] Z. S. Gribnikov, K. Hess, and G. A. Kosinovsky, J. Appl. Phys. **77**, 1337 (1995).

[6] Y. Garbonneau, J. Beerens, L. A. Cury *et al.*, Appl. Phys. Lett. **62**, 1955 (1993).

[7] J. J. Finley, R. J. Teissier, J. W. Cockburn *et al.*, Phys. Status Solidi B **204**, 215 (1997).

[8] M. Shur, *GaAs Devices and Circuits,* Plenum Press, New York, 1987 [Russian translation, Mir, Moscow, 1991].

Translated by M. E. Alferieff

Level statistics inside the core of a superconductive vortex

M. A. Skvortsov and M. V. Feigel'man

L. D. Landau Institute of Theoretical Physics, 117940 Moscow, Russia

V. E. Kravtsov

L. D. Landau Institute of Theoretical Physics, 117940 Moscow, Russia;
International Center for Theoretical Physics, 34100 Trieste, Italy

A microscopic theory of the Efetov supermatrix sigma-model type is constructed for the low-lying electron states in a mixed superconductive–normal system with disorder. This technique is used for the study of the localized states in the core of a vortex in a moderately clean superconductor with $\tau^{-1} \gg \omega_0 \sim \Delta^2/E_F$. At low energies $\epsilon \ll \omega_{\text{Th}} \sim (\omega_0/\tau)^{1/2}$, the energy level statistics is described by the "zero-dimensional" limit of this supermatrix theory, and the result for the density of states is equivalent to that obtained within Altland–Zirnbauer random matrix model. Nonzero modes of the sigma model increase the mean interlevel distance by the relative amount $[2 \ln(1/\omega_0\tau)]^{-1}$. © *1998 American Institute of Physics.*
[S0021-3640(98)01413-3]

PACS numbers: 74.60.Ec, 74.25.Jb, 74.80.Fp

There is a great deal of activity directed to the study of electron energy levels and wave functions in disordered normal metals,[1] where they govern the low-temperature transport properties. In (s-wave) superconductors, disorder is usually of less importance, since the excitation spectrum has a nonzero gap and single-electron states are almost empty at $T \ll \Delta$. The situation is quite different in mixed superconductive–normal systems (for a recent review see Ref. 2) where the gap in the excitation spectrum can be: i) very low compared to the bulk value Δ, or ii) exactly zero. An example of the first case is presented by an S–N–S sandwich with the thickness of the N region $L_N \gg \xi, l$. At generic values of the phase difference φ between superconductors the gap in the electron spectrum in the N region is of the order of the Thouless energy $E_{\text{Th}} = D/L_N^2 \ll \Delta$. To calculate the density of states (DoS) fluctuations at $\epsilon > E_{\text{Th}}$, and other mesoscopic effects in such systems, a field theory was developed[3] which is an extended version of Efetov's supermatrix σ model. A qualitatively different situation arises in case ii), which is realized, e.g., in the same S–N–S sandwich at $\varphi = \pi$ (Ref. 4) or in a variety of situations where an external magnetic field is present. Now the DoS is nonzero at arbitrary low energies, and quantum interference due to Andreev scattering strongly affects even the average DoS $\langle \rho(\epsilon) \rangle$. General approach to this kind of systems was initiated by Altland

and Zirnbauer (AZ),[5] who employed a generalized random-matrix (RM) approach. The particle–hole symmetry of the Bogolyubov–de Gennes (BdG) Hamiltonian leads to the constraints to be imposed on the RM Hamiltonians. The precise form of the constraint depends on the presence or absence of time inversion and spin rotation symmetries. Thus AZ identified 4 new classes of RM ensembles appropriate for the description of this kind of S–N–S systems. Crossover between such classes has been considered in Ref. 6 using the space-independent supermatrix sigma model. While the AZ approach is highly suggestive, it has the same limitation as any *ad hoc* RM theory, i.e., the limits of its applicability to some real physical system are left undetermined.

In the present letter we develop a microscopic field-theory approach to an example of a system of type ii), namely, to the core of a superconductive vortex. It has been known since the paper by Caroli, de Gennes, and Matricon (CdGM)[7] that the BdG equations near the vortex possess localized solutions with energies well below the bulk value Δ. The spacing ω_0 between these localized levels is of the order of $\Delta/(k_F\xi)$ and disappears in the quasiclassical limit $k_F\xi\to\infty$. Thus it was tempting to consider the vortex core as a kind of a ''normal tube'' inside a superconductor, and in many cases such a simplified picture was found[8] to be at least qualitatively correct. Later it was demonstrated[9] that the presence of a quasi-continuum spectrum branch localized on the vortex follows from general topological arguments. However, it is not always possible to consider the chiral branch as a continuous one. It was shown recently[10,11] that the discreteness of the localized energy levels becomes of real importance in layered superconductors at sufficiently low temperatures. In the previous paper[10] we employed the AZ approach to find low-current nonlinearities in the current–voltage relation in a mixed state of a moderately clean superconductor (the mean free path $l\gg\xi$, but $l\ll\xi(k_F\xi)$). In such a case the inverse elastic scattering time $1/\tau$ is much larger than interlevel spacing ω_0, and therefore the applicability of an appropriate RM model (which is, in fact, class C of the AZ classification) seems natural. Another, qualitatively different, limiting case of an ultraclean superconductor with extremely low concentration of impurities ($l\gg k_F\xi^2$) was considered recently by Larkin and co-workers.[11] In the present letter we again consider a moderately clean limit $\omega_0\ll1/\tau\ll\Delta$, now within a microscopic approach starting from the BdG equations in the presence of a Gaussian random potential. We derive the conditions under which the AZ class C statistics is indeed realized in the vortex core, and estimate the scale of nonuniversal corrections to it. We consider here a purely 2D superconductor, which is a good approximation for the case of a strong layered anisotropy (see Ref. 10 for more details).

Below we briefly present our method and results (see Ref. 12 for details). In the present problem even the calculation of the average single-particle quantities is not trivial and cannot be done within the quasiclassical theory, as long as low energies $\epsilon\sim\omega_0$ are considered. Thus our goal is to derive a field-theory technique for the calculation of the average DoS. To average the Green function over disorder, we use a standard trick[1] of representing it as the functional integral over both the Grassmann (χ) and usual complex (S) fields which combine into the superfield Φ. The most direct way would be to work with a real-space-dependent superfield $\Phi(\mathbf{r})$; in this way we would obtain a field theory in terms of a supermatrix $Q(\mathbf{r})$. On the other hand, low-lying states of the chiral branch depend upon a single quantum number only, as well as for a generic 1D problem. Therefore, in the basis of such states the BdG Hamiltonian can be represented as a

random $N \times N$ Hermitian matrix (where $N \sim \Delta/\omega_0$ is the total number of localized states in the core) of a certain structure and symmetry which we will discuss below. In the clean limit, $1/\tau \ll \Delta$, the admixture of delocalized ($\epsilon > \Delta$) states to the low-lying ones can be neglected. Thus it is convenient first to reduce the full 2D problem to a sort of RM problem that can be further reduced to a 1D field theory explicitly containing the chiral spectrum branch only.

In the basis of the CdGM states $\Psi_\mu(\mathbf{r}) = A(J_{\mu-1/2}(k_F r), J_{\mu+1/2}(k_F r))^T e^{i\mu\theta} e^{-K(r)}$ determined in Ref. 7 (here $A \sim \sqrt{k_F/\xi}$ is the normalization constant, θ is the azimuthal angle in the real space, $\mu \in [-N/2, N/2]$ is the angular momentum that takes half-integer values, and $K(r) = (1/\hbar v_F) \int_0^r \Delta(r') dr')$), the full Hamiltonian takes the form $\langle \mu | \hat{H} | \mu' \rangle = \omega_0 \mu \delta_{\mu,\mu'} + \langle \mu | \hat{V} | \mu' \rangle$, where the second term is due to the random white-noise impurity potential $U(\mathbf{r})$ with the variance $\langle U(\mathbf{r}) U(\mathbf{r}') \rangle = \delta(\mathbf{r} - \mathbf{r}')/(2\pi\nu\tau)$; correspondingly, in the functional integral one should use a μ-dependent supervector Φ_μ instead of the superfield $\Phi(\mathbf{r})$. This Hamiltonian has the symmetry

$$\hat{H} = -\hat{\gamma} \hat{H}^T \hat{\gamma}^T; \quad \langle \mu | \hat{\gamma} | \mu' \rangle = (-1)^{\mu+1/2} \delta_{\mu+\mu'}, \tag{1}$$

which follows from an identity $\Psi_{-\mu}(\mathbf{r}) = (-1)^{\mu+1/2} i \tau_y \Psi_\mu^*(\mathbf{r})$ that reflects the basic symmetry property of the Hamiltonian; τ_y is the Pauli matrix in the Nambu space.

The standard way to solve a complicated random matrix problem is to represent it in a form of the effective field theory. In order to reduce the RM problem given by Eq. (1) to the 1D field theory we make a continuous Fourier transform (considering N as very large) from the momentum variable μ to the "angle" $\phi \in [0, 2\pi)$, so our superfield will be defined as $\Phi(\phi) = \Sigma_\mu \Phi_\mu e^{-i(\mu-1/2)\phi} \equiv \Phi_\phi$. Now we can write down an expression for the "partition function" ($\epsilon_+ \equiv \epsilon + i\delta$):

$$Z^R(\epsilon) = \int \exp i \int \frac{d\phi}{2\pi} \left\{ \Phi_\phi^* \left(\epsilon_+ - i\omega_0 \frac{\partial}{\partial\phi} - \frac{\omega_0}{2} \right) \Phi_\phi \right.$$

$$\left. - \int \frac{d\phi'}{2\pi} \Phi_\phi^* V(\phi, \phi') \Phi_{\phi'} \right\} D^2 \Phi_\phi. \tag{2}$$

The matrix elements $V(\phi, \phi')$ of the random potential in the ϕ space obey the symmetry relationship that follows from Eq. (1) and are given by $V(\phi, \phi') = -e^{i(\phi-\phi')} V^*(\phi + \pi, \phi' + \pi) = A^2 \int d^2 \mathbf{r} w_{\phi\phi'}(r, \theta) U(\mathbf{r}) e^{-2K(r)}$. The function $w_{\phi\phi'}$ can be written, using the Bessel function summation formulas, as

$$w_{\phi\phi'}(r, \theta) = (1 - e^{i(\phi-\phi')}) \exp\{-ik_F r[(\sin\phi - \sin\phi')$$

$$\times \cos\theta + (\cos\phi - \cos\phi')\sin\theta]\}. \tag{3}$$

All features of the theory are encoded in the pair correlator $\mathcal{W}(\phi_1, \phi_2, \phi_3, \phi_4) = \langle V(\phi_1, \phi_2) V(\phi_3, \phi_4) \rangle$ where the averaging is performed over the Gaussian distribution of the random potential $U(\mathbf{r})$. Since the typical value of $k_F r \sim k_F \xi \gg 1$, the correlator $\mathcal{W}(\phi_1, \phi_2, \phi_3, \phi_4)$ is appreciably nonzero only when the oscillating exponents in Eq. (3) nearly cancel each other, i.e., when its arguments ϕ_i are pairwise coinciding:[12]

$$\mathcal{W}(\phi_1,\phi_2,\phi_3,\phi_4) = \frac{g\omega_0^2}{\pi} T(\phi_{12}+\pi)(2\pi)^2 [\,\delta(\phi_{14})\delta(\phi_{23})$$

$$- e^{i\phi_{12}}\delta(\phi_{13}+\pi)\delta(\phi_{24}+\pi)\,], \tag{4}$$

where $\phi_{kl} \equiv \phi_k - \phi_l$, $g = 2A^4/\pi\nu\tau\omega_0^2 k_F^2 \sim 1/\omega_0\tau \gg 1$ and the kernel T is given by

$$T(\phi) = \frac{\pi}{2}\left|\cot\frac{\phi}{2}\right|, \quad \text{if } |\phi| > \frac{1}{\sqrt{N}}; \quad T(\phi) \approx \sqrt{N}, \quad \text{if } |\phi| < \frac{1}{\sqrt{N}}. \tag{5}$$

The δ-function approximation (4) for the correlator $\mathcal{W}$ is valid as long as the scale of the angular variations of the field $\Phi(\phi)$ (below it will be seen to be $\ell = [g\ln(N/g)]^{-1})$ is longer than the actual[12] width $w(\phi_{12}) \sim |N\sin(\phi_{12})|^{-1}$ of those δ functions. Thus the following derivation is strictly valid under the condition $w(\ell) \ll \ell$, which is equivalent to

$$\tau\sqrt{\omega_0\Delta} \gg \ln\Delta\tau. \tag{6}$$

Below we will assume that the inequality (6) is fulfilled.

The next step of the σ model derivation is to average the partition function (2) using Eqs. (4) and (5). Before doing that we need to take explicitly into account the symmetry (1), which amounts to a doubling of the number of components of the supervector $\Phi(\phi)$. Thus we introduce (cf. with a similar procedure in Ref. 6) an additional 2×2 ''particle–hole'' (PH) space and define a 4-dimensional superfield $\psi(\phi) = 2^{-1/2}(\Phi(\phi), e^{i\phi}\Phi^*(\phi+\pi))^T$. Next we define the bar-conjugate superfield as $\bar{\psi}(\phi) = \psi^+\sigma_z = [C(\phi)\psi(\phi+\pi)]^T$, with $C(\phi) = -e^{-i\phi}\sigma_z C_0$, where σ_z is the Pauli matrix in the PH space, and the 4×4 matrix C_0 consists of the blocks $C_0^{pp} = C_0^{hh} = 0$, $C_0^{ph} = 1$, and $C_0^{hp} = k$, where $k = \mathrm{diag}(1,-1)$ acting in the Fermi–Bose space. After an averaging over the disorder, the effective action $\mathcal{A}\{\psi\}$ for the retarded Green function $\mathcal{G}^R(\epsilon) = -i\int \Phi^f(\Phi^f)^+\exp[\mathcal{A}\{\psi\}]D\psi^*D\psi$ (where Φ^f means the fermionic component of Φ) can be written as (we denote $\psi_j \equiv \psi(\phi_j)$):

$$\mathcal{A} = i\int \frac{d\phi_1}{2\pi}\bar{\psi}_1\left(\epsilon_+\sigma_z - i\omega_0\frac{\partial}{\partial\phi_1} - \frac{\omega_0}{2}\right)\psi_1 - \frac{g\omega_0^2}{\pi}$$

$$\times \int\int \frac{d\phi_1 d\phi_2}{(2\pi)^2} T(\phi_{12}+\pi)\bar{\psi}_1\psi_2\bar{\psi}_2\psi_1. \tag{7}$$

The second term in the action (7) is similar to that of the 1D tight-binding model with off-diagonal random matrix elements with variance decaying as $1/|x|$, as long as we are interested in scales $|x| \equiv |\phi_1 - \phi_2 + \pi| \ll \pi$. Thus the usual 1D localization is absent in our problem because of the long-range nature of the off-diagonal disorder (cf. Ref. 13).

There is also another way of considering this term, which helps to gain some intuition about its effect. Namely, one can think of the variable ϕ as an angle associated with the 2D quasiparticle momentum $p = k_F\{\cos\phi,\sin\phi\}$. Then the last term in Eq. (7) corresponds to a 2D particle–hole scattering strongly enhanced in the forward direction. For such a singular scattering one has to define two scattering lengths ℓ and $\ell_{tr} \gg \ell$ (cf. with a similar situation discussed in Ref. 14): $1/\ell \propto g\int d\phi\,\sigma(\phi) = g\ln(N/g)$, and $1/\ell_{tr} \propto g\int d\phi\,\sigma(\phi)(1-\cos\phi) = g \gg 1$, where $\sigma(\phi)$ is the differential cross section and $\phi = \phi_1 - \phi_2 + \pi$. For careful evaluation of the logarithmically divergent scattering rate

$1/\ell$, one should use the self-consistent Born approximation (SCBA), which takes into account both terms in Eq. (4). It is equivalent to taking into account the ''noncrossing'' diagrams that can be generated by a perturbative expansion of $\exp[\mathcal{A}\{\psi\}]$ in powers of g. For $\epsilon/\omega_0 \ll 1/\ell$, the ''crossing diagrams'' of the same order in g turn out to be small by the parameter $\ell/\ell_{tr} = 1/\ln(N/g)$. It stands for the usual quasiclassical parameter $(k_F \ell_{tr})^{1-d}$ in this effectively 1D problem.

The existence of the small parameter $1/\ln(N/g) = 1/\ln \Delta\tau$ that allows one to neglect the ''crossing diagrams'' implies that one can derive an effective field theory (nonlinear sigma model) which describes the low-energy behavior of the averaged Green function $G^R(\epsilon)$ for $\epsilon/\omega_0 \ll 1/\ell = g \ln(N/g)$. This can be done in a standard way[1] by the Hubbard–Stratonovich decoupling of the quartic term in Eq. (7) and a further saddle point approximation controlled by the parameter $1/\ln(N/g)$. Because of the symmetry relation (1) and the corresponding relation between $\bar{\psi}$ and ψ, one has to perform both a local decoupling containing $P(\phi)\psi(\phi)\otimes\bar{\psi}(\phi)$ and a nonlocal one containing $R(\phi_1,\phi_2)\psi(\phi_1)\otimes\psi^T(\phi_2)$. Under the condition $\ell \gg 1/\sqrt{N}$ given by Eq. (6), both decouplings are important in order to obtain the correct form for the imaginary part of the Green function in the saddle-point approximation $P(\phi) = P_0$, $R(\phi_1,\phi_2) = R_0(\phi_1 - \phi_2)$, which is equivalent to the SCBA:

$$G_\epsilon(\phi) = -\frac{2\pi i}{\omega_0}\sigma_z\theta(-\sigma_z\phi)e^{-|\phi|/\ell}e^{-i\frac{\epsilon}{\omega_0}\phi}, \quad P_0 = \frac{T_0}{\omega_0}\sigma_z, \quad R_0(\phi) = \frac{i}{\pi}T(\phi)G_\epsilon(-\phi),$$

$$(8)$$

where $T_0 = \int_0^{2\pi}T(\phi)\,d\phi/2\pi \approx \frac{1}{2}\ln N$. In general, the mth Fourier harmonic of the kernel $T(\phi)$ is given by $T_m \approx \ln(\sqrt{N}/|m|)$ for $1 \ll m \ll \sqrt{N}$.

Mesoscopic fluctuations are known[1] to be described by the slow rotations of the saddle-point solution, which are represented in our case as $P(\phi) = U^{-1}(\phi)P_0 U(\phi)$, $R(\phi,\phi') = U^{-1}(\phi)R_0(\phi - \phi')U(\phi')$. The corresponding action that describes the low-energy spectral properties of the CdGM levels, reads:

$$\mathcal{A}_\sigma[Q,U] = -\frac{\pi g}{4}T_0^2 \int\int \frac{d\phi_1 d\phi_2}{(2\pi)^2}T^{-1}(\phi_1 - \phi_2 + \pi)\mathrm{Str}\,Q(\phi_1)Q(\phi_2)$$

$$-\frac{\pi i}{2}\int \frac{d\phi}{2\pi}\mathrm{Str}\left(\frac{\epsilon}{\omega_0}\sigma_z Q(\phi) - i\sigma_z U(\phi)\frac{\partial U^{-1}(\phi)}{\partial\phi}\right), \quad (9)$$

where $Q(\phi) = U^{-1}(\phi)\sigma_z U(\phi)$, and $U(\phi)$ is a π-periodic, pseudo-unitary ($U^{-1}(\phi) = \bar{U}(\phi)$)) matrix. The action (9) is valid for energies $\epsilon \ll \omega_0/\ell = \tau^{-1}\ln\Delta\tau$.

The supermatrix Q can be represented in the form $Q(\phi) = \sigma_z[1 + W(\phi) + \frac{1}{2}W^2(\phi) + O(W^3)]$, with the supermatrix W being purely off-diagonal in the PH space. Then the symmetry $Q = \bar{Q}$ and convergence arguments lead to the following form for the W_{ph} and W_{hp} blocks:

$$W_{ph}(\phi) = \begin{pmatrix} iz(\phi) & \alpha_1(\phi) \\ \alpha_1(\phi) & 0 \end{pmatrix}_{fb}, \quad W_{hp}(\phi) = \begin{pmatrix} iz^*(\phi) & \alpha_2(\phi) \\ -\alpha_2(\phi) & 0 \end{pmatrix}_{fb}. \quad (10)$$

Here z is a complex number and α_i are the Grassmann numbers. Expanding over $W(\phi)$, we obtain in the quadratic approximation

$$\mathcal{A}_2[W_m] = \frac{\pi}{4} \operatorname{Str} \sum_m \left\{ 2g \left(\sum_{k=0}^{|m|-1} \frac{1}{2k+1} \right) + i \left(m\sigma_z - \frac{\epsilon}{\omega_0} \right) \right\} W_{2m} W_{-2m}, \tag{11}$$

where the W_m are the mth harmonics of the field $W(\phi)$. Note that in Eq. (11) only even harmonics enter; odd harmonics, as well as the ''longitudinal'' modes, have a larger gap of the order of ω_0/ℓ and are excluded from the sigma-model action.

Equation (11) sets a characteristic scale $L = (g \ln g)^{-1}$ for the angular variations of the matrices $U(\phi)$. This scale should be larger than the scattering length ℓ. Only in that case can one neglect higher terms of the gradient expansion in powers of $\partial U/\partial \phi$, as was done in deriving Eq. (9). Comparing to $\ell = [g \ln(N/g)]^{-1}$ we see that the parameter of the gradient expansion, $\ell/L = \ln g/\ln(N/g)$, is small if the condition (6) is fulfilled. The length L determines the angular size of the elementary propagator corresponding to the sigma model (9). In this respect it is analogous to the system size in the usual weak-localization problem. The fact that $\ell/L \ll 1$ in our problem tells us that the problem is essentially not ballistic, though it is not diffusional either, since $\ell_{tr}/L = \ln g \gg 1$.

An important property of the action (9) is that it takes a universal form if U is independent of ϕ. At low energies the main contribution comes from the zeroth harmonics of $Q(\phi)$, i.e., the problem reduces to the zero-dimensional σ model. The uniform supermatrix Q is parametrized by 2 real variables (one of which appears to be cyclic) and 2 Grassmann variables, so the final expression for the average DoS is

$$\langle \rho(\epsilon) \rangle = \frac{1}{4\widetilde{\omega}_0} \Re \int_0^\pi d\theta \int d\eta d\zeta \frac{\sin \theta}{1 - \cos \theta} [(1 + \cos \theta)$$

$$+ 2\eta\zeta(1 - \cos \theta)] e^{\pi i \frac{\epsilon}{\omega_0}(1 - \cos \theta)}$$

$$= \frac{1}{\widetilde{\omega}_0} \left(1 - \frac{\sin(2\pi\epsilon/\widetilde{\omega}_0)}{2\pi\epsilon/\widetilde{\omega}_0} \right). \tag{12}$$

The functional form of this result coincides with the result of the AZ phenomenological approach.[5] However, it is expressed via the renormalized mean level spacing $\widetilde{\omega}_0 = \omega_0(1 + (1/2\ln g))$. The renormalization is due to the contributions of higher $W_{m \geq 2}$ modes, which lead[12] to the decrease of the DoS for $\epsilon \lesssim \omega_0/L = g\omega_0 \ln g$ by the relative amount of $\delta\omega_0/\omega_0 = 1/(2 \ln g) \ll 1$. At higher energies this correction decreases as $\delta\omega_0/\omega_0 \propto (g\omega_0 \ln g)^2/\epsilon^2$. This correction can be found using a general approach,[15] in which the perturbative treatment of the nonzero modes leads to the ''induced'' terms in the 0D action. It is given by the single-cooperon diagram, which is absent in the usual normal-metal problems,[1,15] from the formal point of view, the difference stems from the absence of the BB block in the parametrization (10). The usual[15] two-cooperon diagram leads to the ''induced'' term $\propto (\epsilon/\omega_0)^2 (g \ln g)^{-1}$ (cf. Ref. 3). The possibility of neglecting this term determines the upper limit of energies where a purely 0D description is valid: $\epsilon \lesssim \omega_{\mathrm{Th}} = \omega_0 \sqrt{g \ln g}$.

To conclude, we have derived microscopically the supersymmetric field theory for the statistics of the localized electron levels inside the vortex in a moderately clean

superconductor. Our supermatrix σ model, Eq. (9) was derived in leading order in the quasiclassical parameter $1/\ln \Delta \tau$. The approach proposed previously in Ref. 5 is shown to be valid in the low-energy range $\epsilon \lesssim \omega_{\mathrm{Th}} = [(\omega_0/\tau)\ln(1/\omega_0\tau)]^{1/2}$, where the 0D σ model is applicable. Mixing between zero- and higher modes leads to a decrease of the DoS by a relative amount $[2\ln(1/\omega_0\tau)]^{-1}$ at energies $\epsilon \lesssim \tau^{-1}\ln(1/\omega_0\tau)$.

[1] K. B. Efetov, *Supersymmetry in Disorder and Chaos*, Cambridge Univ. Press, New York, 1997.
[2] C. W. J. Beenakker, Rev. Mod. Phys. **69**, 731 (1997).
[3] A. Altland, B. Simons, and D. Taras-Semchuk, JETP Lett. **67**, 22 (1998).
[4] F. Zhou, P. Charlat, B. Spivak, and B. Pannetier, http://xxx.lanl.gov/abs/cond-mat/9707056.
[5] A. Altland and M. R. Zirnbauer, Phys. Rev. B **55**, 1142 (1997).
[6] K. M. Frahm, P. W. Brouwer, J. A. Melsen, and C. W. J. Beenakker, Phys. Rev. Lett. **76**, 2981 (1996).
[7] C. Caroli, P. G. de Gennes, and J. Matricon, Phys. Rev. Lett. **9**, 307 (1964).
[8] N. B. Kopnin and V. E. Kravtsov, JETP Lett. **23**, 578 (1976); Zh. Éksp. Teor. Fiz. **71**, 1644 (1976) [Sov. Phys. JETP **44**, 861 (1976)].
[9] G. E. Volovik, JETP Lett. **57**, 244 (1993); Zh. Éksp. Teor. Fiz. **104**, 3070 (1993) [JETP **77**, 435 (1993)].
[10] M. V. Feigel'man and M. A. Skvortsov, Phys. Rev. Lett. **78**, 2640 (1997).
[11] A. I. Larkin and Yu. N. Ovchinnikov, Phys. Rev. B **57**, 5457 (1998); A. I. Larkin and A. A. Koulakov, http://xxx.lanl.gov/abs/cond-mat/9802002.
[12] M. A. Skvortsov, V. E. Kravtsov, and M. V. Feigel'man, in preparation.
[13] A. D. Mirlin, Yan V. Fyodorov, F.-M. Dittes *et al.*, Phys. Rev. E **54**, 3221 (1996).
[14] A. G. Aronov, A. D. Mirlin, and P. Wölfle, Phys. Rev. B **49**, 16609 (1994).
[15] V. E. Kravtsov and A. D. Mirlin, JETP Lett. **60**, 656 (1994).

GaAsSb/GaAs quantum well growth by MOCVD hydride epitaxy with laser sputtering of antimony

V. Ya. Aleshkin

Institute of Physics of Microstructures, Russian Academy of Sciences, 603600 Nizhniĭ Novgorod, Russia

S. A. Akhlestina, B. N. Zvonkov, N. B. Zvonkov, I. G. Malkina, and E. A. Uskova

Scientific-Research Institute, Physicotechnical Institute of the State University[a)]

A new method of obtaining quantum-size $GaAs_{1-x}Sb_x$ ($x \leqslant 0.45$) layers is proposed. The method consists in laser vaporization of solid metallic antimony near the substrate directly in the reactor. The antimony concentration is set by the antimony sputtering time with the arsine flux shut off. The polarization of the photoluminescence of the obtained layers indicates the formation of quantum wires. The heterostructures obtained are used to fabricate laser diodes. © *1998 American Institute of Physics.* [S0021-3640(98)01513-8]

PACS numbers: 81.15.Gh, 81.15.Kk, 85.40.Sz

Heterolasers based on InGaAs/GaAs quantum wells (QWs) have achieved record values of such very important parameters as the threshold current density and output power at high reliability.[1] However, the spectral range of these lasers is limited on the long-wavelength side by ≈ 1 μm. To advance in the direction of long wavelengths the indium concentration must be increased, and this gives rise to of misfit dislocations and lower radiation efficiency. In Ref. 2 it was shown that using GaAsSb as a quantum layer instead of InGaAs makes it possible to advance into the wavelength range 1.2–1.3 μm. Ordinarily, GaAsSb is grown by molecular-beam epitaxy. Since the antimony distribution factor is small, in MOCVD hydride epitaxy a relatively large quantity of toxic gases is required in order to introduce it. In the present work GaAsSb/GaAs QWs were obtained by MOCVD hydride epitaxy with a solid antimony source. The results of an investigation of the growth and properties of these QWs are presented.

The samples consisted of a (001) *i*-GaAs substrate and a $GaAs_{1-x}Sb_x$ quantum layer (≈ 9 nm thick), sandwiched between GaAs buffer and cover layers (0.15 μm). The surface of the substrates was inclined by 3° in the directions [110] or [−110]. The composition of the quantum-size layer obtained was determined by comparing the positions of the photoluminescence (PL) peak observed at 77 K with the computed spectrum of the quantum well. The calculation was performed on the basis of the model described in Ref. 3. It was assumed that the offset of the conduction band at the heterointerface equals zero.[4] However, it is possible that the $GaAs_{1-x}Sb_x$ quantum layer is a barrier for elec-

trons in the conduction band. In this case the calculation gives values of x which are too high.

The quantum wells were grown in a horizontal quartz reactor at atmospheric pressure. Trimethyl gallium (TMG), 100% arsine, and metallic antimony were used as sources. The antimony source was placed approximately 12 cm from the substrate in the cold zone of the reactor. The antimony was sputtered by focused 0.3 J pulses with a repetition frequency of 12.5 Hz from a Q-switched YAG:Nd laser during GaAsSb growth. A similar method was used earlier for doping epitaxial GaAs with electrically active impurities.[5] Here it was used to introduce the main material in the process of MOCVD hydride epitaxy. The sputtering rate, determined according to the decrease in the target mass, was equal to $(3-3.5)\times10^{-8}$ moles/sec. Some sputtered antimony settled on the reactor walls without reaching the substrate holder.

The buffer and cover GaAs layers were grown at 600 °C with a growth rate of ≈0.5 nm/s. The arsine and TMG fluxes were equal to 6.6×10^{-7} and 8.6×10^{-8} moles/sec, respectively. The GaAsSb QW growth temperature was chosen in the range 490–580°C. During the sputtering of antimony the growth rate of the layer did not change appreciably and once again was proportional to the TMG flux. As expected, very little antimony enters the epitaxial layer in the presence of arsenic. Even with a large decrease in the arsine and TMG fluxes (by a factor of 6–10), sputtering of antimony did not appreciably change the composition of the grown layer from GaAs. For this reason, periodic delivery of arsine and TMG in the presence of a continuous antimony flux was used.

The flux switching regime consisted of the following. Before commencement of growth of the solid solution, arsine delivery was stopped and sputtering of antimony was commenced. At the same time the TMG valve was opened. After this, during a period of time t_1 (from 2 to 6 s) a quantity of gallium that was necessary for depositing approximately one monolayer (1 ML = 0.3 nm) of GaAs or GaSb on the substrate surface, which was stabilized with group-V elements, entered the reactor. Next, the TMG valve was closed, and for a time t_2 (from 0 to 60 s) only the sputtered antimony was delivered to the substrate. In the process, the surface was built up with antimony atoms. Finally, arsine was delivered for a time $t_3=1$ s, which made it possible to finish the incomplete layer of group-V atoms. With the process repeated 30 times, a 9 nm thick quantum-size layer was obtained. Holding the surface depleted of the group-V element in the antimony flux for a time t_2 facilitated the incorporation of antimony, which is difficult under conditions of excess arsenic, which are standard for MOCVD hydride epitaxy. In this growth regime it was found that the composition of the quantum-size layer could be controlled by specifying the time t_2.

Figure 1a shows the dependence of the composition of the grown quantum-size layer on the holding time of the surface in the antimony flux with the arsine flux shut off. One can see that the antimony concentration in the QW layer is proportional to the time t_2 and decreases substantially as the amount of arsenic delivered in the time t_3 increases. (The values of x on the straight line *1* were obtained with an arsine flux three times lower than for the points *2*.)

As the amount of gallium delivered in the time interval t_1 increased (Fig. 1b), the antimony concentration in the layer increased substantially. Thus, $GaAs_{1-x}Sb_x$ layers
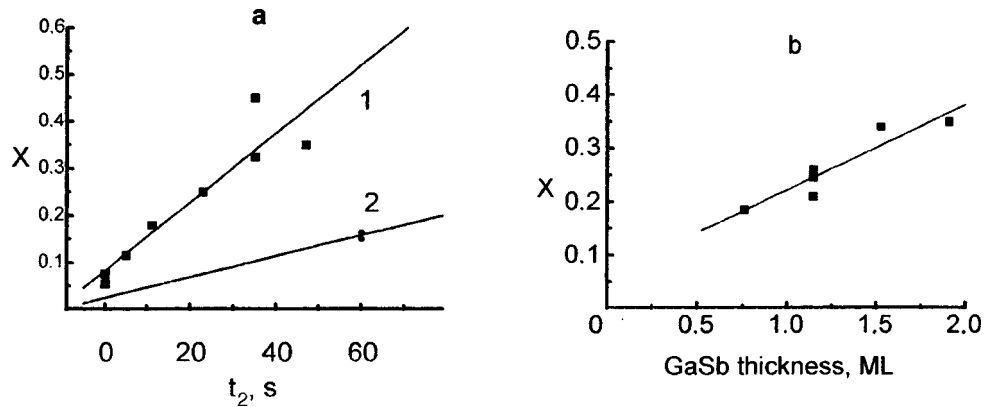
FIG. 1. Composition of a $GaAs_{1-x}Sb_x$ quantum-size layer versus growth conditions: a) versus the duration of the holding period of the gallium-enriched growth surface without arsine; b) versus the amount of gallium delivered during the antimony sputtering time. The arsine flux delivered to finish building the surface with a group-V element (during the period of time t_3) for the straight line *1* is three times lower than for the data points on the straight line *2*.

with $x \leqslant 0.45$ were grown. Further increasing x resulted in degradation of the surface morphology of the structure, apparently as a result of the impossibility of coherent growth.

The requirement that low arsine fluxes be used (1% of the total scale of the gas flow regulator) gave rise to scatter in the values obtained for x. In some cases, because of the drift of the zero point of the gas flow regulator controlling the arsine flux, growth evidently occurred under conditions of a shortage of group-V elements. The surface of the samples became dull, probably because of the appearance of gallium droplets on the surface and subsequent crystallization of the droplets under conditions of excess arsenic during growth of the top GaAs layer. The optical characteristics of such samples were identical to the characteristics of structures with a shiny surface, confirming the relation between the roughness of the surface and excess gallium and not antimony. The results of the measurements obtained on these samples are not presented in the plots.

No effect of growth temperature on the composition of the layers obtained was observed (Fig. 2, curve *1*). The decrease in the PL efficiency as the growth temperature decreases from 55°C (Fig. 2, curve *2*) is apparently due to the usual decrease of the nonradiative lifetime in GaAs grown by MOCVD hydride epitaxy at low temperatures. The PL efficiency likewise decreases for growth temperatures above 550°C, since an increase in the desorption rate of group-V atoms accelerates degradation (increase in the defect density) of the growth surface during the holding period without arsine.

Figure 3 shows the PL spectra of GaAsSb/GaAs QWs 9–10 nm wide, grown by the method described. The curves *1–6* correspond to layers obtained with t_2 ranging from 0 to 35 s. One can see that the PL band of the GaAsSb QW shifts strongly in the direction of long wavelengths as the holding time in the antimony flux increases. However, it is much wider than in the case of InGaAs QWs. Shown for comparison is curve *7*, from a sample with two $In_xGa_{1-x}As/GaAs$ QWs with $x = 0.1$ and $x = 0.2$. The large width of the PL band was also noted in Ref. 2 for a GaAsSb QW. The increase in the width of the

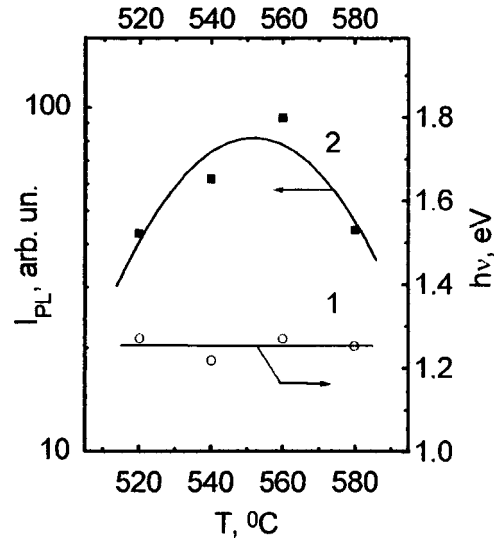FIG. 2. Energy of the maximum (*1*) and intensity of PL (*2*) of a $GaAs_{1-x}Sb_x$ quantum-size layer versus the growth temperature.

spectrum could be due to the presence of a type-II heterojunction, since indirect (in real space) recombination occurs in it, specifically, recombination of holes trapped in the QW with electrons in the GaAs.

On the other hand, comparing curves *1–6* shows that the width of the spectrum increases as the antimony concentration increases, and this attests to the presence of ordered inclusions or stratification in the solid solution GaAsSb.

Figure 4 (curve *1*) shows the dependence of the width of the PL spectrum of a GaAsSb quantum well on the photon energy at the maximum (on the composition of the quantum layer). Irrespective of the variation of the growth conditions (temperature and/or
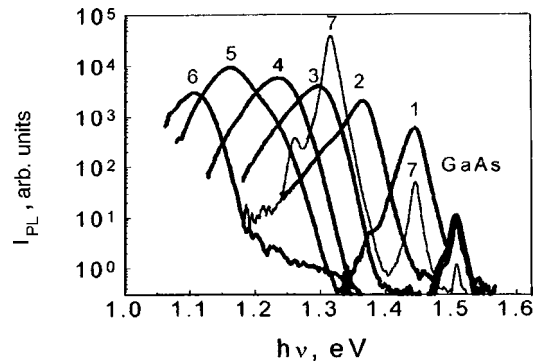

FIG. 3. PL spectra of a $GaAs_{1-x}Sb_x$ /GaAs QW (*1–6*). The curves are numbered in order of increasing t_2. The spectrum of a structure with two $In_xGa_{1-x}As$/GaAs QWs (*7*) is presented for comparison.
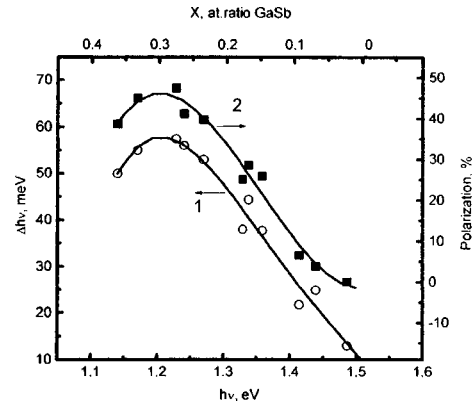
FIG. 4. Spectrum width (*1*) and degree of polarization (*2*) of the PL of a GaAs$_{1-x}$Sb$_x$/GaAs QW versus the energy of the maximum of the PL intensity (composition of the quantum layer).

TMG and arsine fluxes), the experimental data fall on the same curve. The linewidth increases from 10 to 60 meV as photon energy decreases (x increases), reaches its maximum value at ~ 1.2 eV ($x = 0.3$), and then decreases.

To determine the nature of this phenomenon, the linear polarization of the PL was investigated. The degree of polarization was calculated according to the formula $P = (I_{max} - I_{min})/(I_{max} + I_{min})$, where I_{max} and I_{min} are, respectively, the maximum and minimum PL intensities as a function of the rotation angle of the polarizer. It was observed that the PL is strongly polarized. The direction of polarization (electric field vector of the PL) in the plane of the substrate was always the same as the direction $[-110]$, determined by chemical etching, and did not depend on the direction of inclination of the surface of the sample away from the (001) plane. The degree of polarization of the PL reached 50%. Its dependence on the energy of the maximum point (Fig. 4, curve *2*) is identical to the shape of the curve of the width of the spectrum (curve *1*), attesting to their common cause.

Such a cause could be stratification of the solid solution GaAsSb,[6] leading to the formation of inclusions, which extend along $[-110]$, with a smaller band gap. This hypothesis is confirmed by the results of measurements of the polarization of PL emitted along the layers of the structure from the cleaved end: The PL emitted from the end in the direction $[-110]$ is weakly polarized ($<10\%$), while the PL in the $[110]$ direction is strongly polarized in the plane of the QW.

It was found that the PL parameters (energy, linewidth, and intensity) do not change even after the structure is annealed at 650°C for 30 min, and the above-described growth procedure can be used to grow laser heterostructures. Laser structures with GaAs$_{0.8}$Sb$_{0.2}$ quantum layers, a GaAs active region, and InGaP layers as confining solid solutions were obtained on GaAs substrates. Laser diodes with a 100 μm wide active region and a 1 mm long resonator were prepared from them. They emitted at ≈ 1 μm and their threshold current density was equal to 3 kA/cm^2 with excitation by 200 ns current pulses at room temperature.

This work was supported by the Russian Fund for Fundamental Research (Grant No.

98-02-16688) and the Ministry of Science (Program FTNS 97-1089).

[a] e-mail: fdp@phys.unn.runnet.ru

[1] Zh. I. Alferov, Fiz. Tekh. Poluprovodn. **32,** 1 (1998) [Semiconductors **32**, 1 (1998)].

[2] T. Anan, K. Nishi, Sh. Sugou *et al.*, *Tenth Annual Meeting of IEEE LEOS,* PD1.4, San Francisco, November 1997.

[3] G. Huang, D. Yi, V. K. Reddy *et al.*, J. Appl. Phys. **62**, 3366 (1987).

[4] M. A. Herman, *Semiconductor Superlattice,* Akademie Verlag, Berlin, 1986.

[5] B. N. Zvonkov, V. V. Podol'skiĭ, V. P. Lesnikov *et al.*, Vysokochistye Veshchestva **4,** 114 (1993).

[6] S-K. Sun, S. Keller, G. Wang, M. S. Minsky, J. E. Bowers, and S. P. BenBaars, Appl. Phys. Lett. **68**, 1545 (1996).

Translated by M. E. Alferieff

Direct observation of phase separation in La$_{1-x}$Ca$_x$MnO$_3$

N. N. Loshkareva, Yu. P. Sukhorukov, S. V. Naumov, N. I. Solin,
I. B. Smolyak, and E. V. Panfilova

Institute of Metal Physics, Urals Branch of the Russian Academy of Sciences, 620219 Ekaterinburg, Russia[a]

In a study of the infrared optical absorption spectra of polycrystalline La$_{1-x}$Ca$_x$MnO$_3$ ($0.1 \leqslant x \leqslant 0.8$), a contribution from free charge carriers is observed below the Curie temperature for compositions with $x \leqslant 0.4$. The existence of this contribution for samples with a high resistivity is a direct proof of the existence of ''metallic'' drops in an insulating matrix. The relative volume of the ''metallic'' phase is estimated. © *1998 American Institute of Physics.*
[S0021-3640(98)01613-2]

PACS numbers: 75.50.Pp, 78.30.Hv, 64.75.+g

Lanthanum manganites, like other degenerate magnetic semiconductors and high-T_c superconductors (HTSCs), belong to the class of materials exhibiting thermodynamically equilibrium phase separation.[1,2] The formation of regions of charge and magnetic non-uniformity is invoked to explain many physical properties of these materials, but there is no direct experimental proof of the existence of such regions. In the present work optical methods are used to observe phase separation directly and to estimate the volume of the metallic (ferromagnetic) regions in an antiferromagnetic matrix. In contrast to magnetic and electrical methods, optical methods do not require the application of magnetic fields, and hence they do not distort the regions formed and they make it possible to distinguish small inclusions of a ''metallic'' phase against the background of an insulating matrix.

La$_{1-x}$Ca$_x$MnO$_3$ ($0.1 \leqslant x \leqslant 0.8$) single crystals were prepared from La$_2$O$_3$, CaCO$_3$, and MnO$_4$ powders (all powders consisted of ultrapure materials) by ceramic technology. The samples were synthesized in two stages: annealing at 1300°C in air for 30 h, followed by grinding and then repeated annealing at 1300°C for 50 h in air. X-ray crystallographic and x-ray phase analyses were performed on an x-ray DRON-2.0 diffractometer in Cr $K\alpha$ radiation. The samples obtained were single-phase. For the composition with $x = 0.8$ the unit-cell structure is orthorhombic, while for all other compositions the unit cell is cubic with weak orthorhombic distortions.

The Curie temperatures T_c were determined by the kink method according to the temperature dependence of the magnetization in weak magnetic fields (20–50 Oe). The dc resistivity ρ was measured by the standard four-contact method.

To measure the infrared (IR) absorption spectra, samples were prepared by the standard procedure: pressing of the powder to be studied in a transparent CsI matrix. A
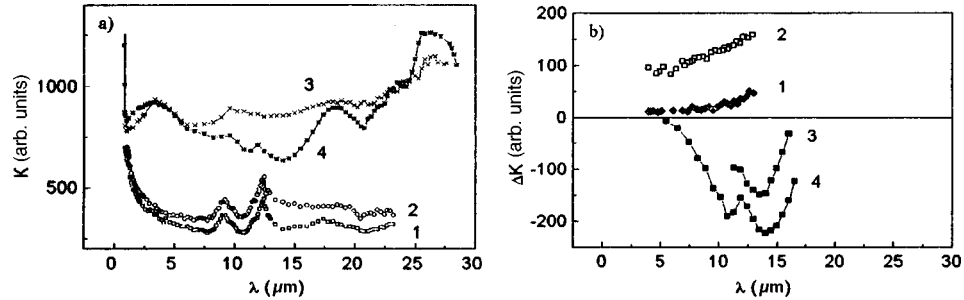
FIG. 1. Spectral dependences of the absorption (a) and the difference of absorption at temperatures 80 K and 293 K (b) of polycrystalline $La_{1-x}Ca_xMnO_3$: a) *1,2 — x=0.2; 3,4 — x=0.8; 1,3 — T=293 K; 2,4 — T=80 K*; b) *1 — x=0.1, 2 — x=0.3, 3 — x=0.6, 4 — x=0.8*.

mixture of the lanthanum manganite solid solution and dehydrated CsI powder in the ratio 3:400 was pressed under a pressure of 0.9 GPa. The spectra of the mixtures relative to pure CsI were investigated in the spectral range 0.75–35 μm and in the temperature interval 80–293 K on an automated IKS-21 spectrometer.

Figure 1a shows the absorption spectra $K(\lambda)$ for compositions with $x=0.2$ and $x=0.8$ at two temperatures. The spectra presented for the sample with $x=0.2$ are characteristic for all compositions with $x \leqslant 0.4$, while the spectrum presented for $x=0.8$ is similar to the spectrum for the composition with $x=0.6$. For all compositions, the increase in the absorption on the short-wavelength side is due to the onset of interband transitions, while at wavelengths above 14 μm it is due to the phonon spectrum. The two groups of bands in the "transmission window" (MIR bands — bands in the mid-IR range) at 3 μm (0.4 eV) and 8–12 μm (0.14–0.10 eV) are due to localized states. We have observed them in other lanthanum manganites also.[3]

As is well known, when a semiconductor is cooled, the absorption in the "transmission window" decreases. Such a situation is also observed in $La_{1-x}Ca_xMnO_3$ for compositions with $x=0.8$ (Fig. 1a) and $x=0.6$. For compositions with $x \leqslant 0.4$ absorption increases, despite the fact that $\rho(T)$ for compositions with $x=0.1$ and $x=0.4$ exhibits a semiconductor variation over the entire temperature range. The difference of the spectra obtained at 80 K (ferromagnetic (FM) region) and room temperature (paramagnetic (PM) region) $\Delta K = K_{80\,K} - K_{293\,K}$ shows (Fig. 1b) that the strongest changes in absorption with decreasing temperature for compositions with $x \geqslant 0.6$ occur near the minimum in front of the phonon spectrum at 14 μm. The additional absorption ΔK arising at a transition into the FM state for compositions with $x \leqslant 0.4$ increases as the wavelength increases (Fig. 1b); this is characteristic for the contribution of free charge carriers. The curves ΔK for compositions with $x=0.2$ and $x=0.4$ (not shown in Fig. 1b) lie somewhat below the curve 2 for $x=0.3$. With the high resistivity of samples with $x=0.1$ and $x=0.4$ at 80 K (Fig. 2a), assuming charge uniformity, it is impossible to explain the appearance of free carriers. Hence, the observed increase in the absorption by free carriers occurs in separate regions, i.e., drops. This allows us to conclude that optical methods detect "metallic" drops in an insulating matrix.

We showed earlier[3,4] that the conduction mechanism changes at a PM–FM transition. Conduction in the PM state occurs by polaron hopping and activation at the mobility
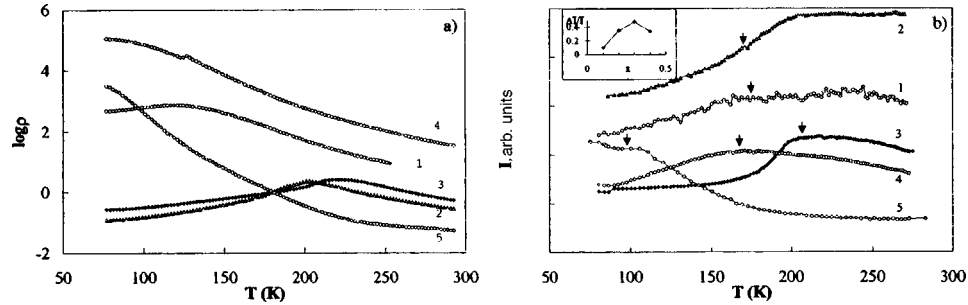
FIG. 2. Temperature dependences of the resistivity (a) and transmitted light intensity (b) of polycrystalline La$_{1-x}$Ca$_x$MnO$_3$: 1 — $x=0.1$, 2 — $x=0.2$, 3 — $x=0.3$, 4 — $x=0.4$, 5 — $x=0.8$. The arrows mark the Curie temperature. Inset: Relative volume of the metallic phase.

edge. The motion of the mobility edge with decreasing temperature leads to a insulator–metal transition near T_c, and the conductivity in the FM region is produced by the more mobile itinerant carriers. The change in the mechanisms occurs sharply. As shown in Ref. 5, a kink at a temperature below T_c is observed in the temperature dependence of the reflectance of a La$_{0.2}$Sr$_{0.8}$MnO$_3$ single crystal, measured at wavelength $\lambda = 14$ μm. For lanthanum manganites a wavelength of 14 μm is a convenient point for investigating the temperature behavior of the contribution of charge carriers. It corresponds to the minimum in front of the phonon spectrum, and its position does not depend on temperature. In semiconductors, in the absence of carriers the minimum is deep, and as the carrier density increases, the reflection at the minimum increases. In the present work, the temperature dependence of the absorption due to the contribution of charge carriers was studied at the wavelength 14 μm. The use of this wavelength is made possible by the weak temperature dependence of the intensity of neighboring absorption bands.

The temperature dependence of the resistivity ρ is presented in Fig. 2a, while the temperature dependence of the intensity I of the 14 μm light transmitted through the sample is presented in Fig. 2b. For all compositions with $x \leq 0.4$, a decrease, due to the appearance of a ''metallic'' contribution, of the transmitted light intensity is observed at temperatures $T < T_c$. For the composition with $x=0.8$, only a deviation from a monotonic dependence is present near T_c. It should be noted that an absolute correlation between the resistivity and transmittance of the samples is observed only for compositions with $x=0.2$ and $x=0.3$. The fact that the variations of the temperature dependences $\rho(T)$ and $I(T)$ are different for compositions with $x=0.1$ and $x=0.4$ is due to the insensitivity of the resistivity to isolated metallic drops in a nonconducting matrix. The temperature behavior of $I(T)$ below T_c apparently reflects an increase in the volume of the metallic drops. There is no domain scattering for the samples investigated. This follows from the fact that the temperature dependences $I(T)$ are the same in a 1 T magnetic field and without a field.

The drop off in the intensity of the transmitted light as temperature decreases is sharpest for the composition with $x=0.3$. For other compositions the drop off is protracted, which is apparently due to an assortment of ''metallic'' regions with different sizes. At low temperatures the intensity essentially does not change. The relative volume of the ''metallic'' phase is estimated as the ratio of the magnitude of the step in the

temperature dependence $I(T)$ to the intensity in front of the dropoff, i.e., $\Delta I/I = (I_{max} - I_{min})/I_{max}$, and is shown in the inset in Fig. 2. We note that the metallic conduction for the composition with $x = 0.3$ at $T < T_c$ is apparently due to touching of the ''metallic'' drops and formation of a ''through'' conducting channel, but islands of the insulating phase remain.

The regularities noted above for the optical properties are not associated with the polycrystallinity of the samples. Investigations of the absorption spectra of a $La_{0.9}Sr_{0.1}MnO_3$ single crystal ($T_c = 150$ K)[5] and of this single crystal pulverized and pressed with CsI likewise show an increase in absorption at 80 K as compared with room temperature. The resistivity of the $La_{0.9}Sr_{0.1}MnO_3$ single crystal exhibits semiconductor behavior in the entire temperature interval, except in the region 120–160 K, where a metal–insulator transition is observed in the drops. The ferromagnetic state is also associated with the ''metallic'' phase.[1,2] One proof of this is the ''red'' shift of the absorption edge in a $La_{0.9}Sr_{0.1}MnO_3$ single crystal in the ferromagnetic regions, a phenomenon which we observed earlier.[5]

A detailed analysis of the phase separation mechanism is possible on the basis of the model developed for HTSCs and copper oxide,[6] which is based on a charge disproportionation reaction. Recently, the existence of complexes based on Mn^{2+} and Mn^{4+}, which arise as a result of a disproportionation reaction $2Mn^{3+} \rightarrow Mn^{2+} + Mn^{4+}$, was proposed for explaining the thermopower and resistivity of $La_{1-x}Ca_xMnO_3$ single crystals.[7] By analogy to copper oxides,[6] the observed MIR bands in the absorption spectra of $La_{1-x}Ca_xMnO_3$ (Fig. 1a) at wavelengths $8 - 12$ μm and 3 μm, respectively, can be associated with hole (Mn^{4+}) and electronic (Mn^{2+}) clusters. For compositions with $x = 0.6$ and 0.8 the intensification of the absorption band at 3 μm, corresponding to transitions in an electronic cluster, agrees with the previously observed[7] increase in the electronic contribution as x increases.

In summary, the optical data attest to a direct observation of ''metallic'' regions in an insulating matrix of lanthanum manganites and make it possible to estimate the relative volume of these regions.

[a]e-mail: magsemi@ifm.e-burg.su

[1] É. L. Nagaev, Usp. Fiz. Nauk **165,** 529 (1995).

[2] É. L. Nagaev, Usp. Fiz. Nauk **166,** 833 (1996).

[3] N. N. Loshkareva, Yu. P. Sukhorukov, A. P. Nosov *et al.*, Fiz. Tverd. Tela (St. Petersburg) **39,** 1616 (1997) [Phys. Solid State **39**, 1440 (1997)].

[4] N. G. Bebenin, N. N. Loshkareva, Yu. P. Sukhorukov *et al.*, Solid State Commun. **106**, 357 (1998).

[5] N. N. Loshkareva, Yu. P. Sukhorukov, B. A. Gizhevskii *et al.*, Phys. Status Solidi A **164**, 863 (1997).

[6] A. S. Moskvin, N. N. Loshkareva, Yu. P. Sukhorukov *et al.*, Zh. Éksp. Teor. Fiz. **105**, 967 (1994) [JETP **78**, 518 (1994)].

[7] M. F. Hundley and J. J. Neumeier, Phys. Rev. B **55**, 11511 (1997).

Translated by M. E. Alferieff